



THE UNIVERSITY OF QUEENSLAND
A U S T R A L I A

GEOMETRIC MODELLING OF WOLF-RAYET BINARY COLLIDING WIND NEBULAE

Ryan M.T. White
BSc, BMath

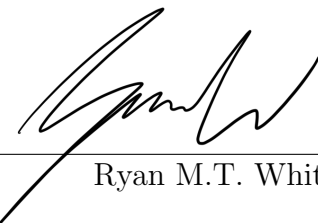
Under the supervision of
Dr Benjamin Pope and Professor Peter Tuthill

A THESIS SUBMITTED TO THE UNIVERSITY OF QUEENSLAND
IN PARTIAL FULFILMENT OF THE DEGREE OF BACHELOR OF SCIENCE WITH HONOURS
SCHOOL OF MATHEMATICS AND PHYSICS
NOVEMBER 2024

© Ryan M.T. White, 2024.

Typeset in L^AT_EX 2_ε.

The work presented in this Thesis is, to the best of my knowledge and belief original, except as acknowledged in the text, and has not been submitted either in whole or in part, for a degree at this or any other university.



Ryan M.T. White



Abstract

The most massive stars end their lives as extremely hot, luminous Wolf-Rayet (WR) stars, before dying in supernova explosions. Many of these Wolf-Rayet stars evolve with a massive companion in a stellar binary, where their interactions shape the surrounding environment and their mutual fate as supernova or gravitational wave progenitors. A spectacular interaction that occurs in a subset of Wolf-Rayet binaries is the colliding wind nebula, where shocked wind of the two stars efficiently produces dust that traces the orbital motion of the binary. In this way, we can infer the orbit of these systems using their spiral nebulae as cosmic fingerprints, where a spectroscopic orbit would otherwise be too difficult to observe. The Apep system stands out among the Wolf-Rayet colliding wind binaries, being the only confirmed WR+WR in that Galaxy that produces such a nebula. In this thesis we present the first *James Webb Space Telescope* imagery of this one-of-a-kind stellar laboratory, together with new epochs of Very Large Telescope images. These data allow us to uniquely infer the orbit of Apep’s inner binary, in particular that the motion of the stars must be more eccentric and with an orbital period of 234 ± 10 years, twice as long as previous estimates. We also find that the O-type supergiant to the north of Apep’s WR+WR binary is dynamically bound to the system – imprinting its own wind-blown cavity into the nebula – making Apep a hierarchical triple and yielding the first direct evidence of local dust destruction in a WR system. In parallel, we present the first model nebula of the candidate WR+WR system WR 48a finding that there is only one WR-type star in that binary, further distinguishing Apep as the only confirmed WR+WR binary. To model these nebulae, we developed a geometric model that is 100 times faster than the state of the art and is able to, for the first time, produce the associated infrared light curve of the colliding wind nebula. The entire model pipeline is differentiable and future statistical inference with gradient-based methods is now possible.

Acknowledgements

I wouldn't have gotten through the year without the unending love and support of my partner, Rika. Thank you for trying so very hard to look interested as I've rambled and ranted my way through this year and the last seven. Truly, no words can do justice for what you mean to me.

I would have quickly been driven mad without the numerous coffee meetups with my friend Katelyn. Even though we can't agree on what films are good or not, you really have convinced me that M Dwarf stars are worthy of love, and I hope I've done the same to you with Wolf-Rayets. We will publish that paper some day.

Thank you to my office mates, Narise, Doni, Tweedie, and Sascha for making this year a bit more bearable, and for helping me hide among the people who do the real physics. At the same time, I need to thank Tennille – doing her honours in the UQ Psychology department – for reminding me how much of a physicist I really am.

This Thesis would not be as pretty without the work of Shashank, who I thank for processing (with Ben) probably the prettiest JWST picture that anyone has ever seen, and for giving some help or an ear here and there over the course of this year. Much in the same way, I must thank Hugh for the numerous friendly chats and statistics help (often in the same conversation).

My thesis wouldn't be in the state that it is without the helpful conversations and generosity of Yinuo. You have such a great intuition for this Wolf-Rayet geometry, and it was incredibly kind of you to let me use your VLT and JWST data for my thesis.

I of course have to thank Peter's group at USyd for hosting me in person and over FOCI. In particular I have to thank Louis, Max, and Grace for adopting me in Sydney and Canberra and showing me around.

I'm grateful to the University of Tasmania astronomy department, the Mount Stromlo Student Seminars LOC and attendees, the UQ SURC organising committee and attendees, and the UQ astronomy department all for listening to me practise and give talks. The enthusiasm in all of your questions reinforced my passion for this project.

I must thank the Andy Thomas Space Foundation for generously contributing a \$10k AUD scholarship towards this Honours project. The cost of living in the 2020s is prohibitive, and this thesis would not be the work it is without the financial safety net that the foundation had given me.

Although it took my mind away from my thesis for a good while, writing a cosmology paper with Tamara was such a good learning experience. The fact that you had faith in me in writing a full publication after only a ~ 4 week winter project speaks volumes about your belief in your students, and that improved my self confidence going into my Honours.

Many wonderful things have come from a coffee and chat with my co-supervisor, Peter. I'm thankful for the introductions to various people I've had through you, and of course for finally convincing me to play pinball; I hope those permutations of Apep highscores remain for a long time.

This project would not have been possible without the ideas and support of my supervisor, Ben. From the get go, you were encouraging me when there was progress and you were quick to blame the demons in my code when things weren't quite working. The feedback you've given on my written and oral work is second to none, and I've become a better communicator as a result. You have a keen eye for opportunity, and I attribute the entirety of my extracurricular success this year to the emails you forward me at 11pm. Even though we can't agree on what films are good or not, I think we're of the same mind in thinking that Wolf-Rayet stars are pretty cool.

I dedicate this thesis to the memory of my friend Gauthier. Although separated by lands and seas in life, I'll see you now whenever I look to the stars.

Contents

Abstract	v
Acknowledgements	vii
List of Figures	xi
List of Tables	xiii
Glossary of Abbreviations and Symbols	xv
1 Introduction	1
2 Wolf-Rayet Stars and Colliding Wind Binaries	3
2.1 Massive Stellar Evolution and Wolf-Rayet Stars	3
2.2 Wolf-Rayet Stars as Supernova Progenitors	7
2.2.1 Metallicity in Different Epochs	8
2.3 Binary and Multiple Systems	8
2.4 Colliding Wind Binaries	9
2.4.1 A Rogues' Gallery of Key CWBs	11
2.4.2 Photometry and Spectra	12
2.4.3 Direct Imaging	14
2.4.4 Hydrodynamical Simulations	15
2.4.5 A Geometric Model	16
3 Creating a Fast and Differentiable Geometric Model	19
3.1 The Basic Ring Model	21
3.2 Higher Order Effects	24
3.2.1 Azimuthal and Orbital Variation in Dust Production	25
3.2.2 Acceleration in the Dust Shell	27
3.2.3 Modelling Wind Anisotropy	28
3.2.4 Miscellaneous Features and Details	30
3.3 A Fully Differentiable Geometric Model	32
3.4 Graphical User Interface	34
3.5 Modelling Light Curves	35
4 The First Model of WR 48a	39

4.1	Geometry Using Archival Data	39
4.2	Is WR 48a a WR+WR Binary?	43
5	The Geometric Model as a Probe into the Physics of Apep	45
5.1	Updated Parameters from the VLT and JWST	45
5.2	Modelling of Tertiary Effects	52
6	Conclusions and Future Work	57
6.1	Future Work	58
A	Statistical Inference with the Geometric Model	61
A.1	Hamiltonian Monte Carlo	61
A.2	Inference on Simulated Data	63
A.2.1	Towards Inference with Apep’s Four VLT Epochs	67
B	Velocity Maps with the Geometric Model	69
	References	71
	List of External Links	81

List of Figures

2.1	P-Cygni Profile of Apep	5
2.2	Images of WR 104, Apep, and WR 140	10
2.3	The \sim 50 year light curve of WR 137	13
3.1	The basic setup of the geometric model	20
3.2	Rendering a point cloud into an image	24
3.3	Azimuthal and orbital modulation change particle weighting	26
3.4	How higher order effects change plume geometry	27
3.5	Anisotropy in dust plume arising from star inclination	29
3.6	Plume lobes arising from wind anisotropy	30
3.7	Smooth histogram involves spreading out particle weights	32
3.8	Smooth and normal histogram comparison	33
3.9	Our geometric model GUI	34
3.10	Our modelled light curve of WR 140	37
4.1	Our modelled geometry of WR 48a	40
4.2	Our modelled light curve of WR 48a	42
5.1	The four epochs of VLT/VISIR Apep images	46
5.2	The three filter JWST/MIRI images of Apep	47
5.3	Colour composite JWST image of Apep	48
5.4	Our geometric fit of Apep to all images	49
5.5	The cavity in Apep's plume from the tertiary star	52
5.6	Movement in the cavity over concentric shells	54
A.1	Contour plot of HMC on simulated data	64
A.2	Samples of HMC on simulated data	65
A.3	Comparison of simulated image to the fit image	66
A.4	Summary statistics of the goodness of fit to the simulated image	66
B.1	Radial and tangential velocity maps of Apep	70

List of Tables

4.1	Best-fitting parameters for the WR48a system.	41
5.1	Best-fitting parameters for the Apep system.	50
5.2	Best-fitting parameters of Apep's plume cavity	53

Glossary of Abbreviations and Symbols

The following list is neither exhaustive nor exclusive, but may be helpful.

Glossary of Abbreviations/Acronyms/Initialisms

We list the commonly used short form names in alphabetical order.

ALMA – Atacama Large Millimeter Array

au – Astronomical Unit

BH – Black Hole

BSG – Blue Supergiant (star)

CoM – Centre of Mass

CWB – Colliding Wind Binary

cWR – Classical Wolf-Rayet (star), evolved off the main sequence

GRB/LGRB – Gamma Ray Burst and Long Gamma Ray Burst respectively

HMC – Hamiltonian Monte Carlo

HPC – High-Performance Computing

IMF – Initial Mass Function

JWST – *James Webb Space Telescope*

LBV – Luminous Blue Variable (star)

LMC – Large Magellanic Cloud

MCMC – Markov Chain Monte Carlo

MIRI – JWST Mid Infrared Instrument

NUTS – No U-Turn Sampler

OB – O or B type star, i.e. those of high mass, temperature, and luminosity

pc – Parsec (parallax arcsecond)

- PN/PNe – Planetary Nebula and Nebulae (plural form) respectively
- RSG – Red Supergiant (star)
- SMC – Small Magellanic Cloud
- SN/SNe – Supernova and Supernovae (plural form) respectively
- VISIR – VLT Imager and Spectrometer for mid Infrared
- VLT – Very Large Telescope
- VLTI – Very Large Telescope Interferometer
- WCR – Wind Collision Region
- WC/N/O – Wolf-Rayet star of Carbon, Nitrogen, or Oxygen type respectively
- WNh – WN star with hydrogen spectra, on the main sequence
- WR – Wolf-Rayet (star)

List of Symbols

- G – Gravitational constant
- M_{\odot} – Solar mass
- R_{\odot} – Solar radius
- M, E, ν – mean, eccentric, and true anomaly (respectively)
- $e, a, i, \Omega, \omega, \nu$ – the orbital elements, respectively: eccentricity, semi-major axis, inclination, longitude of the ascending node, argument of periaxis, true anomaly
- ϕ – orbital phase

1

Introduction

The understanding of massive stars in our Galaxy is foundational to our understanding of the wider Universe. Massive stars are born from the densest regions within clouds of molecular gas, and begin shaping their environment and their galaxy from the outset. These stars evolve very quickly – on the order of a few to tens of millions of years – and produce an abundance of metals as they do so. As they live, massive stars eject material into the interstellar medium through their strong stellar winds and through episodic eruptions. As they die, massive stars enrich the chemical content of their galaxy through powerful supernova explosions. These two processes from massive stars, stellar mass loss and supernovae, are responsible for the overwhelming majority of the earliest metal content in the Universe. In particular, the Wolf-Rayet (WR) stage of stellar evolution contributes a majority of this early carbon, nitrogen, and oxygen with which our Solar System and life as we know it was formed.

These Wolf-Rayet stars are the rare and extreme end-of-life phases of the most massive stars that have shed their hydrogen envelopes through binary interactions and/or the strongest known stellar winds. Only 1 in every billion stars within the Galaxy are of WR-type, and given that they are among the most intrinsically luminous stars, a larger population would be readily apparent if they were not so rare. Despite their intrinsic rarity, these stars exert a profound influence on the Milky Way, for example in their role as progenitors of the most energetic core-collapse supernovae: Type Ic supernova. These supernovae have been associated with long gamma-ray bursts, whose energy output would be catastrophic to life on Earth were one to occur close enough and if oriented along our line of sight. Exactly how WR stars in the modern Universe may produce a gamma-ray burst is yet to be conclusively understood, but it is hypothesised that certain binary interactions may impart enough angular momentum onto the progenitor WR star for this to take place. Since a majority of massive stars are formed in binary or multiple systems, WR binaries are of particular interest.

With no direct in-situ observations of a Wolf-Rayet precursor undergoing a supernova

explosion, the current population of WR stars must be closely studied to advance our understanding of the final moments of massive stars. Of particular interest are the colliding wind binaries (CWBs) that host WR stars. When a WR star and a sufficiently massive companion are in a close binary, we often observe a wind collision region (WCR) where carbon-rich dust is nucleated at the collision interface between the stellar components' winds. This dust is bright in the infrared and traces the orbital motion of the binary itself, forming an intricate spiral structure as the dust plume expands away from the system. This process is analogous to a sprinkler, throwing out material along a narrow cone while rotating with the orbital motion of the binary stars. When the orbital motion is inclined to be almost entirely in the plane of the sky, the dust nebula forms an Archimedean spiral, or a so-called ‘pinwheel nebula’. This spiral structure is sensitive to the orbital and stellar parameters of each binary system, and so encodes precisely the underlying physics of CWBs and by extension WRs and their companions.

Apep, a WR+WR system which is perhaps one-of-a-kind in the Galaxy, stands out as one of the most interesting examples in an already unique class of star system. It is surprising to find a binary system with both stars in this short-lived phase of stellar evolution, and the evolutionary pathway permitting this is an open question. Apep’s orbit is too compact and too distant for us to easily resolve orbital motion without repeated interferometric imaging over a long timespan, an effort which is further complicated by the dusty colliding wind nebula enshrouding the system. Therefore, inferring the physics of Apep through its spectacular nebula will help us understand the most likely gamma-ray burst progenitor in the Galaxy.

The progression of this thesis is as follows. In Chapter 2 we describe physical characteristics of Wolf-Rayet stars and their influence on their environments, in particular the binary systems that produce colliding wind nebulae. We pay close attention to the geometric modelling that reproduces nebulae so well, and in Chapter 3 we present our new geometric model that is differentiable, orders of magnitude faster than the state of the art, and implements more physical phenomena than ever before. Our new model comes more accessible with a graphical user interface which we use to infer the first nebula model for the WR 48a system in Chapter 4. Our WR 48a model is supported by the simulated infrared light curve of the system – the first of its kind – that suggests that the candidate WR+WR system must have only one WR star at its centre. This posits Apep (a confirmed WR+WR system) as a singular laboratory for binary Wolf-Rayet physics in the Galaxy; in Chapter 5 we support this by revealing new *James Webb Space Telescope* and Very Large Telescope imagery of the Apep system, which urges an overhauled perspective on the WR+WR orbit and confirms the physical association of the northern O star with the inner WR+WR binary. Finally in Chapter 6 we conclude and summarise our findings, notably suggesting avenues of future research on Apep and using our geometric model.

“I could put my thumb up to a window and completely hide the Earth. I thought, ‘Everything I’ve ever known is behind my thumb.’”

Jim Lovell, Forbes Magazine, 2016

2

Wolf-Rayet Stars and Colliding Wind Binaries

In this Chapter we begin by reviewing the stellar evolution of massive stars to the Wolf-Rayet stage. We go on to describe the properties of Wolf-Rayet stars and their role in the evolution of galaxies (chemically and otherwise). Since massive stars are often born and evolve in binary systems, we discuss the prevalence of WR binary systems and their unique observables. Naturally this leads to the presence of colliding wind binaries, where we overview their impact on the Galaxy, the methods used to model these, and the gaps in these methods (in particular the geometric modelling).

In this thesis we study only the classical Wolf-Rayet (cWR) stars that are the evolutionary product of the most massive stars; low-mass, stripped stars of WR type are known to exist at the heart of many planetary nebulae (PNe; [Wright, 1918](#); [Gorny & Stasińska, 1995](#)), however their evolutionary histories are quite distinct and do not give rise to the colliding wind binaries that we discuss herein.

2.1 Massive Stellar Evolution and Wolf-Rayet Stars

Massive stars, those of order 10 to $100M_{\odot}$, like other stars form in giant molecular clouds ([de Wit et al., 2005](#); [Tan et al., 2014](#)). The initial masses of stars formed within these molecular clouds follow an initial mass function (IMF) such that low mass stars are formed in much higher number than high mass stars ([Miller & Scalo, 1979](#); [Kroupa, 2001](#)). Even though formed in fewer numbers, the much greater luminosity inherent with massive stars means that they are the dominant force in shaping their parent molecular clouds once star formation begins ([Motte et al., 2018](#)) and even the appearance of their host galaxy ([Cameron et al., 2024](#)), ionising gas in so-called HII regions. As a molecular cloud contracts under its self-gravity, the cloud fragments and forms stars along filamentary structure ([Hoyle, 1953](#); [Chira et al., 2018](#); [Hacar et al., 2023](#)). The closest forming protostars along these filaments interact gravitationally and, supported by complex hydrodynamical processes, often form binary or

multiple systems. As massive stars naturally form in regions of higher density (and in addition to their correspondingly higher gravitational influence), there is a strong preference for binarity/multiplicity in massive star systems, and with companion stars tending towards comparably high masses (Sana & Evans, 2011; Sana, 2017; Offner et al., 2023).

Once a molecular gas core has contracted into a massive protostar, the protostellar core quickly becomes convective and hot enough to fuse hydrogen, helium, and carbon (Carroll & Ostlie, 2017; Motte et al., 2018); the protostar enters the main sequence as an O or B type star. It is in this main sequence phase that all stars spend the majority of their lives, predominately burning hydrogen into helium and heavier elements via the CNO cycle (Maeder, 1983; Woosley et al., 2002; Carroll & Ostlie, 2017). After several million years the hydrogen in the convective core is exhausted and the star leaves the main sequence, forming heavier elements via the triple- α process (Salpeter, 1952; Woosley et al., 2002; Carroll & Ostlie, 2017).

During a phase of core/shell helium or carbon-oxygen burning, massive stars usually evolve into supergiant stars. Depending on the initial mass of the star, this could mean a red or blue supergiant (RSG and BSG respectively), or a luminous blue variable (LBV) star for the more massive stars (Groh et al., 2013). Whether through one or a combination of mass loss mechanisms such as stellar winds and/or binary mass transfer, the highest mass ($\gtrsim 20M_{\odot}$) stars shed their outer hydrogen envelopes leaving an exposed helium star or Wolf-Rayet star (Paczyński, 1967; Conti, 1975; Crowther, 2007). The exact progression of envelope/mass loss is a topic of active research, and depends very sensitively on the mass, metallicity, and rotation of the star among other variables (Meynet et al., 2011; Sander & Vink, 2020; Josiek et al., 2024); the most massive stars ($> 25M_{\odot}$) may skip the supergiant phase altogether and evolve off the main sequence directly into a WR star (Crowther, 2007; Groh et al., 2013).

Wolf-Rayet stars are characterised by extremely strong, dense stellar winds driven by emission lines of helium, carbon, nitrogen, and/or oxygen (Wolf & Rayet, 1867; Hamann et al., 2006; Crowther, 2007). Despite the hydrogen envelope shedding and high mass loss rates, WRs remain very massive at $\gtrsim 10M_{\odot}$, depending on their spectral type. Within the Wolf-Rayet classification, there are 3 main sub-classifications labelled for carbon, nitrogen, and oxygen: the WN type (owing to strong He and N lines), the WC type (owing to an absence of N and prominence of C), and the WO type (an absence of N and strong presence of O) (Gamow, 1943; Crowther, 2007). Within each of these sub-classifications there exist subtypes that describe the relative strength of individual emission lines (WN2-11, WC4-9, and WO1-4) and hence more specific chemical and physical properties of the stars. The relationship between the different classes of WR stars has long been understood to be an evolutionary progression from one type to another (depending on the initial mass of the star; Conti, 1975; Abbott & Conti, 1987), but this has been recently challenged (McClelland & Eldridge, 2016, suggesting that the subtype is mass-dependent) indicating that even the fundamental properties of these stars are still a topic of active research.

In the last 30 years, there has been interest in a peculiar class of WR star: the WNh type. Wolf-Rayet stars of the WNh sub-classification are categorically disparate from the classical WRs of C/N/O type; while they do display strong helium and nitrogen spectral lines characteristic of WN stars, they also exhibit hydrogen lines (hence the appended “h”)

which suggests either a transitory stage of evolution or a different phenomenology altogether ([Shenar, 2024](#)). The $60 - 100M_{\odot}$ mass of these stars – a factor of a few higher than typical WC/WN stars – cements these as massive stars still undergoing core-hydrogen burning, although perhaps near the terminal-age main sequence ([de Koter et al., 1997](#); [Smith & Conti, 2008](#); [Shenar, 2024](#)). Still, their mass loss rates are many times higher than ordinary main sequence O stars and their winds are expected to be radiatively driven, making all but their chemistry similar to classical Wolf-Rayets at first glance.

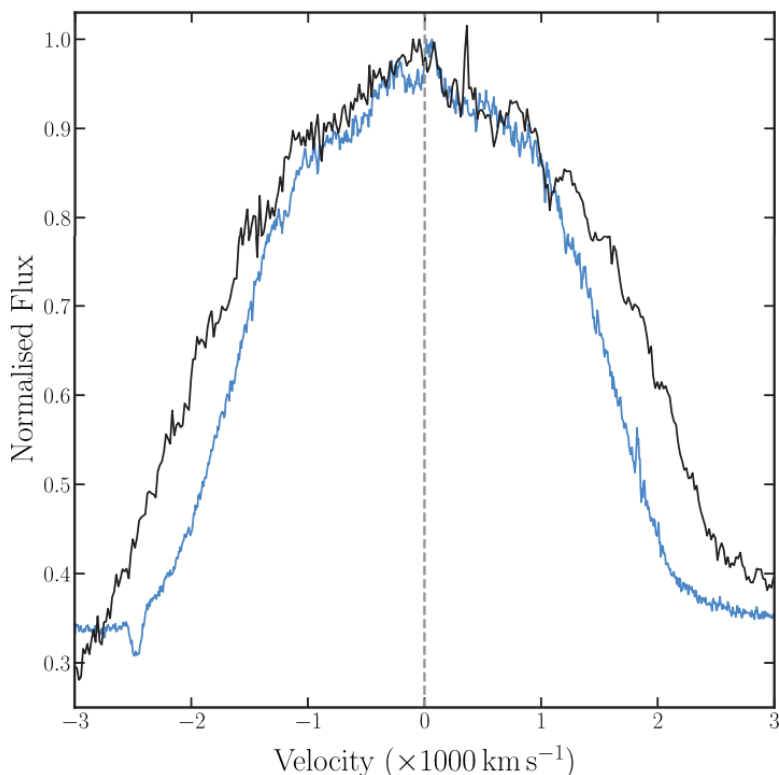


FIGURE 2.1: The spectrum of the WR+WR system Apel shows some lines with a P Cygni profile (here the He II 1012 nm line in blue) and some without (the black C III 971 nm line) – an indication of two stars with different wind speeds ([Callingham et al., 2020](#)). Already converted from wavelength into radial velocity, we see the characteristic absorption dip at about -2500 km s^{-1} .

Despite unknowns in their evolutionary progression, much about the phenomenology of Wolf-Rayet stars is well known and observed. Of particular note is their uniquely strong stellar wind. There are multiple observational probes that reveal these winds, both intrinsic (e.g. line broadening in spectra) and extrinsic (in the interaction with the WR surrounds).

Perhaps the most robust indicator of a WR's wind velocity is in its spectrum. Observing individual emission lines in the spectrum of a star often shows a P Cygni profile (Figure 2.1), where the line is broadened by the expansion of the luminous wind in both radial directions (simultaneous red and blue shifting), and absorption of star light from wind material directly along the intermediate line of sight to the star imposes a strongly blueshifted absorption line. By analysing the shape of this line profile, highly precise wind speeds are obtained ([Willis,](#)

1982; Crowther, 2007; Callingham et al., 2020; Williams et al., 2021). Zavala et al. (2022) also showed that by taking several spectra at different regions of a WR nebula, a three dimensional geometric model of the nebula can be produced that encodes information not only about the wind speed, but direction too.

Interactions of the Wolf-Rayet wind with the surrounding environment, such as the creation of nebulae or cavities in parent molecular clouds, strongly constrain their wind physics. These strong interactions arise not only because of the high wind speed from WR stars, but from some of the highest mass loss rates of any stellar type (comparable only to LBVs and RSGs). It is understood that this mass loss is primarily driven by the radiation pressure of metallic emission lines (Castor et al., 1975; Crowther, 2007), the WR stars themselves being near the Eddington limit (Gräfener & Hamann, 2008; Gräfener et al., 2011). Mass loss rates for WR stars are typically on the order of $10^{-5} M_{\odot} \text{ yr}^{-1}$ (Barlow et al., 1981; Crowther, 2007), and so this coupled with the high wind velocity means that WR winds have exceptionally high momentum.

Over the course of the WR phase, the stellar winds of the stars often form bright nebulae (see: NGC 2359, NGC 6888, Sh 2-308) fuelled by their mass and enriched chemistry; studying the multi-epoch expansion of these nebulae reveals the distances to these systems if the wind velocity is well constrained (or vice versa). One such case where nebula expansion has been observed is in the wind nebula M1-67 around WR 124 (Marchenko et al., 2010), which allowed for an independent distance estimate to the system; this has also been done with the WR PNe BD+30°3639 (Schönberner et al., 2018). As a secondary direct imaging probe of WR winds, WR stars have been observed forming cavities in the molecular material of their natal environment via ablation from their stellar winds (Baug et al., 2019, see also Dale et al., 2013 for simulations of this). This same process has been seen forming shocks when the wind interacts with the surrounding gas, often triggering more star formation (Cichowski et al., 2015).

Much of the mass within the stellar winds is inhomogeneous, being clumpy and nucleating into dust at sufficient distance. Although WR stars have mostly steady winds, there is an observed small-scale stochasticity in the winds that manifests as multi-epoch line variation (Michaux et al., 2014; Chené et al., 2020); hence, the WR stellar wind can be chemically inhomogeneous. On a related note, circumstellar dust is produced around many WR stars, especially those of WC subclassification (Allen et al., 1972; Gehrz & Hackwell, 1974; Lau et al., 2021). How delicate dust molecules are formed around WR stars – some of the hottest and most ionising astrophysical environments in existence – is still a topic of active research. The clumpy wind is one proposed avenue for dust formation, where the high opacity and density within clumps provides a sort of shielding from the environment where molecules can form (Cherchneff et al., 2000). We observe orders of magnitude more efficient dust production around binary stars containing a WR, where turbulent wind compression occurs in the shocked region between the two close massive stars, providing a nurturing environment for dust creation and survival (Soulain et al., 2023). This will be discussed more in Section 2.4.

2.2 Wolf-Rayet Stars as Supernova Progenitors

Wolf-Rayet stars are convincing candidates for Type Ib/Ic supernovae (SNe Ibc) progenitors: WRs are massive pre-supernova stars that lack hydrogen spectra, as do SNe Ibc ([Filippenko, 1997](#); [Crowther, 2007](#); [McClelland & Eldridge, 2016](#)). There is some discussion of an alternate SNe Ibc channel in [Smartt \(2009\)](#) where a lower mass star may lose its hydrogen envelope via binary interactions prior to undergoing supernova (not dissimilar to one of the proposed channels of WR formation; [Paczyński, 1967](#)). The consensus is that at least some combination of the WR progenitor model and this alternate scenario explain the observed population of SNe Ibc (see: [Eldridge et al., 2013](#); [Pellegrino et al., 2022](#); [Karamehmetoglu et al., 2023](#)).

Despite their intuitive connection, no WR stars have been definitively shown to be SNe Ibc progenitors with pre-supernova imaging of galaxies. [Kilpatrick et al. \(2021\)](#) identified the likely progenitor of Type Ib supernova SN2019yvr in *Hubble Space Telescope* imagery taken 2.6 yr prior to explosion. They found that neither a clear-cut WR nor a lower mass binary can adequately describe the SN progenitor, indicating that perhaps a sudden change in the observables of SNe Ibc progenitors take place just prior to explosion, e.g. extreme mass loss. The lack of attribution could also plausibly be ascribed at least in part to the reduced detectability of WR stars at extragalactic distance ([Pledger et al., 2021](#)).

On the other hand, connections have been made between Type Ic supernovae and gamma-ray bursts (GRBs). Gamma-ray bursts are a class of energetic transient whose durations distinctly fall into two categories of ‘short’ and ‘long’, with several sources appearing isotropically on the sky each day ([Woosley & Bloom, 2006](#)). Short GRBs, of order $\lesssim 2$ s, are understood to be the result of kilonovae, the breakup of degenerate neutron stars during gravitational wave induced binary inspiral ([Berger, 2014](#)). In contrast, long GRBs (LGRBs), of order $\gtrsim 2$ s, arise from the relativistic jets produced in the core-collapse of highly rotating massive stars ([Woosley & Heger, 2006](#)). In fact, several SNe Ic-BL events, SNe Ic with especially broad spectral lines indicative of relativistic ejecta, have been definitively associated with LGRBs and fast X-ray bursts ([Galama et al., 1998](#); [Ashall et al., 2019](#); [van Dalen et al., 2024](#)). Interestingly, not all of these SNe Ic-BL have been associated with LGRBs, indicating that either the jets are highly collimated (and hence their visibility being very direction dependent) or there remains a significant gap in understanding ([Siebert et al., 2024](#); [van Dalen et al., 2024](#)).

The consensus on the LGRB mechanism is in the collapsar model, where at the time of supernova the innermost core collapses into a black hole (BH). The surrounding core, having a high enough angular momentum to form a disc, produces polar jets as a result of angular momentum loss as matter accretes onto the natal BH ([Woosley, 1993](#); [Dean & Fernández, 2024](#)). For a star to do this, it must be rotating extremely rapidly. This should be the case for stars that have been efficiently mixed during their lifetimes ([Woosley & Heger, 2006](#)), and hence stars that are effectively free of hydrogen at supernova as a result. Therefore it is not a requirement that GRBs have no hydrogen line association (and hence a Type I vs a Type II SN), but rather a consequence of the evolutionary process that gives rise to GRBs. Because of this, helium and metal-rich stars emerge as the leading candidate progenitors for SNe Ic/-BL. There is a significant body of simulations linking WR to SNe Ic and GRBs

through the collapsar model (McClelland & Eldridge, 2016; Aguilera-Dena et al., 2018), especially those with high rotation at preferentially low metallicity (Detmers et al., 2008).

2.2.1 Metallicity in Different Epochs

Modern Wolf-Rayet stars are synonymous with metallic line-driven winds. These winds, along with magnetic effects, are known to be efficient at dissipating angular momentum from hot stars (Woosley & Heger, 2006; Ud-Doula et al., 2009). This, in conjunction with the more efficient mass-loss at high metallicity (Vink & de Koter, 2005; Gräfener & Hamann, 2008), means that we generally expect Galactic WRs to be slower rotators than those in less-evolved galaxies. There is a strong dependence on the rotation speed of a progenitor star to its LGRB status (and also between the spin of the collapsar BH to the GRB jet collimation; Hurtado et al., 2024), and so the logical conclusion is that we should expect fewer or no LGRBs in evolved galaxies with high metal content.

Indeed, there is strong indication from stellar models that low-metallicity massive stars should be rapidly rotating (Chiappini et al., 2006; Vink & Harries, 2017). This motivates searches for LGRB progenitors in dwarf and/or satellite galaxies where the metal content can be orders of magnitude below solar metallicity (Tolstoy et al., 2009). There has been some plausible, if inconclusive, evidence of rapidly-rotating WRs in the Large Magellanic Cloud (Shenar et al., 2014; Vink & Harries, 2017), lending credence to this idea. Therefore we expect that LGRBs are efficiently produced in the early universe or in dwarf galaxies with less enriched chemical content.

One proposed channel for fast spinning massive stars, and hence LGRB events, within chemically evolved galaxies like the Milky Way is in the tidal spin up from a closely orbiting companion star. Early studies suggest that this mechanism is improbable at solar metallicity and marginally more likely at low metallicity (Detmers et al., 2008). More recently, population synthesis studies have shown this to be an efficient mechanism to sustain fast rotation in evolved stars (Chrimes et al., 2020; Bavera et al., 2022), although only in very closely orbiting binaries.

2.3 Binary and Multiple Systems

There is an apparent link in models between the rotation rate of massive stars and their binarity, and there is clear evidence that massive stars often form in binary or multiple systems within the Galaxy (Offner et al., 2023). The question is then how Wolf-Rayet stars fit within the picture of binary/multiple systems, and what this means for their evolution and observation.

Massive O stars on the main sequence are most commonly formed within binary or multiple systems, where their companions are usually massive OB stars too (Shara et al., 2022; Offner et al., 2023). Naturally, as the primary stars in these systems evolve off the main sequence into BSG/RSG or WR stars, they tend to keep their companions. Eventually, the primary star is expected to undergo a supernova in which case the secondary may be ejected as a ‘runaway star’ with high velocity (of order orbital velocity at the time of supernova, up to $\sim 120 \text{ km s}^{-1}$; Eldridge et al., 2011). This means that although surveys may identify single

O/B/WR stars, they may have originally been formed within a binary system (Schootemeijer et al., 2024). Regardless, the Galactic WR binarity fraction is reported as $\sim 40\%$ (van der Hucht, 2001; De Marco & Izzard, 2017) and surveys of the lower metallicity Large and Small Magellanic Clouds (LMC and SMC, $Z \sim 0.5Z_{\odot}$ and $Z \sim 0.2Z_{\odot}$ respectively) suggest similar values indicating that binarity is not a function of metallicity or redshift (Foellmi et al., 2003; Shenar et al., 2020; Schootemeijer et al., 2024).

Just about the only trait common among the Wolf-Rayet binaries is that there are two or more stars per system and one of them is a Wolf-Rayet star. Companions have been found in both very close and very wide orbits, and interestingly there appears to be at least some correlation between orbital period and WR type: WN stars are more commonly found in close binaries, and WC in wide binaries (Dsilva et al., 2020, 2022, 2023). Also, while WR companions are usually similarly (or more) massive O stars, there are several confirmed and tentative detections of unusual companion types. Of particular note is the possible detection of a low mass F type main sequence companion to WR 113, making the system a triple with its known WC8+O8 components (Shara et al., 2022). In the same study the authors propose a detection of a wide orbit (~ 1800 au) WN3-4 companion to the WN7 star WR 120, making it one of the only candidate WR+WR systems. Although not evolved stars, the WR 20a system has an observed WN6h+WN6h binary at its centre in an extremely short ~ 4 day orbit (Bonanos et al., 2004; Rauw et al., 2005; Olivier et al., 2022). WR 48a has been proposed as a candidate WC8+WN8h system on the basis of its spectra (Zhekov et al., 2014), although this is contested in favour of an O star companion classification (Williams et al., 2012).

Apep (WR 70-16) has been confirmed as a WC8+WN4-6 binary due to the superposition of specific spectral lines characteristic of those two classes of WR star, together with a clear wind speed discrepancy in those lines (Callingham et al., 2020, Figure 2.1). At present, Apep is the only confirmed WR+WR system composed of two evolved WR stars. The evolutionary history delivering two Wolf-Rayet stars in the same system at the same time is, like Wolf-Rayet evolution in general, an open question and made still more puzzling by the disparate spectral classes (WC and WN). Early studies even questioned the observability of these systems (Vrancken et al., 1991), although technique and instrumentation development has provided clear success in detection of WR binaries. With a lack of population synthesis studies showing a clear WR+WR formation channel, the best indication may lie in the study of less evolved massive stars (e.g. in the WN6h+O3/WN7 system R145; Shenar et al., 2017).

2.4 Colliding Wind Binaries

Given that Wolf-Rayet stars are known by their intense winds and high binarity fraction, it naturally arises that we should expect some interaction at the collision interface between the winds of the WR star and its massive companion (Cherepashchuk, 1976; Prilutskii & Usov, 1976). Indeed, there is a modest population of WR+O/B/WR binaries whose dense winds collide to produce dust nebulae that expand outwards from the system. We show a diversity of such systems in Figure 2.2, showing that even the same physics can produce vastly different observed nebula geometry.

All dust producing colliding wind binaries observed to date are composed of a cool,

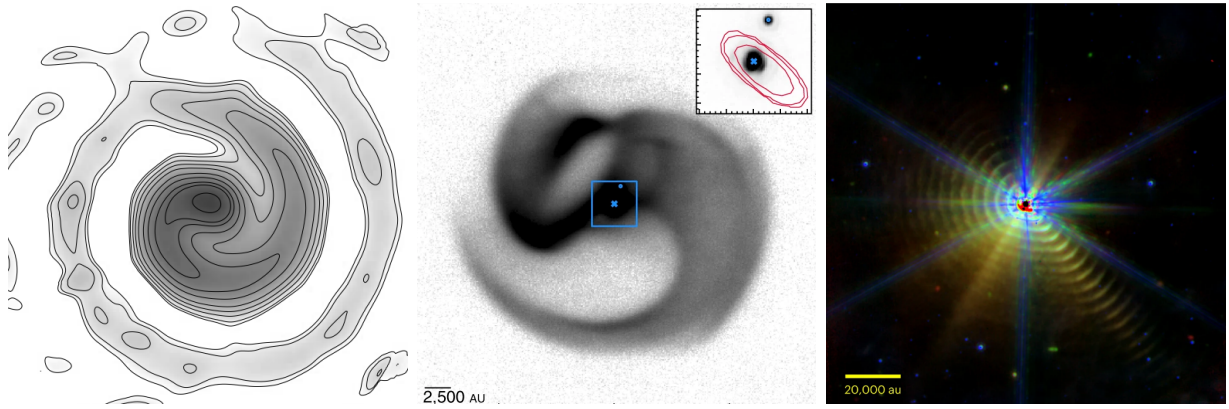


FIGURE 2.2: The last ~ 20 years has seen much progress in imaging the dust nebula colliding wind binaries. *Left:* The first imaged CWB, WR 104 (Tuthill et al., 2008), done so by reconstructing interferometric data. *Centre:* The only confirmed WC+WN system in the Galaxy, Apel (Callingham et al., 2019), taken with the VISIR instrument on the Very Large Telescope (VLT). *Right:* The first CWB directly imaged with the *James Webb Space Telescope*, WR 140 (Lau et al., 2022), shows dust production evident over several concentric shells.

late type WC star whose wind contains the key ingredients for dust. In the wind collision region, these ingredients are mixed and subsequently shielded from the ionising radiation in the turbulent conical shock boundary (Hendrix et al., 2016). The result is a very bright dust nebula in the infrared whose geometry and periodicity reveal otherwise hidden orbital parameters of the system.

The first association of dust production to the colliding wind mechanism was in the periodic infrared brightening of WR 140 (Williams et al., 1978, 1987), where the wind collision region and subsequent turbulent shock provides an ample environment for dust production (Williams et al., 1990; Usov, 1991). The spiral structure in these nebulae arise from the shock cone produced at the collision interface wrapping around from the orbital motion of the stars.

With this in mind, we see so called ‘pinwheel nebulae’ produced in binary systems where the components have roughly circular orbits and orbit roughly in the plane of the sky (e.g. in WR 98a and WR 104, the latter shown in Figure 2.2). Archimedes first described spirals in which the radial extent of a point on the curve is determined purely by its outwards velocity and angular coordinate (Archimedes, 2017, originally in approx. 225 BCE),

$$r = v \cdot \theta \quad (2.1)$$

For the circularly orbiting CWBs that constantly produce dust, these Archimedean spirals trace the nebula geometry exceptionally well since the dust position is described by Equation 2.1 to first order. The binary systems with elliptical orbits deviate from the typical spiral shape, often associated with orbital modulation in the dust production that manifests as a ‘turn on’ and ‘turn off’ in the spiral (see Apel, WR 140 in Figure 2.2). This, coupled with the range of inclinations that these systems can have relative to our line of sight, means that no two colliding wind nebulae appear the same despite a consistent formation mechanism.

2.4.1 A Rogues' Gallery of Key CWBs

We present here some of the most unique and significant (historically or otherwise) Wolf-Rayet colliding wind binaries for ease of reference.

Apep One of the only confirmed WR+WR systems, and certainly the only one of these known to harbour a WC with a dust nebula (Cunningham et al., 2020), Apep was identified as a bright X-ray and radio source and potentially the brightest of all the CWBs. It was recently observed with the VLT which showed its spiral dust nebula structure (Cunningham et al., 2019; Han et al., 2020). Possibly a triple system, there is an O8 star very close to the north of the WR+WR inner binary with some indication of association. This system is the primary object studied within this thesis, and is discussed more in Chapter 5.

WR 48a At present, this is the only other candidate WR+WR CWB – specifically of WC8+WN8h classification (Zhekov et al., 2014) – found to be in an orbit with eccentricity $e \sim 0.6$ (Williams et al., 2012). This was one of the first objects to be identified as a colliding wind binary (Danks et al., 1983), and was first directly imaged in Marchenko & Moffat (2007). Like Apep, WR 48a has a relatively long orbital period of ~ 32 years and displays variable dust production throughout its orbit (although there is no evidence of a complete dust ‘turn off’ in 48a as in Apep). We discuss WR 48a as a candidate WR+WR binary in Chapter 4.

WR 98a One of the first colliding wind nebulae to be directly imaged, this system showed the first imaging evidence of inclination effects in a pinwheel nebula (Monnier et al., 1999), in contrast to the Archimedean spiral of WR 104.

WR 104 As the first colliding wind binary to be directly imaged, WR 104 emerged as the prototype ‘pinwheel nebula’ from the clear evidence of orbital motion in its dust plume (Tuthill et al., 1999). This system has been the subject of intense study, particularly in hydrodynamical simulations and the application of pinwheel structure to other CWB nebulae. Like WR 98a, WR 104 is a reasonably short period WC+O binary ($\lesssim 2$ years) in a very circular orbit (Tuthill et al., 2008). Recently, a B star distant from the WC+O binary was considered as being associated with the system (Wallace et al., 2002; Soulain et al., 2018), potentially making WR 104 one of the very few known WR triple systems.

WR 112 First imaged in 2002, the colliding wind nebula of WR 112 was the first to visibly reveal concentric shells of dust formation (Marchenko et al., 2002) from its inner WC8+O binary (Lau et al., 2020b). Like the other consistent dust producers listed here (WR 98a, 104), WR 112 has a well constrained eccentricity close to 0 as is evident from its regular concentric shell structure. Notably, the pinwheel nebula structure was incorrectly applied to WR 112’s dust nebula twice, yielding far-off estimates of the nebula expansion speed and the binary eccentricity and inclination (Marchenko et al., 2002; Lau et al., 2017).

WR 125 One of the longer period colliding wind binaries, the WC7+O9III binary shows episodic dust production with a periodicity of 28.1 years ([Endo et al., 2022](#); [Richardson et al., 2024](#)). While not yet imaged, the surrounding dust shell has been suggested as anisotropic and the binary orbit elliptical ([Richardson et al., 2024](#)).

WR 137 One of the three systems first dubbed as ‘Wolf-Rayet’ stars in 1867 ([Wolf & Rayet, 1867](#)), WR 137 is a WC7+O9V colliding wind binary ([Richardson et al., 2016](#)). The infrared light curve shows episodic dust production over an orbital period of about 13.1 years, and the orbital plane of the binary appears to be almost entirely in the line of sight ([Peatt et al., 2023](#); [Lau et al., 2024](#)).

WR 140 The ‘prototype’ colliding wind binary, composed of WC8+O5 stars on a very high eccentricity ($e \sim 0.89$) orbit of about 7.9 years ([Williams et al., 2009](#); [Monnier et al., 2011](#)). This was the first system to be unequivocally identified as a colliding wind binary, in no small part due to its modulation of dust production: the dust seen in Figure 2.2 (right-side) is produced only in a narrow time frame as the stars approach and leave periastron ([Lau et al., 2022](#); [Han et al., 2022](#)), and this reliably repeats on each orbital passage. This is perhaps the most well studied of all CWBs across all wavelengths and imaging techniques.

WR 147 An apparent triple system composed of a WN8, a close unseen companion, and a distant OB star ([Rodríguez et al., 2020](#)). This is the first system to have an observed pinwheel from the inner binary not in the infrared but in the radio. Not only this, but there is a well resolved bow-shock distinct from the pinwheel where the winds collide with the ternary component. This aligns with previous X-ray observations that resolved the system as a double X-ray source: one at the inner binary and another at the WCR of the inner binary relative to the outer companion ([Zhekov & Park, 2010a,b](#)).

2.4.2 Photometry and Spectra

From earliest discoveries through to contemporary studies, direct photometric and spectral observation has been the workhorse tool for understanding colliding wind binaries. Systems exhibiting episodic dust production, especially those with non-negligible eccentricity, yield clear photometric signatures due to their periodic peaks in infrared brightness. This is especially notable in systems such as WR 140 ($P \sim 7.9$ years) and WR 48a ($P \sim 32$ years) where mostly complete light curves have been made since the discovery of CWBs ([Williams et al., 1987, 2012](#); [Peatt et al., 2023](#); [Richardson et al., 2024](#)). This is potentially the most efficient way to discover new CWBs: photometric monitoring can be obtained from sky survey data and only requires discrete snapshots distributed in time (perhaps even when only in the field of another target). Light curve analysis is still being used even recently to discover episodic dust producers that likely lie in CWBs ([Williams, 2019](#)). Not only their in their discovery, but the properties of CWBs can be discerned from the infrared light curve profile which gives a measure of dust production and is therefore a useful tool in monitoring known systems.

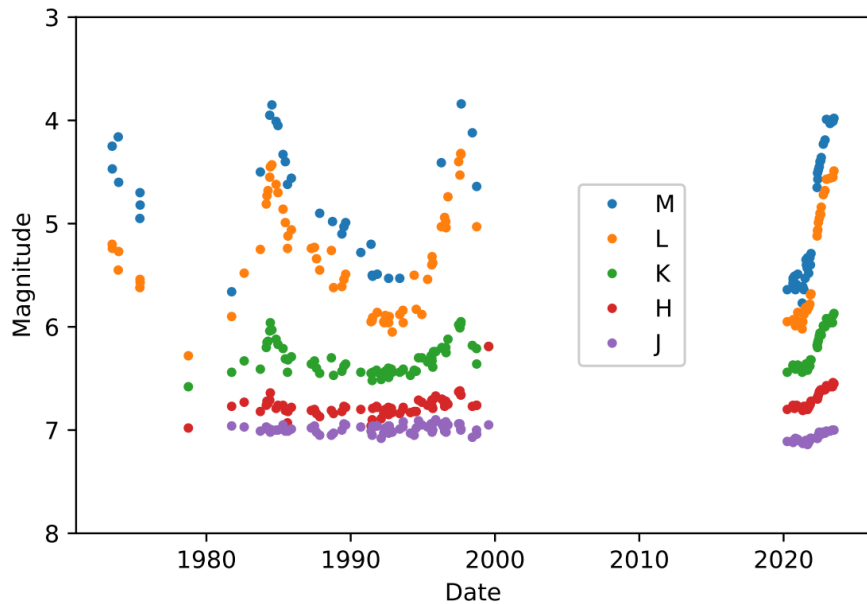


FIGURE 2.3: The long-term infrared light curve of WR 137 shows episodic dust production in the periodic peaks. Shown here is the photometry across different infrared bands (descending band central wavelength in the legend), where the deeper infrared shows brighter total emission as a result of dust production. As the stars approach periastron every ~ 13 years, dust production turns on and eventually turns off after the stars are again sufficiently far apart. Figure from [Peatt et al. \(2023\)](#).

An earlier clue for dust formation in Wolf-Rayet binaries arose from studies of their spectra. Dust produced in these systems is relatively cool (of the order $\lesssim 1000$ K), and so has peak blackbody emission in the infrared ([van der Hucht et al., 1996](#), for dust peaks around $10 - 15 \mu\text{m}$ in WR 48a, 98a, 104, 112, and 118). Circumstellar dust absorbs higher energy light and re-emits in the infrared, therefore spectra have an infrared luminosity far in excess of dust-free stars ([Gehrz & Hackwell, 1974](#); [Williams et al., 1978](#)). Analysing the spectra of these systems remains a key tool in understanding their wind composition, and also their orbits (for example the spectral decomposition of WR stars in [Callingham et al., 2020](#)).

A recent spectral analysis of a dust shell of WR 140 suggested that there exists not just one infrared peak of carbon dust emission, but two: one dust species of $T \sim 1000$ K and grain size $\sim 1 \text{ nm}$, and another of $T \sim 500$ K and size $30 - 50 \text{ nm}$ ([Lau et al., 2023](#)). The analysis further showed that the ratio of these species varies in the shell number (or rather the age of the dust), and so the dust properties of any CWB are constantly evolving not only in production but in composition too.

Another promising avenue to study Wolf-Rayet stars through their spectra is in the method of spectropolarimetry. This method provides an unambiguous probe into the asphericity (or more generally anisotropy) of a stellar wind via any discrepant polarisation between continuum and line emission ([Harries et al., 2000](#); [Vink et al., 2011](#), see the latter for a succinct description of the method). This method has been successful in identifying wind asphericity and rapid rotation in several classes of stars, including WRs, and even in

the WC+O CWB WR 137 (Harries et al., 2000; Lefèvre et al., 2005). It is currently not unambiguously clear, though, if this method is valid as a signal of stellar rotation in the environment of a WCR.

Colliding wind binaries are strong X-ray sources, and were first hypothesised as such in Cherepashchuk (1976); Prilutskii & Usov (1976). Since the association of CWBs with X-ray sources, the theory modelling their properties has matured and accurately represents observations (Rauw & Nazé, 2016, for a review). Modern models reproduce X-ray spectra exceedingly well, providing insight into the mass loss rates and wind speed but also the homogeneity of the wind and its cooling physics (Zhekov, 2021; Zhekov et al., 2022). The X-ray flux of eccentric CWBs is variable as the properties at the WCR change over the course of the orbit, allowing us to constrain orbital and dust production properties; the phase of the flux peaks has been found to be wavelength dependent as the most efficient cooling mechanism at the WCR changes between radiative and adiabatic with orbital phase (Gosset & Nazé, 2016; Rauw & Nazé, 2016; Mackey et al., 2023). This kind of variation within the light curve is in conjunction with the usual eccentricity effects, as well as a WCR column density constraint on the orbital inclination in the X-ray (see Section 5.3 of Gosset & Nazé, 2016).

Colliding wind binaries are also luminous in the radio, observed as far back as 1976 (Sequist, 1976; De Becker & Raucq, 2013). The wind collision region in these systems acts as a particle accelerator, efficiently producing relativistic electrons that then emit radio waves via synchrotron radiation (Eichler & Usov, 1993; Bloot et al., 2022). As such, radio observations of CWBs offer information of the WCR directly, even so far as identifying the WCR itself with interferometric imaging (see Dougherty et al., 2005; Marcote et al., 2021). Since radio observations constrain the WCR so well, any discrepancies between wind models and data (e.g. momentum ratios, mass loss rates, etc.) are immediately apparent. Recently, radio observations of Apep were used to constrain its wind asphericity, where Bloot et al. (2022) found a preference for an anisotropic wind, with the WC star at an inclination angle of $(22 \pm 6)^\circ$ to the orbital plane. These studies are integral to our understanding of WRs as rapid rotators, as is to be expected from an aspherical wind, and their role as LGRB progenitors.

2.4.3 Direct Imaging

Although the dust nebulae produced by colliding wind binaries are orders of magnitude larger than the Solar System (see the scales in Figure 2.2), their Galactic distance of $\gtrsim 1\text{ kpc}$ requires that high angular resolution observations are needed to resolve structure. This, coupled with the fact that the resolved dust nebulae are luminous only in the infrared, means that direct imaging of these nebulae is a recent development coevolving with high angular resolution infrared astronomy. Directly imaging these nebulae is an essential effort as we can more precisely constrain many of the orbital parameters compared to other methods, and learn about some parameters that are not constrained by, or possible with, spectral or photometric analyses (see Section 2.4.5).

The first imaging of these systems was done with aperture mask interferometry on the Keck telescope for WR 104 and WR 98a (Tuthill et al., 1999; Monnier et al., 1999; Tuthill

et al., 2000). This method of imaging allowed for diffraction-limited (i.e. limited by the telescope optics rather than atmospheric distortion) observations which is essential to discern the nebula structure on the characteristic angular scale of these systems ($\lesssim 100$ mas). The 20 years since have seen an explosion of ground-based high angular resolution infrared astronomy, where direct images of colliding wind nebulae has become almost routine on large, 8 metre class telescopes (Marchenko et al., 2002; Marchenko & Moffat, 2007; Tuthill et al., 2008; Callingham et al., 2019, for WR 112, 48a, 104/98a, and Apep respectively), even for very distant systems near the galactic centre (Tuthill et al., 2006).

Very recently, the *James Webb Space Telescope* (JWST) has begun observing colliding wind binaries. JWST has made visible dust emission that would otherwise be difficult or impossible to obtain from ground-based facilities due to sensitivity and resolution limits imposed by the atmosphere. This has allowed observation of cool dust at a greater distance from the central CWB engine, and hence the simultaneous observation of several orbital periods' worth of dust shells in the nebulae (Lau et al., 2022). Not only does this allow us to determine the behaviour of dust over hundreds of years (its cooling curve and lifetime, for example), this allows us to break degeneracies in our models and very sensitively determine the orbital periods of these CWB systems.

2.4.4 Hydrodynamical Simulations

The most rigorous, if also computationally intensive, treatment of the colliding wind environment surrounding Wolf-Rayet binaries is with hydrodynamical simulations. Therein the complicated interactions of gas and dust in the environment around the binary can be simulated, offering insight into dust production and the chemical content of CWB nebulae. It is with these simulations that the dust production mechanism within CWBs was first quantified, showing that gas mixing in the turbulent shocked fluid can efficiently create dust amidst the harsh WR environment.

These simulations are essential in predicting the geometric dust production around the shock, as well as comparing the state of theory with observations. One of the most easily observed parameters of colliding wind nebulae, no matter the orientation, is the shock opening angle. The opening angle uniquely describes the momentum ratio between the two stellar winds in the binary, defined from stellar mass loss rates and wind terminal velocities as

$$\eta = \frac{\dot{M}_1 v_{\infty,1}}{\dot{M}_2 v_{\infty,2}} \quad (2.2)$$

for two stars of subscript 1 and 2. For a range of wind parameters, hydrodynamical simulations have accurately linked the wind momentum ratio and shock opening angle. Notably, hydrodynamical simulations were used to suggest that dust production is more efficient around the trailing edge of the shock than the leading edge (with respect to the orbital motion of the stars Lamberts et al., 2012; Hendrix et al., 2016; Soulain et al., 2023). This is observationally confirmed by the ‘azimuthal variation’ in dust production around the shock cone of WR 140 in particular (Williams et al., 2009; Han et al., 2022).

Hydrodynamical simulations have helped show just how sensitive dust production is to system parameters, explaining in large part the diversity of colliding wind nebulae. Not only

has mass loss rate, wind velocity, and wind chemical composition been shown to alter the shock properties (Eatson et al., 2022a; Soulain et al., 2023), but even the speed of orbital motion has been suggested as a key factor in the turn on vs turn off true anomaly in eccentric systems, such as WR 140 (Eatson et al., 2022b). Further, these simulations are consistently used in the reproduction of non-thermal (primarily X-ray and radio) observations (Pittard & Dougherty, 2006; Mackey et al., 2023).

2.4.5 A Geometric Model

In parallel with the maturation of hydrodynamical simulations, various simple geometric models were developed to reproduce key features of colliding wind nebulae. These geometric models allow for far simpler parameter estimation of CWBs and at much faster compute time compared with hydrodynamical simulations. Archimedean spirals have been used since the first direct images of these dust nebulae (Tuthill et al., 1999), although this does not account for the volumetric geometry of the dust plume and is valid only for a narrow range of binary orbital inclinations and eccentricities. Since then, a more physically motivated geometric model has been developed which reproduces the volumetric structure of the expanding plume. The model approximates the wind collision process by tracking rings of material that expand on the surface of a cone after encountering the nose of the wind-wind shock, expanding with a velocity corresponding to that of the radial wind (see Figure 3.1). When populating a high number of rings over the orbital period, the result is a discretised expanding plume structure that faithfully emulates the true geometry of the dust nebula when interpolated. This family of geometric models was first shown in Monnier et al. (2002) for WR 140, but has since been used for Apep (Callingham et al., 2019; Han et al., 2020), WR 104 (Harries et al., 2004), WR 112 (Lau et al., 2020b), WR 137 (Lau et al., 2024), and WR 140 (again, more accurately Han et al., 2022; Lau et al., 2022), with great success when compared to CWB imagery.

Somewhat similar, independent models have been published since the creation of the aforementioned geometric model. The first geometric treatment of the WCR alone was in Parkin & Pittard (2008), who modelled the shock region as a cone that rotated with orbital motion. This treatment of the geometric model involved implementing a ‘skew’ (a rotation of the WCR ring) to the WCR to account for the orbital motion of the secondary star. While this is apparently necessary to accurately model non-thermal emission from CWBs, it is not clear if this has a significant effect on dust production that would manifest in infrared imagery. An independent attempt at modelling the entire volumetric structure of the dust nebula was published in Williams et al. (2009) for WR 140, where the resulting eccentric structure is close to that of Monnier et al. (2002), but with added effects of dust asymmetry not unlike Han et al. (2022).

These simpler geometric models offer significant computational efficiency at a cost of physical insight. Where a hydrodynamical simulation may take hours, days, or more, the geometric model can be evaluated on the order of seconds. This opens the door for parameter estimation using the geometric model rather than using it purely as a consistency check. As mentioned earlier, this does come at a cost of physical insight; these geometric models do not offer detailed information about dust production (e.g. dust mass, non-thermal emission,

etc.), but they do offer immediate information on fundamental parameters such as orbital characteristics and dust turn on/off. As of yet, geometric models have not been used to constrain orbital parameters (eccentricity, inclination, etc.) effectively, and a proper statistical treatment with Bayesian parameter inference methods has not been proven in the literature. Han et al. (2020) described their attempt at using Markov Chain Monte Carlo (MCMC) to infer binary parameters from the ridges of the geometric dust plume (rather than the entire image as a whole). They ultimately abandoned attempts at machine optimisation with the model due to the high dimensionality of the problem together with difficulty in creating an appropriate loss function that accounts for the complex ridge geometry in the nebula images. With direct imaging of CWB nebulae now occurring so regularly, there is a gap in the literature in using modern statistical methods to infer system parameters with these images.



3

Creating a Fast and Differentiable Geometric Model

In Section 2.4.5 we described the previous use of a simple geometric model to reproduce the observed spiral structure of colliding wind nebulae. The basic idea that underpins the geometric model is to approximate instantaneous dust production within the wind collision region as a ring expanding from the stagnation point down the surface of the wind-wind shock cone. This ring is initialised in the orbital plane at the location of the ‘secondary’ star (in terms of wind strength, not mass as is convention), and ejected along the line of sight from the primary star to the secondary at the wind speed of the primary. As the two stars orbit each other, the direction of ring ejection changes with the result that the plume ‘wraps’ to create the characteristic spiral. This is illustrated in Figure 3.1.

Even at this basic level, the model has a multitude of parameters that can be changed at run time. The parameters most fundamental to this geometric approximation are the number of discretised points within each ring, and the number of rings to produce over the course of one orbital period. Ideally both of these would be as large as possible in order to reduce the error associated with approximating a continuous process as discrete (so-called quantisation error); practically we usually set these to be 400 points per ring and 1000 rings per orbit which provides a dense point cloud for the nebula.

To render the point cloud into an image that resembles the real nebulae, we take a histogram of the line of sight projection of the cloud. Even though these nebulae are three dimensional, in imaging we observe the column density of the dust due to its projection onto the plane of the sky. Hence by collapsing our modelled 3D point cloud to a 2D image we can reproduce the observed images. By utilising the weighting functionality of histograms, we can selectively alter the importance of selected points in order to emulate physical phenomena responsible for sculpting the nebula (e.g. dust turn off, azimuthal variation, etc.).

Previous geometric models have been successful in reproducing the structure of the spiral



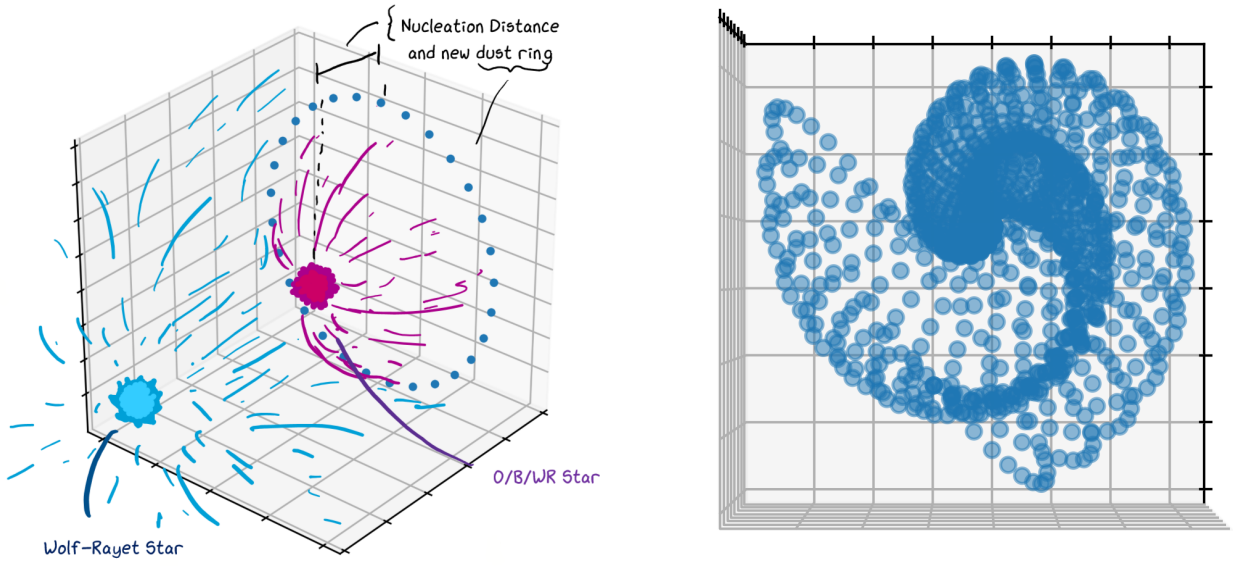


FIGURE 3.1: The idea behind the geometric model involves initialising rings at discrete times that trace the orbital motion of the binary stars. *Left:* As the Wolf-Rayet wind consistently overpowers that of its companion star, we initialise a ring of particles at some distance behind the companion. This ring is initialised with motion out of the system along the line of sight of the two stars, and with a speed of the WR terminal wind speed. *Right:* Dozens of rings are initialised at constant intervals throughout the orbital period, here for a representative test system with many fewer rings than N_{rings} so as to emphasise their presence. As rings age they expand and propagate further from the system barycenter. The orbital motion of the two stars then wraps the ring geometry into a characteristic spiral.

nebula, although they are computationally inefficient. If parameter inference is the goal of using these models, we need to make the model as computationally fast as possible so as to reduce compute time, both for interactive fitting and particularly to enable machine optimisation with an MCMC. Further, the high dimensionality of these problems requires that gradient-based, Hamiltonian Monte Carlo (HMC) methods be used so that the model can converge to a valid solution in finite time. Fortunately, the JAX Python framework ([Bradbury et al., 2018](#)) offers automatic differentiation capability for Python code and comes standard with Just In Time (JIT) compilation that speeds up model evaluation significantly. Therefore, creating a geometric model from scratch with JAX allows us to tackle all needed criteria at once. Indeed, our complete code takes of order $\lesssim 0.1$ seconds to generate the hundreds of thousands of particles in the point cloud and render them into an image, compared to that of ~ 5 s with an equivalent implementation in stock NumPy ([Harris et al., 2020](#)).

In Section 3.1, we describe the details of constructing this geometric model from scratch in JAX. In light of recent developments in colliding wind physics, we detail in Section 3.2 the additional, physically motivated features that we have added to the geometric model. In Section 3.5 we describe our development and success of the first colliding wind nebula light curve model. Finally, in Section 3.3 we describe the effort made to make the model differentiable end-to-end.

3.1 The Basic Ring Model

Before rings can be created, we first need a model of the binary orbit so that we know where to initialise the rings and in what direction they move. The motion of two celestial bodies in their mutual orbit is described by Kepler's equation ([Murray & Dermott, 1999](#), for a review of the two-body problem). To calculate the true anomaly of a star at any point over the orbital period (i.e. with known mean anomaly, M), Kepler's equation

$$M = E - e \sin E \quad (3.1)$$

must be solved for the eccentric anomaly, E . Traditionally, this is solved by an iterative method which converges to the correct value of E given M . Those iterative methods are not differentiable, however, and so we use the non-iterative method described in [Markley \(1995\)](#) and implemented in JAX in [Hattori et al. \(2024\)](#). From the eccentric anomaly, we can then calculate the true anomaly, ν , analytically via

$$\nu = 2 \operatorname{atan2} \left(\sqrt{1+e} \sin(E/2), \sqrt{1-e} \cos(E/2) \right) \quad (3.2)$$

Since the mean anomaly changes linearly with time, this calculation of true anomaly provides the angular position of each body relative to the focus of their orbits (i.e. the centre of mass) at constant time intervals.

The choice of mean anomaly grid is directly proportional to the time domain over which dust is produced. If the system in question produces dust constantly, a grid choice encompassing $0 \leq M \leq 2\pi$ then results in the relevant true anomalies with which to initialise rings. If the system is an episodic dust producer, i.e. produces dust between a well-defined dust ‘turn on’ and ‘turn off’, the choice of a mean anomaly grid is not so straightforward. Previous implementations of the geometric model would initialise rings over a full circle of mean anomaly but then discard rings whose true anomaly fall out of the specified turn on/off range. As producing ‘invisible’ rings requires significant computational work – of order the same compute time as the visible rings and to no effect – we should avoid this and devise a method to produce only rings that contribute to the visible spiral plume.

To produce rings only between dust turn on/off, we need to find a grid of mean anomalies between our true anomaly bounds; essentially the inverse problem to that described above. We begin with our true anomaly bounds, $\nu_{t,\text{on}}$ and $\nu_{t,\text{off}}$. For true anomaly we follow the convention that periastron corresponds to $\nu = 0$ and so we expect that the turn on is in the range $-\pi \leq \nu_{t,\text{on}} \leq 0$ radians, conversely $0 \leq \nu_{t,\text{off}} \leq \pi$ radians for turn off anomaly. The eccentric anomaly corresponding to dust turn on is then calculated as

$$E_{t,\text{on}} = 2 \operatorname{atan2} \left(\tan \left(\frac{\nu_{t,\text{on}}}{2} \right), \sqrt{\frac{1+e}{1-e}} \right) \quad (3.3)$$

and the same is used to calculate $E_{t,\text{off}}$ instead with $\nu_{t,\text{off}}$. The results of this can be substituted into Equation 3.1 to then obtain the mean anomaly bounds corresponding to dust turn on/off, $M_{t,\text{on/off}}$. For the episodic dust producers, we create a grid of mean anomalies in the range $M_{t,\text{on}} \leq M \leq M_{t,\text{off}}$ for each single shell which is fed back into the solver to find the true anomalies corresponding to the stellar orbits.



In order to eventually determine the size and distance of each ring from the binary centre, the age of each ring must be calculated. An equally spaced grid within the mean anomaly bounds naturally provides an equally spaced grid in time. The age of the ring corresponding to each mean anomaly value, relative to the orbital period (i.e. in the range $0 \leq t_{\text{age}} \leq 1$), can then be calculated by

$$t_{\text{age}} = \text{mod} \left(\frac{\text{mod}(M, 2\pi)}{2\pi} - \phi, 1 \right) \quad (3.4)$$

where ϕ is the current orbital phase of the binary. Equation 3.4 results in rings created at the current orbital phase having the lowest age, and those at the previous mean anomaly grid position having the largest age. When multiple shells of material are being simulated, the grids of mean anomalies and ages are tiled N_{shell} times, where each successive tiling has an additional +1 to the age which accounts for the previous orbital periods of time. To convert from this nondimensionalised age relative to the orbital period into an absolute time, we can simply multiply by P_{orb} .

Using the true anomalies corresponding to dust production, the positions of the stars in their orbits can be calculated so that the positions and orientation of each ring can be found. The nondimensionalised position of the primary star is calculated as

$$\hat{\mathbf{r}}_1 = (\cos(\nu), \sin(\nu), 0) \quad (3.5)$$

for each true anomaly value, where we note that we take the orbital motion to be in the $x - y$ plane; the corresponding position of the secondary is just the negative of Equation 3.5, $\hat{\mathbf{r}}_2 = -\hat{\mathbf{r}}_1$, since angular displacement of the stars is always π radians relative to the system barycenter. To convert this into a true distance, we multiply by the distance of each star relative to the system barycenter, $\vec{r}_{1/2} = r_{1/2} \hat{\mathbf{r}}_{1/2}$, where

$$r_{1/2} = a_{1/2}(1 - e \cos(E)) \quad (3.6)$$

for each corresponding eccentric anomaly to the true anomaly, and for each star. From Kepler's Third Law, the semi-major axis of the binary system is

$$a = \left(\frac{G(M_1 + M_2)P_{\text{orb}}^2}{4\pi^2} \right)^{1/3} \quad (3.7)$$

and so the semi-major axis of each star in their orbits relative to the system barycenter is

$$a_1 = a \frac{M_2}{M_1 + M_2}; \quad a_2 = a \frac{M_1}{M_1 + M_2} \quad (3.8)$$

Calculating the absolute positions of the stars, especially relative to each other, is necessary when determining the position and angle of each ring relative to the system.

We construct the rings along the x -axis (so that a circle is seen in the $y - z$ plane), and populate them with $N_{\text{particles}}$ particles per ring. The particles are linearly spaced within the ring and constitute a full circle, such that $0 \leq \theta_{\text{particle}} \leq 2\pi$. The coordinates of the particles within each ring depends on the plume opening angle, θ_{OA} , by

$$\hat{\mathbf{r}}_{\text{particle}} = \left(\cos\left(\frac{\theta_{\text{OA}}}{2}\right), \sin\left(\frac{\theta_{\text{OA}}}{2}\right) \sin(\theta_{\text{particle}}), \sin\left(\frac{\theta_{\text{OA}}}{2}\right) \cos(\theta_{\text{particle}}) \right) \quad (3.9)$$

The particle coordinates within each ring are then scaled by the distance they should have travelled given the ring age and the WR wind speed,

$$\vec{r}_{\text{particle}} = v_{\text{wind}} t_{\text{age}} \hat{\mathbf{r}}_{\text{particle}} \quad (3.10)$$

This expands the ring along the surface of a cone projecting outwards from the system centre, and both enlarges the ring and displaces it by the appropriate amounts. The direction that this cone is facing is calculated from the current stellar positions as

$$\varphi = \text{atan}2\left(\frac{y_2 - y_1}{\|\vec{r}_1 - \vec{r}_2\|}, \frac{x_2 - x_1}{\|\vec{r}_1 - \vec{r}_2\|}\right) \quad (3.11)$$

which is the angle from the primary to secondary star in the orbital plane. Since the rings are created along the x -axis, they must be rotated about the z -axis by φ so that they align with the direction vector of the primary to the secondary. That is, we update each particle vector to be

$$\vec{r}_{\text{particle}} = (R_z(\varphi) \vec{r}_{\text{particle}}^T)^T = \left(\begin{bmatrix} \cos(\varphi) & -\sin(\varphi) & 0 \\ \sin(\varphi) & \cos(\varphi) & 0 \\ 0 & 0 & 1 \end{bmatrix} \begin{bmatrix} x_{\text{particle}} \\ y_{\text{particle}} \\ z_{\text{particle}} \end{bmatrix} \right)^T \quad (3.12)$$

While Equations 3.9–3.12 are described in terms of a single particle, these operations are applied to all of the particles that belong to a single ring at once. This procedure is made computationally efficient by the `vmap` functionality within JAX, which automatically vectorises the particle and ring mathematics. This entire process of generating rings to populate the point cloud is shown in Figure 3.1 for a system of arbitrarily chosen parameters.

In our simulations we create each ring with $N_{\text{particles}} = 500$ particles and each shell with $N_{\text{rings}} = 1000$ rings. These numbers were chosen as a suitable middle ground between computational performance (which would favour fewer rings and particles) and dense spatial sampling of the plume (which would require as many rings and particles as possible). Since the true colliding wind nebulae are smooth to first order, our approximation of a point cloud introduces quantisation error into any rendered image. Hence, our choice of $N_{\text{particles}}$ and N_{rings} was motivated so that there would always be a small but non-zero number of particles in even the lowest density rendered pixels.

With our point cloud generated, next we need to render an image of the simulated nebula so as to compare it to observations. For this, we collapse our 3D point cloud into two dimensions which is analogous to its projection in the plane of the sky. We then take a 2D histogram of these collapsed particle locations which produces a ‘heatmap’ of the nebula as shown in Figure 3.2. Although this is a simple procedure, producing a column density of particles in this way is essentially what we observe when taking real astronomical images of optically thin material: the line of sight projection of material in the field of view. As a by-product, using a histogram allows us to very easily change the number of bins in the render as a proxy of changing the angular resolution of the simulation. This proves useful when comparing a simulated image to that taken by a telescope; we can render the image with the exact number of pixels (bins) needed on the correct angular pixel scale by manually fixing just two parameters.



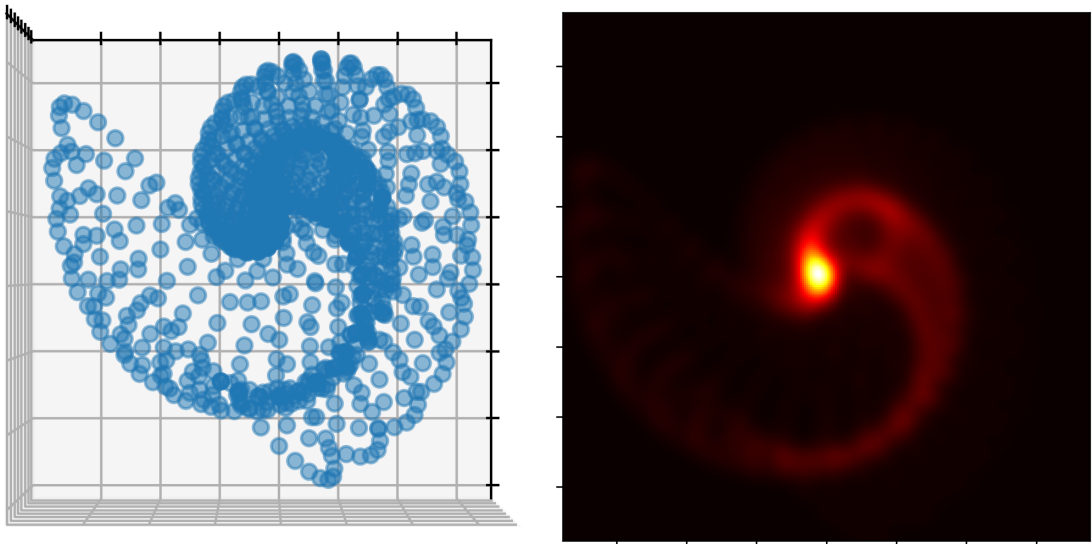


FIGURE 3.2: By collapsing the created point cloud (left) into its projection on the sky via a 2D histogram, we produce a column density map of particles (right) that resembles true images of colliding wind nebulae.

Since the image is rendered in two dimensions, we must first ensure that the plume geometry is consistent with the orbital elements prior to rendering. That is, we must rotate the entire point cloud in 3D with the appropriate Euler angles so that the point cloud resembles the true geometry from our (observer’s) perspective. We update the coordinates of each particle within the point cloud, $\vec{r}_{\text{particle}}$, as

$$\vec{r}_{\text{particle}} = (R_z(-\Omega)R_x(-i)R_z(-\omega)\vec{r}_{\text{particle}}^T)^T \quad (3.13)$$

where Ω is the binary orbit longitude of ascending node, i the inclination, and ω the argument of periastron. Note that these parameters do not affect the intrinsic geometry of the nebula, but only its projection into the plane of the sky.

3.2 Higher Order Effects

In the previous Section we described in detail the process of generating a point cloud and rendering it into an image for a general colliding wind binary system. The focus of that Section was to share the underlying mathematics and process which is the foundation of modelling any particular system. As Figure 2.2 and Section 2.4.1 show, however, no two WR CWB systems are exactly alike and many additional features are needed in our geometric model to faithfully recreate their observed morphology.

In this Section we describe the so-called ‘higher order’ effects that we incorporate into the geometric model. Most of these features are physically motivated from observations and hydrodynamical simulations, while in Section 3.2.4 we discuss changes to the model purely to emulate real images (i.e. non-physically-motivated effects).

3.2.1 Azimuthal and Orbital Variation in Dust Production

The first additional feature to the model that we consider is the azimuthal variation in dust production on each created ring. WR 140 was observed to create dust most strongly on the trailing edge (with respect to the orbital motion) of its shock cone in [Williams et al. \(2009\)](#). In the time since, this phenomenon has been required to reproduce the observed geometry of WR 140 in multi-epoch imaging including with JWST ([Han et al., 2022](#); [Lau et al., 2022](#)). This enhanced dust production along the trailing edge of the shock has also been supported by hydrodynamical simulation of WR 104 ([Soulain et al., 2023](#)).

Since we render each point cloud into an image via a histogram, we can apply weightings to each particle which affects how much it contributes to the final geometry. Utilising this functionality, we model this azimuthal variation as a Gaussian function multiplier applied to each particle within a ring and each entire ring respectively, similarly to [Han et al. \(2022\)](#). That is, the weighting factor of each particle from azimuthal variation is calculated by

$$\delta w_{\text{az}} = \max \left\{ 1 - (1 - A_{\text{az}}) \exp \left(-\frac{(\theta_{\text{particle}} - \theta_{\text{az_min}})^2}{2\sigma_{\text{az}}^2} \right), 0 \right\} \quad (3.14)$$

where A_{az} is the global strength of the variation, θ_{particle} is the angular coordinate of the particle within the ring (0° being in the $+z$ direction), $\theta_{\text{az_min}}$ is the location of the azimuthal minimum and σ_{az} is the spread of the variation across the angular coordinates of the particles. Although each of these are free parameters, we usually set $\theta_{\text{az_min}} = 90^\circ$ in practice; this corresponds to the leading edge of the dust plume with respect to the orbital motion resulting in dust production being weaker at the leading edge. A minimum value of 0 in Equation 3.14 is enforced since A_{az} can in principle take any positive value, although it is usually in the range $0 \lesssim A_{\text{az}} \leq 1$. This multiplicative factor calculated for all of the particles within the ring, and we approximate this effect as being constant across orbital phases.

The dust nebula of WR 140 shows evidence not only of azimuthal asymmetry, but orbital modulation in dust production between the classical turn on and off ([Williams et al., 2009](#); [Han et al., 2022](#)). This manifests as a dip in the dust production when the binary stars are near periastron which results in two distinct phases of dust nucleation per orbit: at ingress and egress. We model this orbital modulation much in the same way as for the azimuthal variation,

$$\delta w_{\text{orb}} = \max \left\{ 1 - (1 - A_{\text{orb}}) \exp \left(-\frac{(\nu_{\text{ring}} - \nu_{\text{orb_min}})^2}{2\sigma_{\text{orb}}^2} \right), 0 \right\} \quad (3.15)$$

which is applied to an entire ring's weighting. The parameters in this Gaussian are analogous to that of the azimuthal variation, instead using the true anomaly of the entire ring instead of a particle angular coordinate, and with orbital variation amplitudes and spreads instead of azimuthal. Although technically free, we set $\nu_{\text{orb_min}} = 180^\circ$, corresponding to the periastron of the orbit where the dust production may be weak during the dust production phase.

For those systems that do not show signs of azimuthal and/or orbital variation, we may simply set $A_{\text{az}} = A_{\text{orb}} = 1$ in Equations 3.14 and 3.15, thereby setting the weighting effect to 0. We show in Figure 3.3 these weighting values given the particle angle or ring true anomaly for multiple values of A and σ .

When the true anomaly at the current orbital position falls between that of the turn on and off threshold values, the produced rings contribute to the visible dust plume. We



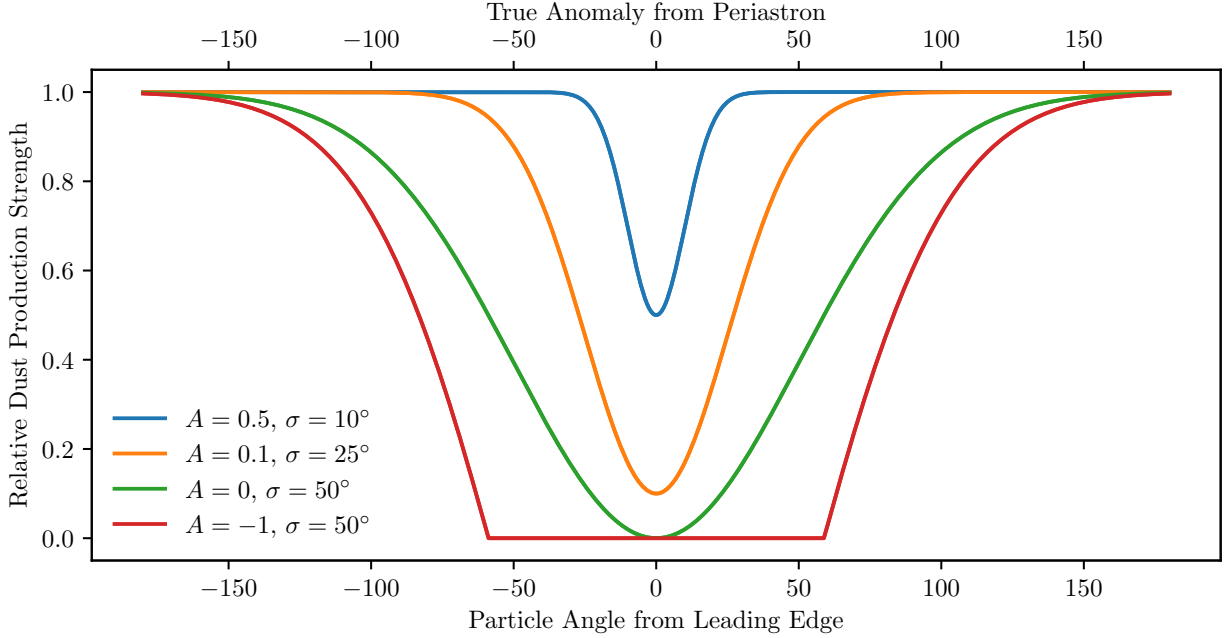


FIGURE 3.3: The free parameters of Equations 3.14 and 3.15 change the depth and breadth of the strength variations in dust production. The top axis represents the weighting applied to each ring as a function of true anomaly for a representative set of free parameters, while the bottom axis represents the weighting applied to each particle within each single ring.

should not expect, however, that the turn on or off of dust production is instantaneous, but rather that there is a gradual change in the production rate. Hence as an additional feature, we have implemented a turn on/off smoothing in the dust production that was not present in previous versions of the geometric model. To do this, we use a half-Gaussian function to decrease the weight of rings that are outside of the usual dust production regime; this function has a value of 1 at the usual dust production true anomaly bounds, and decreases with standard deviation σ_{gradual} outside of the usual dust production regime. To include this we therefore have to inject some rings outside of the usual dust production true anomaly bounds, $\nu_{t,\text{on/off}}$. We modify the previous bounds to now be

$$\nu_{t,\text{on}} = \max \{-180^\circ, \nu_{t,\text{on}} - 2\sigma_{\text{gradual}}\}; \quad \nu_{t,\text{off}} = \min \{180^\circ, \nu_{t,\text{off}} + 2\sigma_{\text{gradual}}\} \quad (3.16)$$

where we include rings up to two standard deviations outside of the usual bounds. For each ring, we then apply a histogram weighting of

$$\delta w_{\text{gradual}} = \begin{cases} \exp \left(\frac{(\nu_{\text{ring}} - \nu_{t,\text{on}})^2}{2\sigma_{\text{gradual}}^2} \right) & \nu_{\text{ring}} < \nu_{t,\text{on}} \\ 1 & \nu_{t,\text{on}} \leq \nu_{\text{ring}} \leq \nu_{t,\text{off}} \\ \exp \left(\frac{(\nu_{\text{ring}} - \nu_{t,\text{off}})^2}{2\sigma_{\text{gradual}}^2} \right) & \nu_{t,\text{off}} < \nu_{\text{ring}} \end{cases} \quad (3.17)$$

to emulate a gradual dust production turn on and off. With this as the final required weighting factor, the overall weighting on each particle in the point cloud is calculated as

$$w = \delta w_{\text{az}} \times \delta w_{\text{orb}} \times \delta w_{\text{gradual}} \quad (3.18)$$

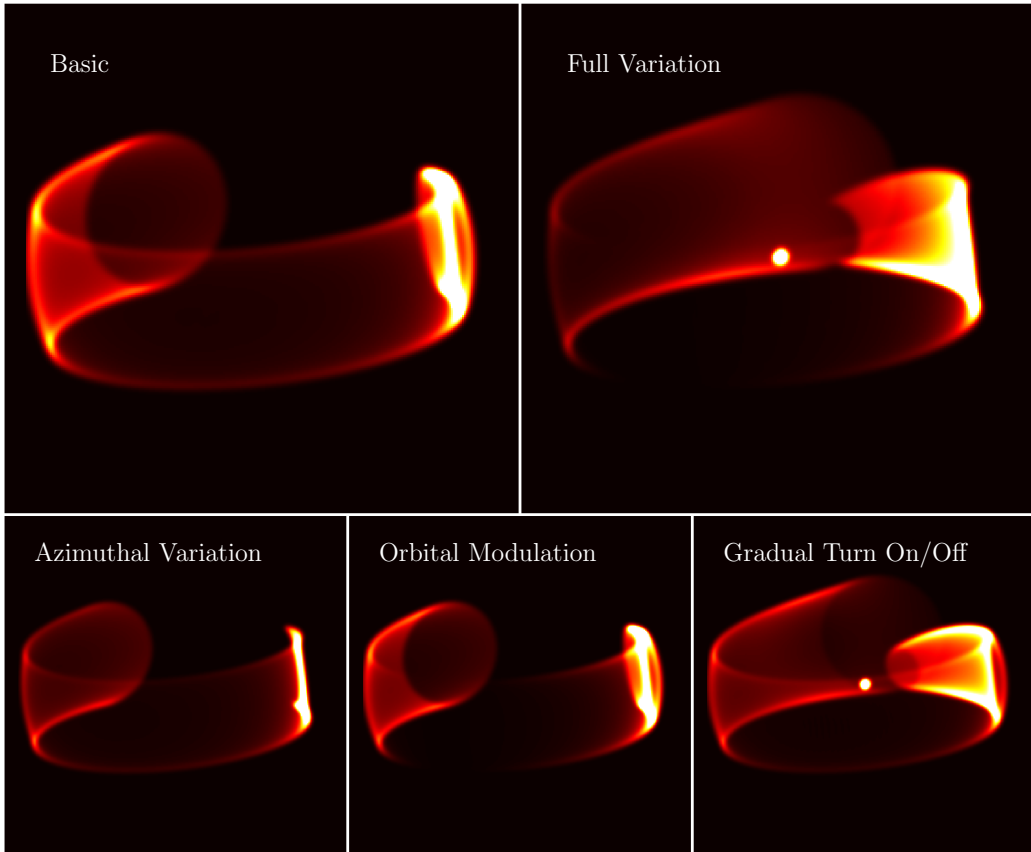


FIGURE 3.4: Each higher order variation affects the dust plume in different ways. The top right plot shows how an arbitrary test system appears with only the ‘basic’ model implementation as described in Section 3.1. The bottom row shows each of the higher order dust production variations discussed so far, and their effect on the ‘basic’ plume in isolation. The top right plot shows the effect of including all of these features at once. The value of each effect in the figure is: $\sigma_{az} = 60^\circ$; $A_{az} = -1$; $\sigma_{orb} = 40^\circ$; $A_{orb} = 0$; $\sigma_{gradual} = 19^\circ$.

For the Apep system in particular, we make more modifications to the total weighting of each particle which we discuss in Section 5.2.

3.2.2 Acceleration in the Dust Shell

Wolf-Rayet stars are among the most luminous stellar objects, and so the environment immediately surrounding them is engulfed in intense radiation. As a result, we expect that the formed dust grains would experience some manner of radiation pressure given that WR stars are at a significant fraction of their Eddington luminosity (Gräfener et al., 2011; Maeder et al., 2012). This radiation pressure has been observed accelerating gas around clusters of stars (Murray et al., 2011), and has been used to explain the apparent acceleration of dust shells around WR 140 (Han et al., 2022).

In the paper describing the radiative acceleration of dust around WR 140, the authors do not explicitly include acceleration into their geometric model. For the first time, we



include this acceleration in our model. [Han et al. \(2022\)](#) propose an acceleration model that is largely physically motivated: the dust nucleates at some distance from the star in an optically thick regime while accelerating at a constant rate, then becomes optically thin some time later and proceeds to accelerate at a decreasing rate. The strength of acceleration in this model is parameterised by radial distance from the central WR+O binary, as one would expect from radiation pressure which follows an inverse-square law. Unfortunately elements of this prescription are difficult to integrate into our geometric model; the ejected rings are parameterised mainly by their age, which is subsequently used to calculate their (non-accelerated) radial distance. In order to incorporate the acceleration terms from [Han et al.](#) into our geometric model, an iterative method would be required to find the correct accelerated distance. This introduces computational complexity and is at odds with gradient computation in JAX.

To maximise computational efficiency and maintain gradient calculations, we instead use a more phenomenological model for acceleration parameterised by the dust ring age: the velocity of each ring is the exponential decay of some initial velocity v_i to a terminal velocity v_∞ in the radial direction from the central WR binary. That is,

$$v(t_{\text{age}}) = v_\infty + (v_i - v_\infty) \exp(-10^A t_{\text{age}}) \quad (3.19)$$

where A is a scaling constant which determines the slope of the exponential (i.e. the strength of the acceleration). When v is in units of km s^{-1} and t_{age} in units of years, we find this exponential constant should be roughly in the range 10^{-5} to 10^0 years^{-1} , or $-5 \lesssim A \lesssim 0$.

Including this acceleration into the model means that we replace the v_{wind} parameter in Equation 3.10 so that the Equation now reads

$$\vec{r}_{\text{particle}} = v(t_{\text{age}}) t_{\text{age}} \hat{\mathbf{r}}_{\text{particle}} \quad (3.20)$$

In modelling acceleration this way, we note that we can also easily simulate dust deceleration as needed. In Equation 3.19 we see that when $v_\infty < v_i$, the rings are decelerating towards a terminal velocity; conversely, $v_\infty > v_i$ results in dust ring acceleration as we would model in WR 140, for example. The detailed consequences of modelling acceleration with an exponential instead of a power law have not been exhaustively explored. However the acceleration term is dominant only at early orbital phases when the dust is close to the luminous stars. At present there does not exist a large body of observations of the CWB systems at these phases, making comparison difficult. Since [Han et al.](#) and our implementation of acceleration both yield velocity converging to a terminal value, we expect that any difference in geometric fits would be small and not the dominant source of model error.

3.2.3 Modelling Wind Anisotropy

One of the biggest unanswered questions about the Wolf-Rayet colliding wind binaries is whether their spiral nebulae can exhibit evidence of wind anisotropy, particularly in the case of the Apep system ([Callingham et al., 2019](#)). The dominant wind in the Apep system has been suggested as being anisotropic on account of the large discrepancy between the polar wind speed (measured through spectroscopy) and the nebula expansion speed (measured kinematically, also see Section 5.1); the idea here is that WC star in Apep may harbour a



FIGURE 3.5: Wind anisotropies may be visible in the dust plume if the wind-dominant star is inclined with respect to the orbital plane (left). In principle, the axis of rotation could also be misaligned from the periapsis of orbit (right) which might affect the wind anisotropy evidence in elliptical orbits.

slow, but dense equatorial wind which is responsible for the visible dust plume as well as a fast and sparse polar wind. This interpretation suggests that this star is critically rotating, in which case Apel is the most likely LGRB progenitor candidate known in our Galaxy. It is therefore essential to look for any evidence of wind anisotropy in the visible plume to investigate this hypothesis.

We present here the first attempt at integrating an anisotropic wind into the geometric model for the Wolf-Rayet CWBs. Evidence of anisotropy in the dust plume may be present if the star with the higher momentum wind is inclined with respect to the orbital plane of the binary; this would mean that the wind at the shock interface would change in momentum depending on the orbital position of the stars. The inclination of this star may also be misaligned with the orbit argument of periastron, ϖ , which would affect the anisotropy-true anomaly correlation. These ideas are shown in Figure 3.5.

We parameterise the strength of wind anisotropy based on the origin latitude of the wind that is currently causing the colliding wind shock, ϑ . We take $\vartheta = 0$ as being along the equator of the windy star, and so the value of ϑ at any point along the orbit is calculated as

$$\vartheta(\nu) = |\iota \sin(\nu - \varpi)| \quad (3.21)$$

where ι is the inclination of the star with respect to the orbital plane, and ϖ is the argument of periastron offset, and the absolute value assumes that the wind anisotropy is symmetric about the equator.

We expect that a wind anisotropy would manifest itself as a true anomaly dependence on the plume opening angle and/or expansion velocity in the CWB nebula. This is because if the mass-loss or speed is latitude-dependent, the momentum ratio of the winds at the shock interface would change depending on the wind origin and hence the plume geometry should change as a result. We considered implementing a model in which the rings were elliptical (as opposed to circular), but the WCR is always such a distance from the two stars that the local wind field is essentially planar.

Without detailed knowledge of the exact 3D wind fields around these WC/WN stars, we phenomenologically model these opening angle and expansion velocity perturbations due to anisotropy as multipliers onto the standard parameters, much in the same way we modelled



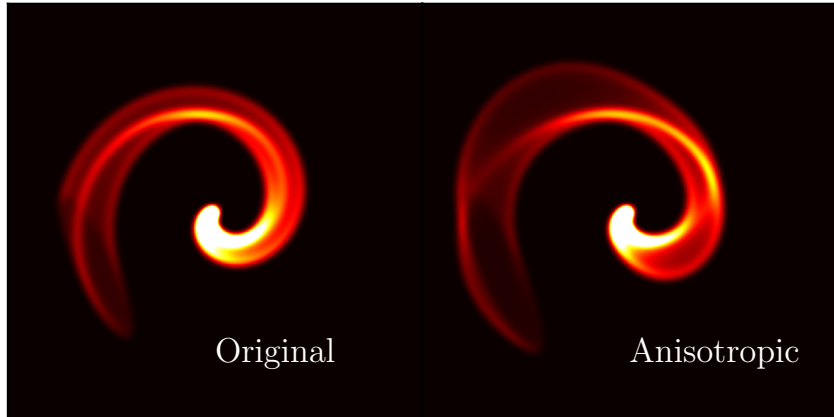


FIGURE 3.6: The introduction of anisotropy into the geometric model typically results in lobes protruding from the original plume. The system in this figure has a modest $\iota = 24^\circ$ with opening angle and velocity parameters chosen arbitrarily for visualisation.

azimuthal and orbital variations as histogram weighting multipliers. These multipliers are

$$\delta v(\vartheta) = 1 + \left(\frac{v_{\text{polar}}}{v(t_{\text{age}})} - 1 \right) \tanh(10^{m_v} \vartheta^{p_v}) \quad (3.22)$$

$$\delta \theta_{\text{OA}}(\vartheta) = 1 + \left(\frac{\theta_{\text{OA, polar}}}{\theta_{\text{OA}}} - 1 \right) \tanh(10^{m_{\text{OA}}} \vartheta^{p_{\text{OA}}}) \quad (3.23)$$

where we have three additional parameters for each of the velocity and opening angle multipliers: the parameter of subscript ‘polar’ denotes the value of that parameter due to the polar wind, the m_v and m_{OA} represent the value of a constant multiplier onto the latitude dependence of the wind, and p_v/p_{OA} impose a power law dependence of the anisotropy strength onto the latitude. The tanh function was used here as this allows us to sensitively change the slope and shape of the multiplier dependence on ϕ . As a caveat, this manifests only as a monotonically changing multiplier value and cannot represent a latitude dependence with turning points. This nonmonotonic behaviour has been seen in some numerical models of massive stellar winds (Hastings et al., 2023), although it is common to assume smoothly changing monotonic wind parameters vs latitude for evolved massive stars (van Marle et al., 2008). The true WR wind morphology, including the effects of rotation, would require detailed stellar evolution and magnetohydrodynamical models, and this does not appear to have been published in the literature (although this has been recently done for non-rotating WR stars in Moens et al., 2022).

3.2.4 Miscellaneous Features and Details

There exist a number of features we have implemented into the geometric model that have either little or no effect on the physical geometry. In the aim of doing statistical inference with our model, we have added in two parameters that affect only the pixel values of the final render; the first is a brightness ceiling on the rendered array as an emulation for image

pixel saturation, and the second is a power law scaling of the remaining pixels mainly to exaggerate otherwise dim pixels. Allowing for these parameters to change makes it easier to compare simulated images to real data, and may allow for faster convergence in statistical methods on our simulations.

The next modification made to the geometric model pertains to the azimuthal angles of particles within each generated ring. Equation 3.9 describes the initial Cartesian coordinates of particles within each ring, parameterised by some azimuthal angle θ_{particle} unique to each particle within the ring. In early versions of our model, the grid of these azimuthal angles for particles within each ring was identical across all of the rings in the plume; what we saw was that this accentuated the quantisation error of approximating these continuous rings as a series of particles. Since the particles were at identical angular positions within neighbouring rings, ‘stripes’ of nebulosity would be visible in the final image. One solution to this would be to simply increase the number of particles in each ring, although this would quickly increase compute time. To minimise this effect, we instead shift the angular coordinate of all particles within a ring by 1 radian across each consecutive ring created. This imposes some quasi-randomness in the position of the particles across neighbouring rings, especially since the angular coordinates are mod 2π .

Since we calculate the position of each star at all times in the model, it is relatively straightforward to take this position and plot the stars on the final rendered image. To do this, we generate the simulated image of the colliding wind nebula, then inject Gaussian flux profiles on the angular positions of the stars at that epoch. The user can determine the amplitude of the flux (how bright the star is), as well as the standard deviation of the flux profile (how much the flux bleeds into neighbouring pixels). Including the stars in each image helps to anchor the geometry of the plume with respect to its origin, and the position of stars becomes particularly important in our discussion in Section 5.2.

The final small addition to the geometric model that we describe is the dust nucleation distance. Dust is expected to nucleate at some distance, r_{nuc} , behind the colliding wind shock (referred to as ‘dust-forming separation’ in Eatson et al., 2022a, for example) where the conditions are favourable. This nucleation distance is estimated to be typically on the order of tens of au for the WR CWBs, sufficiently far downstream for both mixing of the two winds and attenuation of the stars’ ionising radiation. Because this nucleation distance is relatively small, the gaps in the models due to dust not yet nucleated are limited to phases close to periastron for the episodic dust producers. To account for this nucleation distance in the model, we include another ring weighting multiplier in the form of a heaviside step function

$$\delta w_{\text{nuc}} = \begin{cases} 1 & \|\vec{r}_{\text{particle}}\| \geq r_{\text{nuc}} \\ 0 & \text{otherwise} \end{cases} \quad (3.24)$$

which is then included onto Equation 3.18. Including this feature mainly results in a delay in dust production from the orbital motion of the stars, and has no impact on dust shells that are not actively forming dust. The strongest evidence for delayed onset of dust formation, apart from in hydrodynamical simulations, comes from CWB light curves where phase shifts between orbital data and infrared peaks are apparent (see Section 3.5).



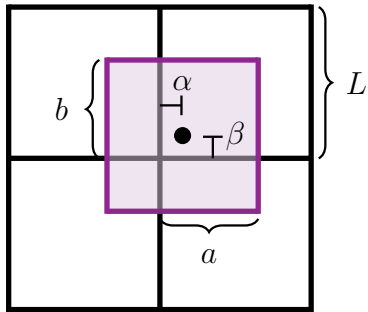


FIGURE 3.7: The fundamental behaviour of our smooth histogram involves spreading out point information over multiple bins. We show here a graphical representation of each parameter used in Equations 3.25–3.30. We note that the purple box, like the histogram bins, has a side length L .

3.3 A Fully Differentiable Geometric Model

The main advantage to building our geometric model within the JAX framework is to utilise its powerful automatic differentiation capabilities. When deployed for statistical inference, this allows us to calculate the gradient of a log-likelihood function with respect to any of the model parameters. Great care has been taken to ensure that the geometric model is smoothly differentiable with respect to every parameter. Regardless, there are steps in the pipeline that are not natively differentiable and so alternatives are needed.

In the context of differentiation, the most glaring issue in our original model lies in the rendering step: after generating the three dimensional point cloud, we take a histogram of the points to generate an image. Histograms are, however, not smoothly differentiable due to their inherently discrete representation of data. For example, a point in one dimension may be in the centre of a histogram bin, or it may be on the extreme edge of the bin, and the bin count increases by one all the same. One can imagine moving this point smoothly in one dimension (e.g. from the centre of a bin to the edge of the same bin) and even though the absolute coordinate of the point has changed, the bin count remains steady. Suddenly, as the point moves from the edge of one bin to another, there is a discontinuous drop in the count of the first bin and conversely a discontinuous increase in the count of the neighbour. Discontinuities are problematic for gradients, and so a gradient-friendly renderer is needed.

Our devised solution still acts fundamentally as a histogramming tool, but spreads density information of each point to all of the neighbouring bins of a point. We show the simple setup in Figure 3.7, where instead of discrete counts added onto a bin total we calculate areas. The ‘count’ incremented to each neighbouring bin of a point is chosen based on the area overlap of a square (with side length of the bin size) centred on the point exactly. The bin that the point occupies will have the most area overlap of this square and so will have the highest ‘count’. If a point is to the left of centre of a bin, the neighbouring left bin will have some lesser ‘count’ increment, and analogously for the top, down, and right directions.

The equations to calculate the contribution to each bin are made easier with a change of coordinates. If a point at position (x, y) is α away from the left edge of its resident bin and β away from the bottom edge of its bin (i.e. $\alpha = x \bmod L$ and $\beta = y \bmod L$ for L bin side

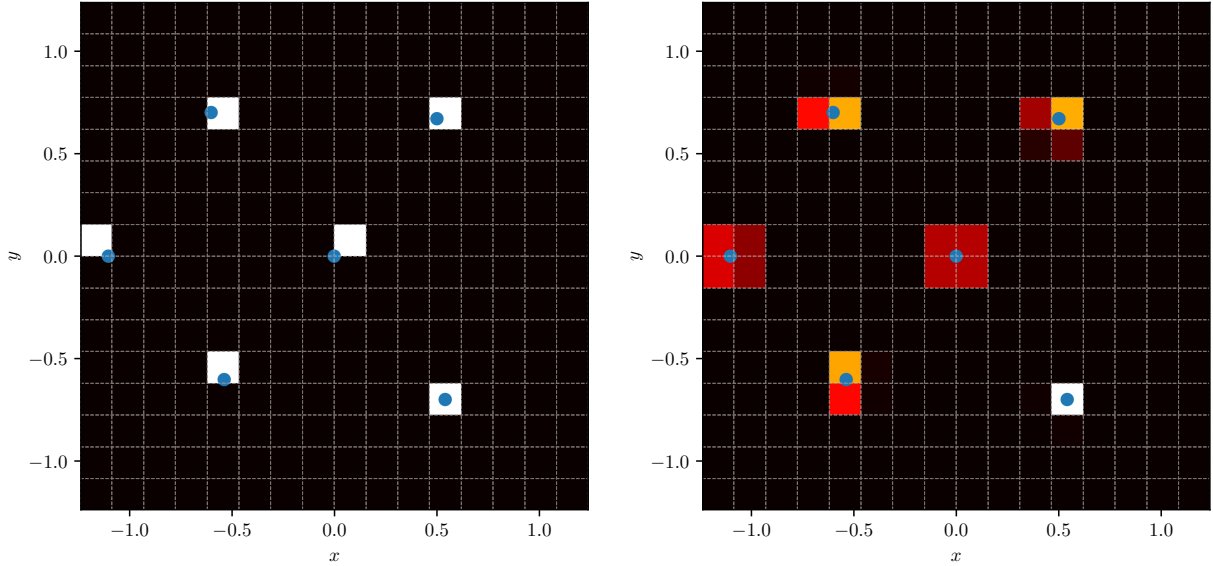


FIGURE 3.8: We show the behaviour of the smooth histogram at all key criteria. The true positions of points are shown as a blue dot, and the associated smooth histogram representation is shown in the bins (here with a grid size of $N = 16$). Dot positions were manually chosen so that all behaviours are shown in the same plot. Brighter values of the colourmap represent larger bin values. An animation showing how the normal and smooth histogram compare for a moving particle is available online [Q](#).

length), we can define new coordinates

$$a = \min\{\alpha, L - \alpha\} + L/2 \quad (3.25)$$

$$b = \min\{\beta, L - \beta\} + L/2 \quad (3.26)$$

where the $+L/2$ for each dimension arises from the fact that the overlapping square is centred on the point absolute coordinate. The geometric interpretation of these parameters is shown in Figure 3.7. With these, the respective contribution to the main (that the point lies in), horizontal neighbouring, vertical neighbouring, and diagonal neighbouring bins are

$$A_{\text{main}} = ab \quad (3.27)$$

$$A_{\text{horiz}} = (L - a)b \quad (3.28)$$

$$A_{\text{vert}} = a(L - b) \quad (3.29)$$

$$A_{\text{diag}} = (L - a)(L - b) \quad (3.30)$$

We show in Figure 3.8 how this smooth histogramming differs from a traditional histogram for a range of possible point positions within bins. In particular we see that that when a point is directly in the centre of a bin, this method reduces to the normal histogramming behaviour where only one bin count is changed. If a point is directly centred on one axis (vertical or horizontal) within a bin, only the other axis gets a count contribution spread to neighbouring bins. When a point is directly on the corner of a bin, all neighbouring bins get the same count contribution. This method enforces finite gradients as a point moves



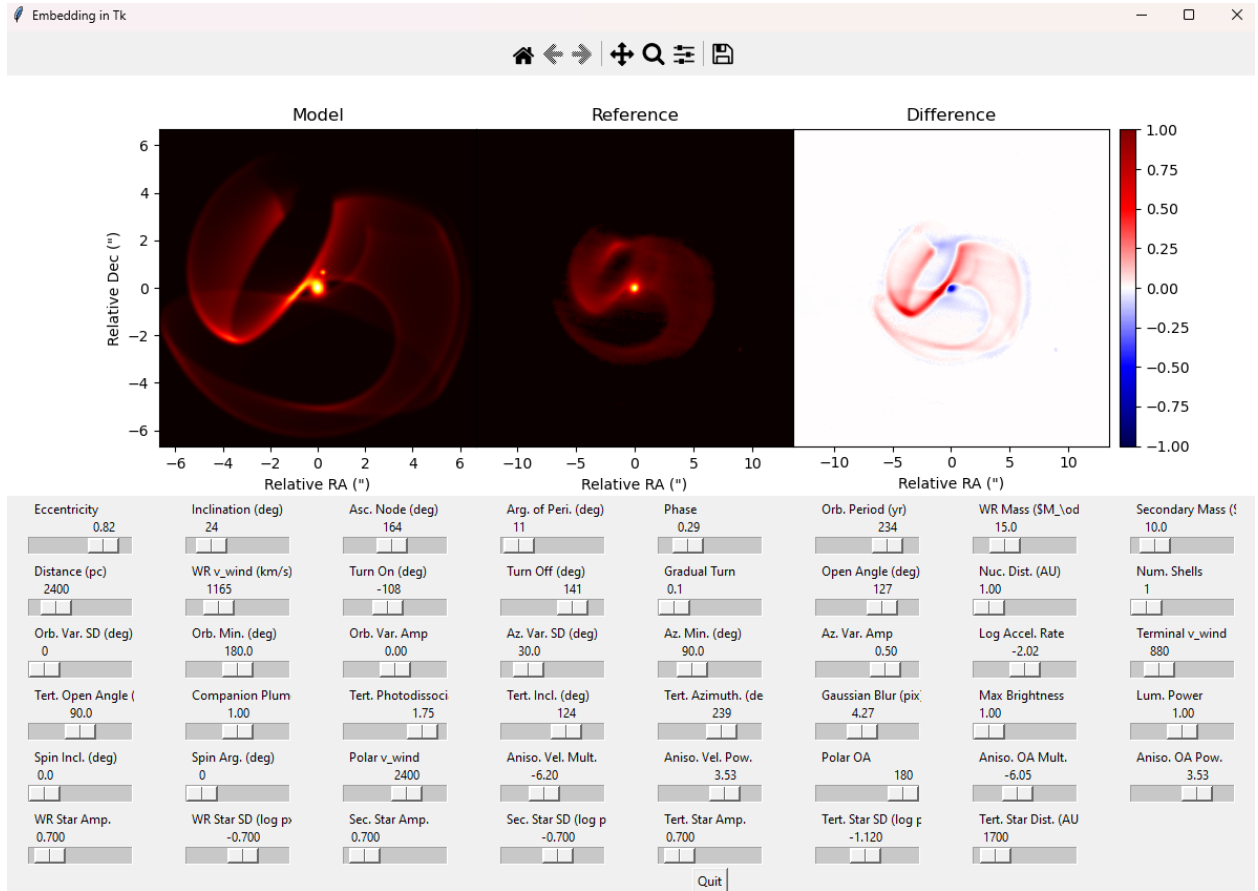


FIGURE 3.9: We designed a graphical user interface for the geometric model in order to streamline the process of finding parameter initial guesses. The position of the various sliders dictate the ‘Model’ plot in the upper right. At runtime, the user can load in a reference image shown in the upper middle plot so that they can compare the ‘Model’ and ‘Reference’. The upper right plot shows the difference in pixel values between the ‘Model’ and ‘Reference’ images, with a colourbar showing the difference scale. An animation showing the use of the GUI is available [online](#).

smoothly in space, since the contribution to each neighbouring bin changes smoothly. This allows us to continue working with a relatively simple renderer for our plume point cloud, while preserving the differentiability of our plume model.

3.4 Graphical User Interface

If statistical inference is the goal with our geometric model, we must first arrive at some initial guesses of parameter values for each CWB system. Given the sheer number of parameters that describe the model, this has long been a tedious procedure. In this Section we describe our creation of a graphical user interface (GUI) as a tool to quickly (but manually) optimise parameter guesses.

The standard Python library for creating graphical user interfaces is `tkinter`, which we have used for our GUI. This library comes with the needed basic functionality to make sliders

for each parameter, as well as `matplotlib` (Hunter, 2007) integration which is required to display our simulated plots. Figure 3.9 shows the final version of our GUI, where we have sliders for all discussed parameters so far as well as those that are yet to be discussed in Chapter 5.

An important criteria for the GUI is the ability to compare the current iteration of a model to a reference. For this reason we chose to display three plots: the first is the simulated plume given the parameter choices in the sliders pane; the second is a reference image that can be set at runtime, usually of the observed image of the CWB of interest; the third is a difference plot showing how closely the model resembles the reference image.

The use of a GUI for the CWB geometric model is only possible with our JAX-based code. Previous iterations of the geometric model code (that had of order ~ 5 s compute time per model evaluation) were prohibitively slow, given that the ‘Model’ pane in the GUI is updated at every slider repositioning. With our model evaluation time of $\lesssim 0.1$ s, the changing of parameters is smooth and intuitive. Given its speed, we plan to eventually provide this GUI as a webapp so that anyone may hone their intuition for CWB parameters with minimal overhead.

3.5 Modelling Light Curves

Before the first images of the Wolf-Rayet colliding wind binaries became available, many system parameters could be strongly constrained using their visible and infrared light curves. The light curves of these systems give valuable information about the phase dependence of dust production, and, naturally, the period and other characteristics about the binary orbit. The CWB X-ray light curves in particular have been well modelled for a range of systems; this modelling gives detailed information about the physics at the colliding wind shock, and more broadly about the mass loss rates and chemistry of the two component stellar winds (Walder et al., 1999; Parkin & Pittard, 2008). More recently, the radio light curves of O+O binaries have been modelled (Pittard, 2010) as well as of the Apep system (Bloot et al., 2022), albeit not across a whole orbit.

Today, there exists a wealth of infrared light curve data on many Wolf-Rayet colliding wind binary systems. Despite this, there appears to be no published light curve modelling to reproduce this infrared photometry. In order to make a light curve, one must evaluate a brightness model at several orbital phases to form a complete timeseries picture. In order to make an infrared light curve for a WR CWB, one must do this costly procedure on a model of the dust nebula itself. Given that hydrodynamical simulations are typically used to model the CWB dust nebula, the compute time per light curve quickly becomes intractable.

Using our fast geometric model, we present here the first infrared light curve model for the WR CWBs. To construct a light curve, we evaluate our geometric model at several phase values; for each model evaluation we take the brightest pixel in the subsequent render as being representative of the total flux at that epoch. When plotted, e.g. in Figure 3.10 for WR 140, we see a smoothly changing flux over time that closely matches the observed light curves.

The most physically motivated way to calculate the flux at each epoch would be to sum the total pixel values across the image – the ‘integrated flux’ – weighted by the dust cooling



curve, although we are not able to do this with our model. Since each dust shell consists of the same number of particles and the brightness of each pixel is determined by the number density of particles, the integrated flux of each of our renders is constant. The cooling of (and therefore the dimming in the infrared emission of) dust as it expands is not a part of our purely geometrical model. Therefore, in order to get some degree of variability in our light curve, we posit an approximation that the mean value of the 50 brightest pixels (roughly 0.1% of the pixels in a 256×256 pixel image) yields a suitable substitute for the integrated flux. Indeed, observations of bright sources are typically saturated by a small number of bright pixels which dominate the photometry. Physically, the dust-producing CWBs are brightest when copiously producing dust and this holds true in our geometric model. Recall that in our model each generated ring hosts the same number of particles, therefore when new rings are created at the nucleation distance their angular scale is very small and the number density of particles per pixel is very high; those pixels at the site of dust formation are then very bright as a result, and this emulates the true physical process to a surprising degree.

In the case of the WR 140 light curve shown in Figure 3.10, we note that our model curve seems to replicate some observed filter curves better than others. In particular, the strong double peak structure of our model curve most resembles $8.75\text{ }\mu\text{m}$ filter light curve. A filter with a central wavelength of $8.75\text{ }\mu\text{m}$ will be integrating over the blackbody emission from warm dust at around $\sim 330\text{ K}$. Previous work suggests that the dust in these WR CWBs forms initially at about $\sim 1000\text{ K}$ and quickly cools (Lau et al., 2023), so we would expect a rapid light curve fall off in filters that probe hotter dust and a more gradual fall off for filters deeper into the infrared. Since our light curve only traces dust formation, we should expect that it will be a closer fit to observations in filters whose transmission integrates over wavelengths corresponding to warm dust blackbody emission.

Results so far with our light curve model are promising, but not without limitations. The benefit of our model lies in its computational efficiency in being able to produce a well sampled light curve in a matter of seconds. There is significant potential for future development of this modelling, especially in linking our plume geometry with a radiative transfer model (e.g. MCFOST, Pinte et al., 2006) and integrating over that flux to yield a more physically motivated light curve.

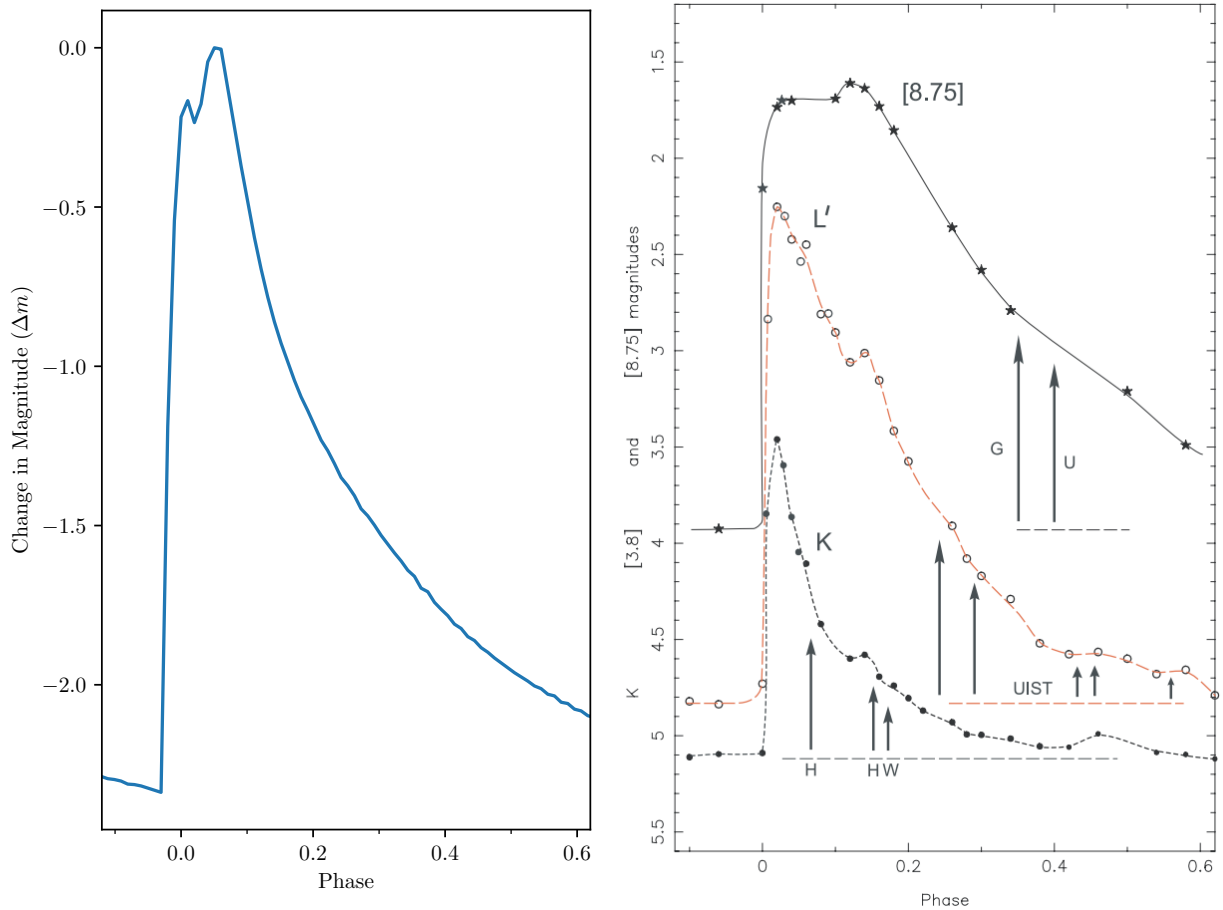


FIGURE 3.10: Our modelled light curve of WR 140 matches closely the observed infrared light curves. *Left:* The 2-shell model light curve shows a distinct double peak and smooth fall off in ‘flux’, with the first peak occurring immediately prior to periastron ($\phi = 0$). By default, the light curve is calculated on a 256×256 pixel rendered image. *Right:* The observed infrared light curves of WR 140 in several different bandpasses, from Williams et al. (2009), showing that the fall off tends to be steeper in shorter wavelength bandpasses.



4

The First Model of WR 48a

As discussed in Chapter 2, the WR 48a system is the next serious candidate WR+WR dust producing CWB following the confirmation of a WC+WN binary in Apep. It is a rare and valuable laboratory to study the effects of two massive stars in close proximity with entangled winds, and even more so if the tentative double WR classification holds true. In this Chapter we review archival observations of WR 48a spanning over 30 years and present the first attempt at modelling the associated colliding wind nebula geometry. We then comment on the likelihood of the system having two WR stars as opposed to the much more common WR+O binary classification.

4.1 Geometry Using Archival Data

Among the first Wolf-Rayet systems identified as a colliding wind binary, WR 48a has been observed and studied for longer than most other CWB systems. As a result, there exists a wealth of data, much of which has not been studied in the same detail as in other systems. To our knowledge there has been no previous attempt to model the geometry of the WR 48a dust nebula despite the system being imaged over 20 years ago at the time of writing. In this Section we present the first such attempt, visualised in Figure 4.1 with the associated orbital and stellar parameters in Table 4.1, and discuss the motivation behind parameter choices. The image itself provides strong constraints on some but not all of the parameters, and so we use the well-sampled light curve of WR 48a (Figure 4.2) to support our parameter search.

The WR 48a image and light curve both show clear signs of episodic dust production. In the image, this manifests as discontinuous spatial jumps in dust locations seen particularly around the $\sim 110^\circ$ and $\sim 250^\circ$ positions relative to the central bright source. This is the main consideration in our choice of $\nu_{t,\text{on}}$ and $\nu_{t,\text{off}}$. In the light curve, the distinct peaks and subsequent gradual fall off in flux suggest episodic dust production (Williams et al.,



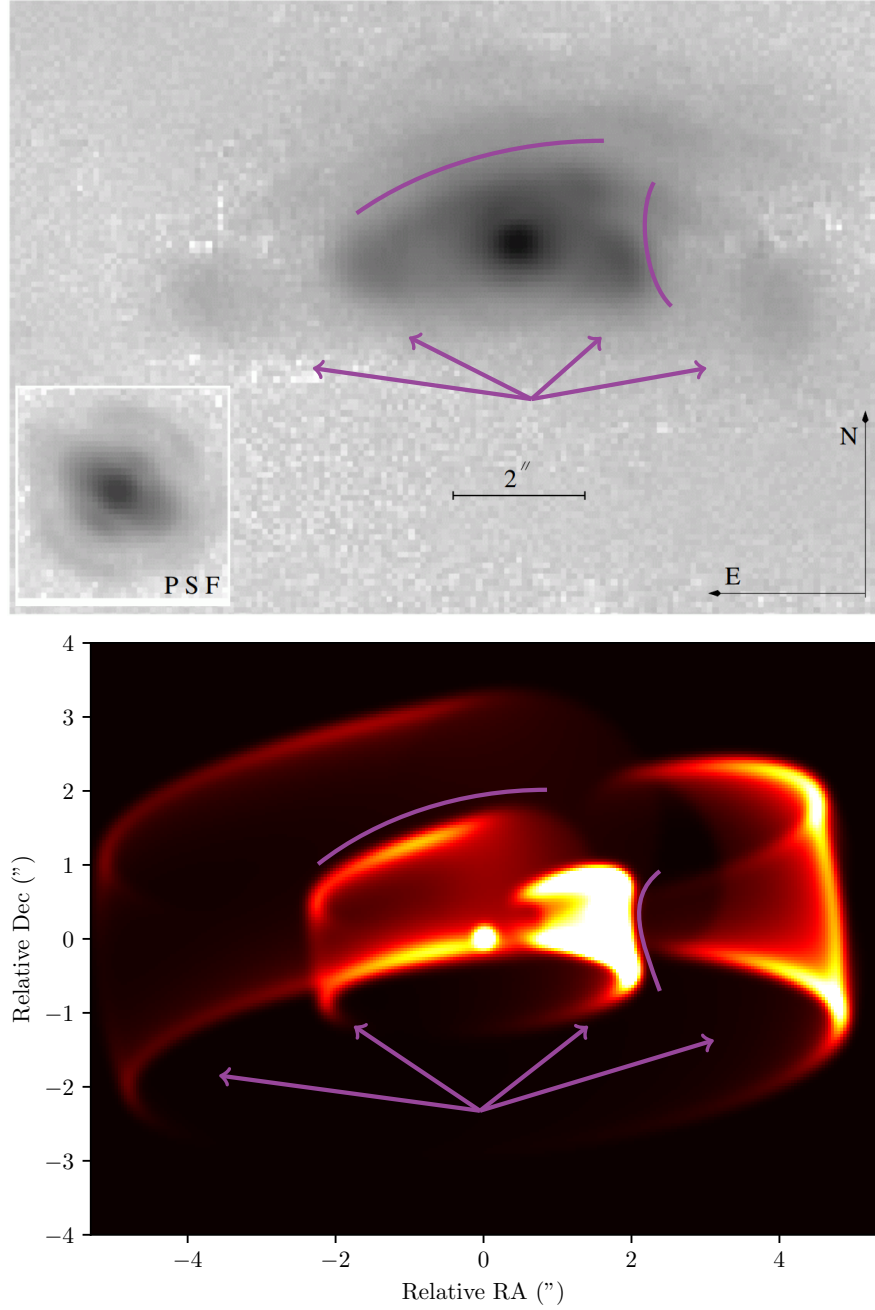


FIGURE 4.1: Our nebula model of WR 48a reproduces many of the geometric features in the observed image. *Top:* The TReCs/Gemini-South (De Buizer & Fisher, 2005) image of the WR 48a dust nebula shows inclined concentric shell structure (darker is brighter). Image from Marchenko & Moffat (2007). *Bottom:* Our attempt at modelling the plume geometry in the above figure, with the parameters as in Table 4.1. The annotated purple lines indicate key geometric features that were considered in the fitting: arrows correspond to the periastron ingress (left arrows) and egress (right arrows) showing the effect of orbital modulation in dust production, while curved lines show other notable ridges. We have an animation available online [online](#) that shows the evolution of the nebula with our parameters over one orbital period.

Parameter	Value	Reference
Eccentricity, e	$0.74^{+0.05}_{-0.15}$	This work
Inclination, i	$(74 \pm 15)^\circ$	This work
Long. of Asc. Node, Ω	$(174 \pm 10)^\circ$	This work
Arg. of Periastron, ω	$(124 \pm 20)^\circ$	This work
Opening Angle, θ_{OA}	$(37^{+5}_{-10})^\circ$	This work
Orbital Period, P_{orb}	32 ± 2 yr	W12, Z14
Orbital Phase at March 2004, ϕ_{2004}	0.78 ± 0.02	This work
Distance, d	~ 4 kpc	W12, Z14, references therein
Dust Expansion Speed, v_{wind}	1700 ± 200 km s $^{-1}$	Z14
Dust Turn On True Anom., $\nu_{t,\text{on}}$	$(-121 \pm 25)^\circ$	This work
Dust Turn Off True Anom., $\nu_{t,\text{off}}$	$(137 \pm 15)^\circ$	This work
Gradual Turn On/Off, σ_{gradual}	$(19^{+5}_{-10})^\circ$	This work
Orbital Modulation, σ_{orb}	$(40 \pm 20)^\circ$	This work
Azimuthal Variation, σ_{az}	$(45 \pm 10)^\circ$	This work

TABLE 4.1: Our best-fitting parameters for the WR 48a system given the geometry in Figure 4.1. References: W12 – [Williams et al. \(2012\)](#); Z14 – [Zhekov et al. \(2014\)](#).

[2012](#)). Following the gradual fall in flux, a gradual rise in flux beginning in 2004 precedes the expected periastron passage. The form of the curve is entirely unlike the sudden and steep rise in flux exhibited by WR 140 (Figure 3.10), for example. This motivates the use of the ‘gradual turn on/off’ feature incorporated into the model, wherein dust production does not suddenly start or stop, but rather smoothly changes with true anomaly. We find that a gradual change in dust production over a $(19^{+5}_{-10})^\circ$ standard deviation in true anomaly best fits both the light curve model and the observed geometry. There is evidence for this gradual effect in the north-western regions of Figure 4.1, where there is only faint evidence of dust emission in a spiral arm. With the adopted geometry, the dust production rate appreciably increases at $\phi \simeq 0.74$ and ‘turns off’ at $\phi \simeq 0.44$, in agreement with the bumps and falls in the observed light curve.

The eccentricity of the system was previously suggested to be $e \sim 0.6$ by [Williams et al. \(2012\)](#). This is corroborated by the fact that some variable conditions at the colliding wind interface – such as the stars moving closer and subsequently further apart from eccentric orbital motion – is needed to explain predictable episodic dust formation. We began our parameter search with $e \sim 0.6$ and found that slightly higher eccentricity best describes the geometry. With the orbital period and phase at 2004 so well determined, varying the eccentricity changes the distance of the south-west and south-east ‘lobes’ relative to the central stars. Hence the eccentricity is mainly dictated by how well those positions can be constrained.

An eccentric orbit allows for exotic geometry as the shock conditions change. The high eccentricity of WR 140 results in the dust production rate at periastron being significantly



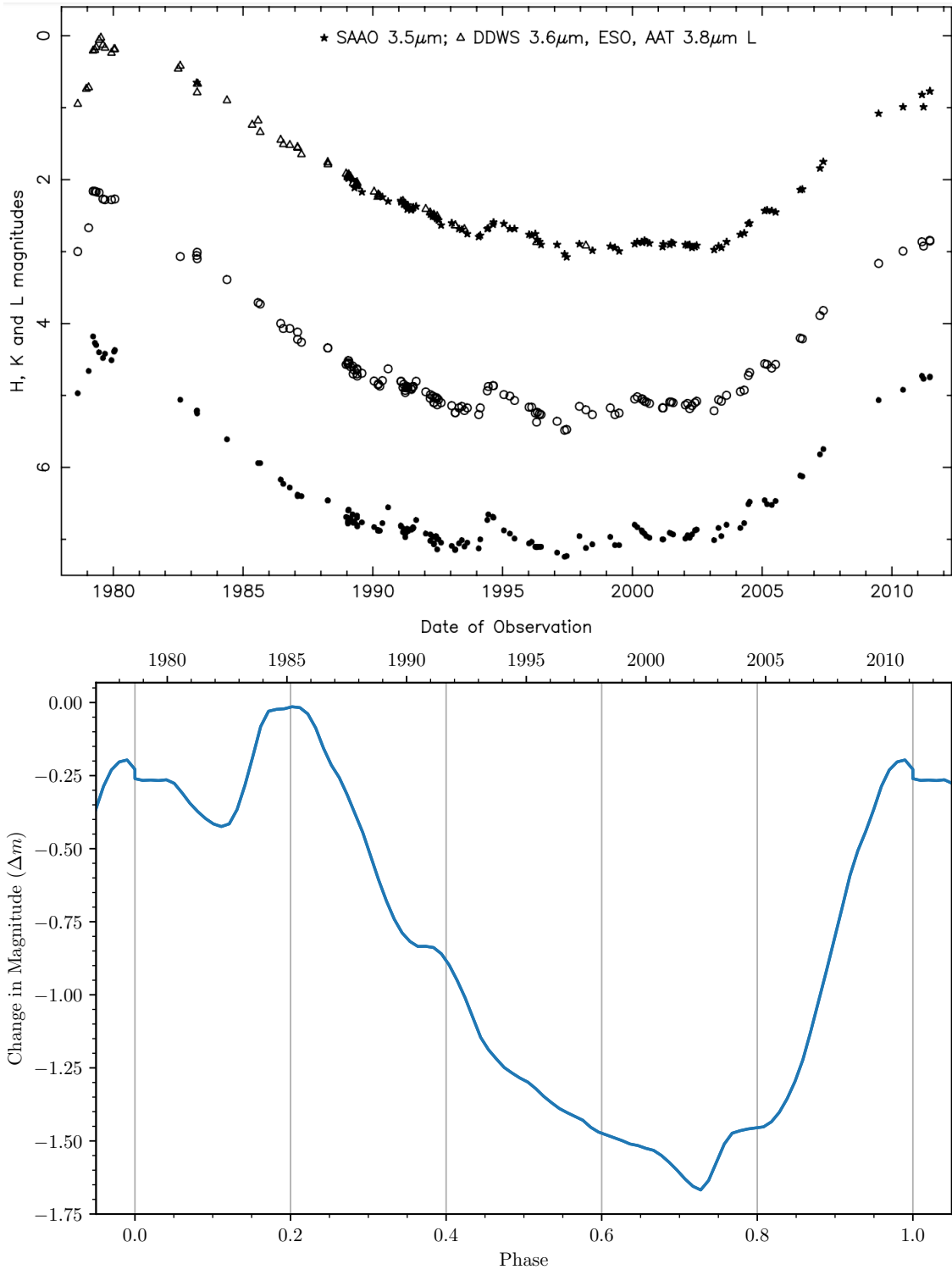


FIGURE 4.2: Our model light curve of WR 48 reproduces many of the observed features well. *Top:* Photometry over ~ 34 years produces an almost complete light curve of the WR 48a system with an expected period of 32 years, from Williams et al. (2012). *Bottom:* Our 5-shell model of the WR 48a light curve given the geometry in Figure 4.1 and Table 4.1, generated on a 600×600 pixel grid and convolved with a $\sigma = 0.01$ Gaussian blur in phase (using SciPy's `gaussian_filter` function, Virtanen et al., 2020).

reduced because the shock occurs closer to the stellar surfaces. We see evidence of this same phenomenon in WR 48a in the region directly to the south of stars in Figure 4.1. Here, the dust in the east (left) region forms first and soon drops in production rate; after periastron passage, again the dust production increases in rate, forming the nebula arms in the west (right) before gradually turning off. We find that an orbital modulation standard deviation of $(40 \pm 20)^\circ$ in true anomaly best describes these observations, similar to the $(40^{+30}_{-10})^\circ$ modulation in WR 140 (Han et al., 2022).

This modulation near periastron also affects the light curve profile of the system: in WR 140 this manifests as a narrow but sharp dip in brightness that causes double peak centred around periastron, whereas in WR 48a this causes a smoother initial rise with a delayed peak. Since we estimate the system as being slightly less eccentric than WR 140 (which has $e \simeq 0.89$), we expect those periastron modulation light curve features to be smoothed in orbital phase and time. We note that our model light curve has an appreciably higher flux around the year 1985 than observed; all observed filters are in the wavelength range $3.5 - 3.8 \mu\text{m}$ which corresponds to reasonably hot dust, however we established in Figure 3.10 that our light curve model seems most accurate for wavelengths $\gtrsim 9 \mu\text{m}$. We suggest that we would see a broader double peak consistent with our model in a light curve deeper in the infrared.

With only two published images of WR 48a, it is difficult to accurately constrain the Wolf-Rayet wind speed through the observed plume expansion. Lau et al. (2020a) show a VISIR epoch of WR 48a in 2016 (12 years after the original Gemini image), although they adopt the Gaia parallax distance of 2270 pc to WR 48a to convert plume expansion into a wind speed of 1000 km s^{-1} . Unfortunately Gaia distances to Wolf-Rayet CWBs have been notoriously unreliable (in this case it is a factor ~ 2 smaller than other estimates), and so this derived wind speed may not be accurate. If we instead adopt the Zhekov et al. (2014) ~ 4 kpc distance with the observed angular expansion speed, we arrive at a similar wind speed value to Zhekov et al. using a terminal wind speed of 1700 km s^{-1} , common for stars of WC8 classification. Interestingly, we find that this expansion speed is consistent with the geometry shown in Figure 4.1. Our choice of inclination, argument of periastron, and longitude of ascending node are primarily to align the observed ridges in the Gemini image. We believe that the south-west/east lobes are suitably positioned in the model, so that the northern spiral bars are then particularly constraining of the inclination.

4.2 Is WR 48a a WR+WR Binary?

Potentially the most interesting result to come out of our WR 48a geometric model is the unusually narrow plume opening angle that best fits the image. To align the spiral structure and the lobes at the $\sim 110^\circ$ and $\sim 250^\circ$ positions we required an inclination of $i = (74 \pm 15)^\circ$ and plume opening angle of $\theta_{\text{OA}} = (37^{+5}_{-10})^\circ$. We note that the geometry could also be suitably fit with an opening angle as low as 30° and inclination as high as $\sim 85^\circ$. If the WR+WR hypothesis for WR 48a is to be considered, the most natural comparison for its parameters is with the only confirmed WR+WR system: Apep. Immediately we see a major difference in WR 48a from Apep; Han et al. (2020) cite the full opening angle of Apep as $(125 \pm 10)^\circ$ which is over 3 times larger than what we estimate in WR 48a.



The wind momentum ratio (Equation 2.2) is a useful tool to learn about the relative properties of stellar winds in a binary. Without knowing the mass loss rates and velocities of each stellar wind, however, this is difficult to constrain unlike the observed shock opening angle. Supported by hydrodynamical simulations, we consider two approximate functional forms of the shock opening angle θ_{OA} to the wind momentum ratio, η , of the two stars. The first is from Eichler & Usov (1993),

$$\frac{\theta_{\text{OA}}}{2} = 2.1 \left(1 - \frac{\eta_{\text{W/S}}^{2/5}}{4} \right) \eta_{\text{W/S}}^{1/3} \quad (4.1)$$

which when solved – with θ_{OA} converted to radians – gives information about the momentum ratio of the weaker wind (subscript W) compared to the stronger (subscript S) wind. With Equation 4.1 and a full opening angle of θ_{OA} we yield $\eta_{\text{W/S}} \simeq 0.00395$. The second equation we consider is from Tuthill et al. (2008); Gayley (2009),

$$\eta_{\text{S/W}} = \left(\frac{121}{\theta_{\text{OA}}/2} - \frac{31}{90} \right)^3 \quad (4.2)$$

which gives information about the stronger wind relative to the weaker wind. When solved, we obtain $\eta_{\text{S/W}} \simeq 237.9$. Since $\eta_{\text{S/W}} = 1/\eta_{\text{W/S}}$, we find that the first equation gives $\eta_{\text{S/W}} \simeq 253.2$, in reasonably close agreement with Equation 4.2. Going forward, we adopt the rough midpoint of these two estimates, $\eta_{\text{S/W}} = 245$. Even at the upper uncertainty limit in our geometric fit (with $\theta_{\text{OA}} + \sigma = 42^\circ$), Equation 4.2 yields a momentum ratio of $\eta_{\text{S/W}} = 159$, meaning that we can be confident in there being a significant momentum imbalance between the two stellar winds.

The most in-depth spectral analysis of WR 48a yet suggests that the dust-driving WC star has a WN8h companion (Zhekov et al., 2014), although the companion has been assumed to be a main sequence O star in other works (Williams et al., 2012; Lau et al., 2020a, see the latter for a more recent VLT/VISIR image of WR 48a). If we adopt the values chosen by Zhekov et al. (2022) of $\dot{M}_{\text{WC8}} = 2.92 \times 10^{-5}$, $\dot{M}_{\text{WN8h}} = 4.05 \times 10^{-5}$, $v_{\text{WN8h}} = 1000 \text{ km s}^{-1}$ and our adopted $v_{\text{WC8}} = 1700 \text{ km s}^{-1}$, using Equation 2.2 we obtain $\eta_{\text{WC8/WN8h}} \simeq 1.22$, significantly discrepant to the observed shock opening angle. If we choose parameters more akin to those found for other WN8h type stars, e.g. $\dot{M}_{\text{WN8h}} = 10^{-4.74}$ and $v_{\text{WN8h}} = 650 \text{ km s}^{-1}$ (Crowther & Smith, 1997; Nishimaki et al., 2008), we instead obtain $\eta_{\text{WC8/WN8h}} \simeq 4.2$, still two orders of magnitude discrepant.

As a result of this tension between a wind momentum ratio seen in the geometry and that with typical WC+WN8h wind parameters, we suggest that the companion to the dust producing WC star in WR 48a is unlikely to be a Wolf-Rayet star. This is at odds with the spectral modelling of the system which is apparently best reproduced by the superposition of WC8+WN8h spectra, and long term spectroscopic monitoring may provide much needed insight into what lies at the heart of the WR 48a colliding wind binary. The requirement of there being only one WR star in the system further cements the Apep system – with a confirmed WC8+WN4-6 central binary – as a one-of-a-kind Galactic laboratory for Wolf-Rayet colliding wind physics and binary stellar evolution.

EPHRAIM WINSLOW

What made your last keeper leave?

THOMAS WAKE

He believed that there was some
enchantment in the light. Went mad,
he did.

The Lighthouse (2019)

5

The Geometric Model as a Probe into the Physics of Apep

In the previous Chapter, we showed how the candidate dusty WR+WR system WR 48a likely only harbours one Wolf-Rayet star. We now turn our attention to the colliding wind nebula of the only presently confirmed WC+WN binary – Apep – using our geometric model to infer the underlying physics beyond our direct view. We utilise four epochs of infrared imaging taken with the VLT as well as a single JWST epoch to infer the most accurate orbital parameters of Apep yet. Section 5.1 details this new data as well as our fit parameters, and Section 5.2 discusses newly found evidence of dust destruction in the Apep system that confirms the association of the Northern O star companion.

5.1 Updated Parameters from the VLT and JWST

The WC8+WN4-6 system Apep has been intensely studied since its discovery as a colliding wind binary and subsequent imaging in [Callingham et al. \(2019\)](#). In the papers that followed, the inner binary of the system was quickly established as being the longest period CWB known with an estimated 125 year orbit, and a dust plume expansion speed in direct contradiction of the spectroscopic wind speed by at least a factor of 2 ([Han et al., 2020](#)). This expansion speed was determined over 3 epochs of VLT/VISIR ([Lagage et al., 2004](#)) 8.72 μm imaging in the years 2016, 2017, and 2018, and an adopted distance of 2.4 kpc.

Here we present a fourth epoch of VISIR imaging taken in 2024 which triples the previous phase coverage of the orbit. This alone allows us to more sensitively constrain the eccentricity and present phase of the binary orbit through our geometric model; for orbits that are less eccentric, the plume will evolve in shape more over the same time period and conversely highly eccentric orbiters will have a comparatively stable dust plume geometry after production ceases. We show the four epochs of VISIR imaging in Figure 5.1, observed

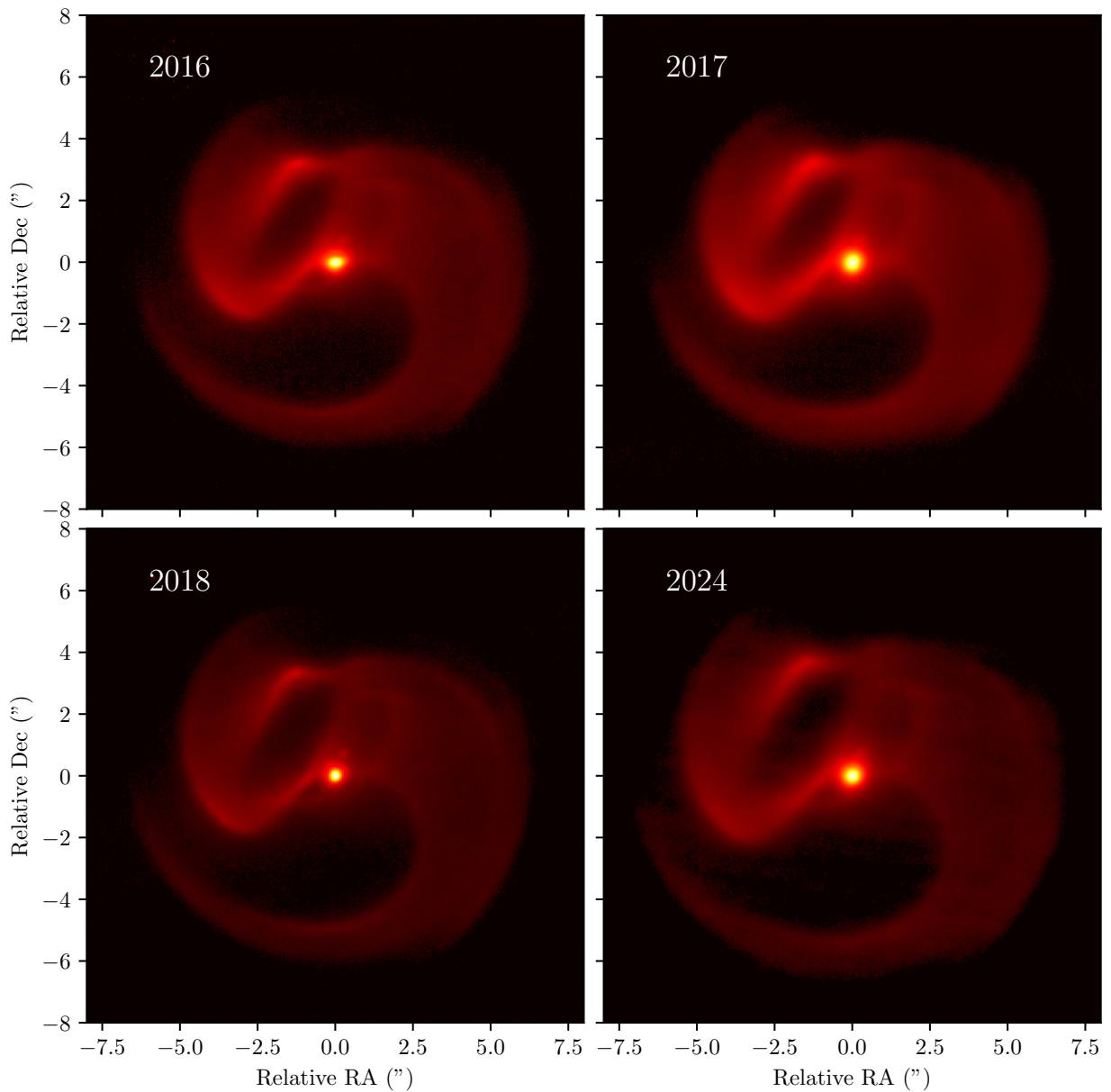


FIGURE 5.1: The four epochs of VLT/VISIR Apep images visibly show plume expansion over an 8 year duration. The images were taken in the $8.72\text{ }\mu\text{m}$ filter on VISIR, and are processed according to description in the text. The pixel resolution of each image is $10^3 \times 23/512 \simeq 44.922\text{ mas per pixel}$. An animation of these four images showing the expansion over time is available [online](#)

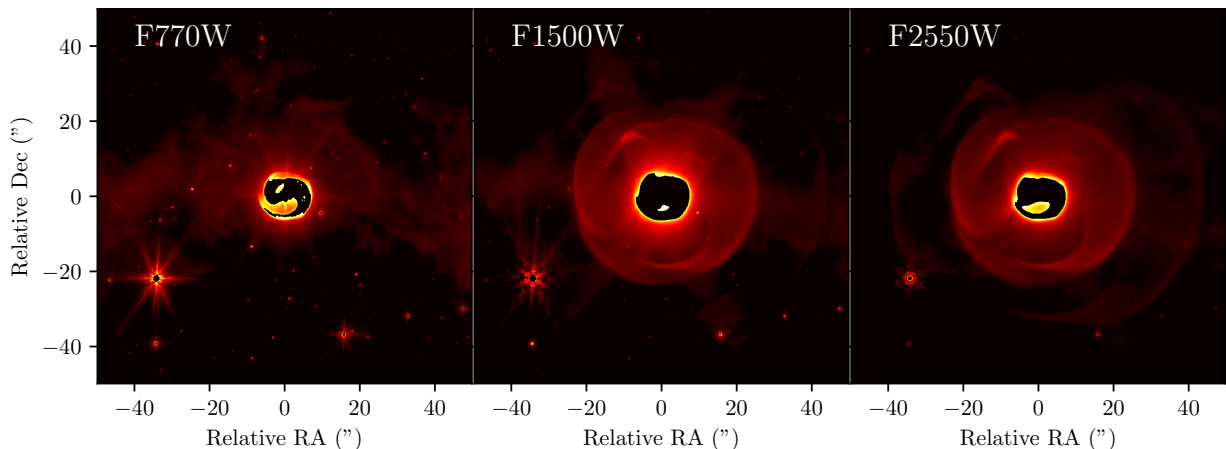


FIGURE 5.2: Apep was observed with JWST/MIRI in three filters in 2024. Each frame corresponds to the filter centred on emission at $7.7\ \mu\text{m}$, $15\ \mu\text{m}$, and $25.5\ \mu\text{m}$ respectively. The majority of the inner shell in each frame is largely saturated and plotted with NaN values, although the core values can be recovered with the zero-group images in the $7.7\ \mu\text{m}$ and $25.5\ \mu\text{m}$ bands (which are used in Figure 5.3). These images are processed similarly to the VISIR images in Figure 5.1, although here with a 60th percentile background subtraction.

in an infrared filter centred on $8.72\ \mu\text{m}$ and plotted in false-colour with the `matplotlib` ‘hot’ colourmap. In these images and in our analysis, we work with slightly processed versions of the raw data: the background was removed via an 84th percentile flux subtraction, the maximum flux was normalised to 1 across the images, a flux floor of 0 was imposed, and the brightness was uniformly increased with a square-root power on the flux. We modified the image in this way to minimise the effect of the background and to bring out finer details in the ridge geometry for fitting.

For the first time, the *James Webb Space Telescope* observed the Apep system on July 2024 as part of Cycle 3 (GO Program 5842). The dust plume was observed in 3 filters, centred on $7.7\ \mu\text{m}$, $15\ \mu\text{m}$, and $25.5\ \mu\text{m}$, and we show the processed images in Figure 5.2. Immediately we see second and third concentric shells in the $15\ \mu\text{m}$ and $25.5\ \mu\text{m}$ images which are not visible in the $7.7\ \mu\text{m}$ or VISIR images. Since the dust within the colliding wind nebula is visible via blackbody emission, the geometry over the different filters describes the temperature profile of the dust. We expect that this dust forms at $\sim 10^3\ \text{K}$, and so cooler blackbody emission directly translates to older dust. Indeed, the outer shells correspond to previous rounds of dust formation when the inner WR+WR binary was previously near to periastron. In this way, coupling the angular separation between the shells together with the angular expansion speed from the four VISIR epochs allows us to uniquely constrain the orbital period of the inner binary independent of a distance measurement to the system.

Since we have monochromatic images in three wavelengths, it is natural to combine them into a composite, false-colour image. The false-colour JWST image for Apep is shown in Figure 5.3, and has been processed to bring out the saturated inner shell emission (seen as NaNs in Figure 5.2). We carefully note that this false-colour image has limited quantitative scientific value; rather it yields an excellent qualitative, human-interpretable vision of the



FIGURE 5.3: Mapping the three observed JWST filters to RGB allows us to make a colour composite of Apep. This image was created by Benjamin Pope and Shashank Dholakia, who together processed the image by de-saturating the inner shell core and colourmapping the filters. See page iv for a full-page version of this image.

overall geometry. For example, Figure 5.3 emphasises the background nebulosity of the Milky Way, seen in the blue diffuse flux around the image. We considered whether or not this nebulosity could be associated with Apep, perhaps as hot gas ejected from the system as collimated jets, but the most likely interpretation is background emission; Apep lies in the plane of the Milky Way, and so we would expect a significant density of dust along the line of sight.

Using our geometric model, in Figure 5.4 we simultaneously fit all four epochs of VISIR data (Figure 5.1) together with the $25.5\text{ }\mu\text{m}$ MIRI image (Figure 5.2, right side). Table 5.1 shows our inferred parameters for Apep at the 2024 epoch as visible in the ‘Model’ pane of Figure 5.4. For the JWST pane, we chose to fit specifically to the $25.5\text{ }\mu\text{m}$ image since it had the least background nebulosity as well as the most visible structure of the third shell; in the geometric fitting, we do not directly consider temperature profiles and so we need only the most prominent ridges to fit to. In considering the previous VISIR epochs, we only fit the orbital phase in the year 2024, generating the model for previous years with a calculated phase $\phi_{\text{year}} = \phi_{2024} - (2024 - \text{year})/P_{\text{orb}}$.

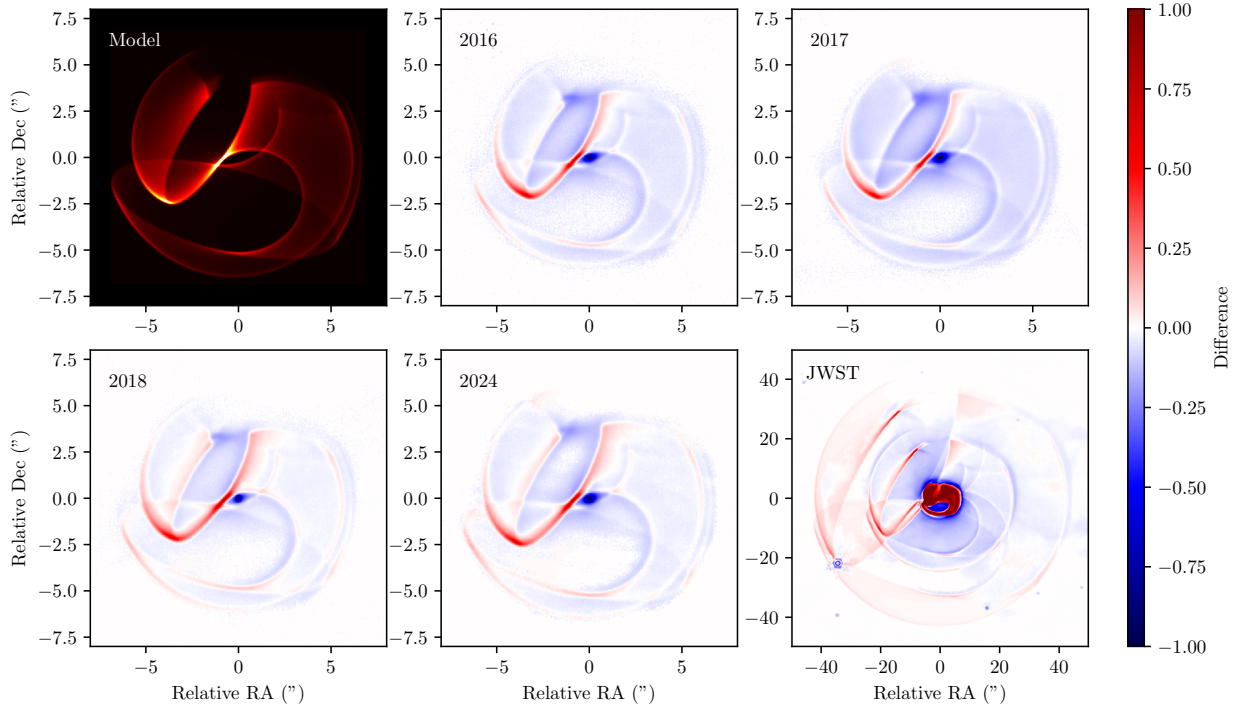


FIGURE 5.4: Using the 4 VLT epochs plus the JWST image, we found parameters for our geometric model that faithfully reproduce the observed geometry; the numerical values of each parameter are shown in Table 5.1. The top left panel shows the model geometry at ϕ_{2024} , and all other panels show the difference imaging of $F_{\text{model}} - F_{\text{obs}}$ adjusted for the respective orbital phases. Although the exact flux often does not cancel out in the difference imaging, we note the nebula ridge positions align very well. This geometry includes the effects discussed in Section 5.2. We have an animation available [online](#) that shows the evolution of a shell with our parameters over one orbital period.

While many of the parameters in Table 5.1 are similar to previous works, e.g. opening angle and dust turn on/off, several are considerably different driven by the requirement to fit the new data. In particular, some configurations of orbital phase, orbital period, and eccentricity are degenerate for the VISIR data; with the location of a second and third shell found in the JWST data, this degeneracy is broken. What we find now is that the WR+WR binary in Apep is more eccentric than previously thought, with a value of 0.82 ± 0.04 compared to the previous 0.7 ± 0.1 estimate. Similarly, we find that the orbital period of the inner binary is almost twice as long as previously thought, with a period of 234 ± 10 yr compared to the previous estimate of 125 ± 10 yr. In order to reproduce the observed dust distribution across all images, we now require a correspondingly smaller orbital phase of $\phi_{2024} = 0.35 \pm 0.02$ compared to the previous estimate of $\phi_{2024} \sim 0.66$; while this means that the dust is younger relative to the orbital period, the absolute age of the dust we see in the inner shell is consistent with previous parameter estimates of about 75 yr (at the 2016 epoch). This positions Apep as an unusually long period binary not only among the CWBs, but also among all known WR binaries, whose orbits overwhelmingly tend to have short periods (Deshmukh et al., 2024).



Parameter	Value	Reference
Eccentricity, e	0.82 ± 0.04	This work
Inclination, i	$(24 \pm 3)^\circ$	This work
Long. of Asc. Node, Ω	$(164 \pm 15)^\circ$	This work
Arg. of Periastron, ω	$(10 \pm 10)^\circ$	This work
Opening Angle, θ_{OA}	$(126 \pm 5)^\circ$	H20, This work
Orbital Period, P_{orb}	$234 \pm 10 \text{ yr}$	This work
Orbital Phase at July 2024, ϕ_{2024}	0.35 ± 0.02	This work
Distance, d	$2.4^{+0.2}_{-0.5} \text{ kpc}$	C19, H20
Dust Shell Expansion Speed, v_{wind}	$860 \pm 100 \text{ km s}^{-1}$	This work
Dust Turn On True Anom., $\nu_{t,\text{on}}$	$(-108 \pm 10)^\circ$	This work
Dust Turn Off True Anom., $\nu_{t,\text{off}}$	$(141 \pm 10)^\circ$	This work
Azimuthal Variation, σ_{az}	$(30 \pm 10)^\circ$	This work

TABLE 5.1: Our best-fitting parameters for the Apep system. The opening angle parameter θ_{OA} is slightly updated from the reference, and we make no attempt to fit for the distance to the system. References: C19 – [Callingham et al. \(2019\)](#); H20 – [Han et al. \(2020\)](#).

With this new eccentricity, Apep’s membership within the family of highly eccentric CWBs akin to WR 140 is further reinforced. This means that the window in phase for which dust production occurs is even smaller than previously thought. With our parameters we find that dust production turns on at $\phi \simeq 0.97$ and turns off at $\phi \simeq 0.10$ which translates into a dust producing duration of ~ 30 years. At the orbital distances required to host two WR stars on a 234 yr orbit (typical separation of several tens of au), we expect that the shock cooling is always adiabatic. As a rough measure of whether the CWR region is cooling adiabatically or radiatively, [Stevens et al. \(1992\)](#) introduced the cooling parameter,

$$\chi = \frac{v_8^4 d_{12}}{\dot{M}_{-7}} \quad (5.1)$$

which when $\ll 1$ is indicative of radiative cooling and adiabatic otherwise. Here, v_8 is the wind velocity in units of 1000 km s^{-1} , d_{12} is the star-CWR distance in units of 10^7 km , and \dot{M}_{-7} is the stellar mass loss rate in units of $10^{-7} M_\odot \text{ yr}^{-1}$. If we take $v_8 = 0.86$, $d_{12} = 150$ (using the semi-major axis of 56 AU from [Han et al. 2020](#) together with $r_p = a[1 - e]$) and $\dot{M}_{-7} = 500$ (a rough estimate of $10^{-4.3} M_\odot \text{ yr}^{-1}$ for both stars) we obtain $\chi \simeq 0.187$ which suggests that the shock is radiatively cooling at periastron. In the time since that paper, however, [Mackey et al. \(2023\)](#) have introduced an analogous parameter,

$$\chi_{\text{IC}} = \frac{1.61 v_8 d_{12}}{L_5} \quad (5.2)$$

which accounts for the effect of inverse-Compton cooling in the shocked wind. Here, L_5 is the luminosity of the star in units of $10^5 L_\odot$. Again, $\chi_{\text{IC}} < 1$ is evidence towards a radiatively

cooling wind. Adopting $L_5 = 3.16$ (for a star of $10^{5.5}L_\odot$), we arrive at $\chi_{\text{IC}} \sim 68$ which strongly suggests that the wind cooling is not radiative at periastron. We note that the adopted d_{12} distance does not account for the likely larger semi-major axis that would be calculated with our updated parameters (which would work to increase χ_{IC}) and that this parameter is not particularly sensitive to the chosen luminosity, so we could reasonably triple the adopted luminosity and arrive at the same conclusion that the wind is adiabatic.

Apep was already known as the Wolf-Rayet colliding wind binary with the longest known period, but with an updated orbital period of 234 ± 10 years the margin by which it is the longest has increased significantly. The next longest known WR-CWB is WR 48a with a period of approximately 32 yr (see Chapter 4), which was determined from its infrared light curve. Unfortunately, our estimated orbital period of Apep is much too long to construct a complete light curve and the last time it was at this orbital phase would be many decades prior to when Wolf-Rayet stars were first studied. With our parameters, the last periastron passage would have occurred in the year 1942 ± 4.5 and we expect the next to occur in 2176 ± 4.5 .

To investigate the possibility of anisotropic winds in Apep manifesting in the visible dust plume, we developed a simple phenomenological model as described in Section 3.2.3. One of the key observables with this model is the extension of polar lobes away from the dominant wind source, visible by a modulation in opening angle or expansion velocity or some combination thereof. When applied to our VISIR+MIRI data of Apep we did not see any evidence of such polar extension. This does not necessarily rule out the anisotropic wind hypothesis – each of the WR stars could very well have their rotation axis aligned with the orbital plane, a ‘blind spot’ in this phenomenological model – but does motivate a more rigorous treatment of anisotropic winds in a CWB in the future, perhaps with hydrodynamical simulations, to see how this really does affect the visible dust plume, if at all.

With that said, we do see some evidence of geometric discrepancy that we could not reproduce in our model. In the top-right region of each pane of Figure 5.4 we see that the true plume (shown in blue) extends further radially than our model prediction. This could be evidence of wind anisotropy, but this is localised to a single region in true anomaly whereas our simplified approach would predict two affected regions of true anomaly. Interestingly, the true anomaly of this morphological distortion is centred just after the periastron passage. The opening angle of the CWR is indicative of the wind momentum ratio at contact, and there is evidence that the wind momentum ratio and position of the shock relative to the component stars changes as a function of stellar separation (Parkin & Pittard, 2008). Therefore we would most expect to see this effect of orbital modulation in opening angle for the most eccentric CWBs. With that in mind, we might expect to see this in the dust nebula of WR 140 – the most eccentric known CWB – however there is unambiguous evidence that the dust production weakens (effectively to the point of turning off) near periastron in WR 140 and so this opening angle modulation may be present but ‘invisible’. If this is true, Apep would be the first detection of this modulation in a directly imaged CWB.

A second-order effect that may reproduce some of this same phenomenology is radiative braking, where the dominant wind shocks the subdominant wind into the latter’s acceleration region close to the secondary star (Usov, 1991; Tuthill et al., 2008). When this occurs, the radiation pressure from the secondary star slows the dominant wind thereby influencing the



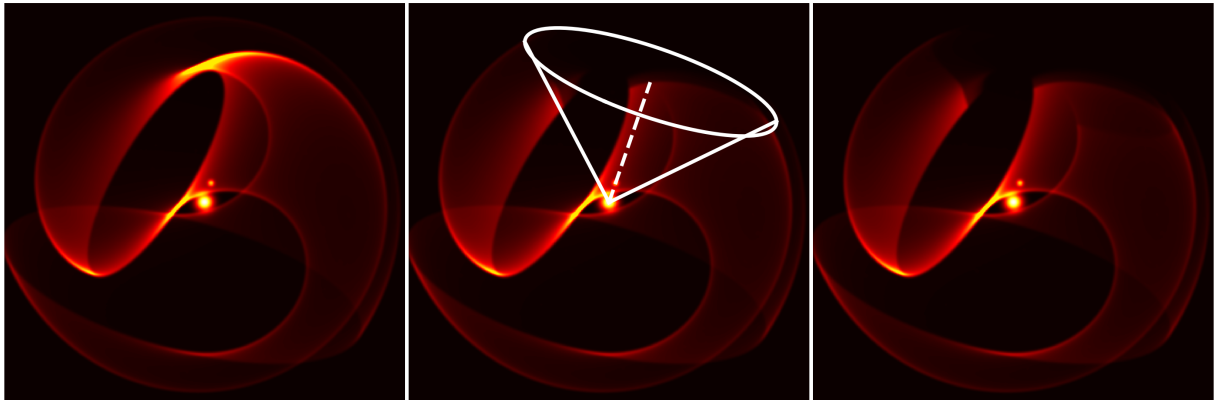


FIGURE 5.5: The Northern O star in the Apep system carves a cavity out of the expanding dust shell. The WR+WR binary is the central point source, and the Northern companion is the smaller point source above it. *Left:* Previous models do not include photodissociation effects from the Northern companion, and so overestimate the dust luminosity in the upper region of the plume. *Middle:* We model dust destruction along the volume of a cone extending out of the WR+WR central engine towards the Northern companion. *Right:* When modelling this dust destruction, the model geometry more closely matches what we see with direct imaging.

wind momentum ratio towards order unity and increases the shock opening angle as a result. If this does occur in the Apep system, its effects would need to be very small – on the order of $\sim 2^\circ$ in full opening angle – to explain what we see.

5.2 Modelling of Tertiary Effects

Since the first direct imaging of Apep, there has been uncertainty as to whether the ‘Northern companion’ O star at $0.7''$ is physically associated with the WR+WR binary, or a (improbable) chance alignment. The star has been classified as an O8 Iaf supergiant ([Callingham et al., 2020](#)), and has been suggested to be associated with the Apep WRs on account of its similar interstellar reddening along the line of sight. We present in this Section conclusive evidence that the Northern companion is dynamically bound to WR+WR binary through the signature of its interaction with the expanding dust plume.

Previous models of Apep have been successful in reproducing most but not all of the geometry of the colliding wind nebula. In particular, the northern region of each pane of Figure 5.1 is not suitably reproduced by previous versions of the geometric code (see the left pane of Figure 5.5 for a representative example of previous attempts). Upon realising that the cavity in the plume aligned perfectly with the apparent position of the Northern companion of Apep’s inner binary, we began investigating how a far off third companion could influence a colliding wind nebula. The most dominant effect appears to be photodissociation of the already formed dust once it collides with the tertiary O star wind. With this in mind, our model ‘destroys’ dust that falls within some angular distance of the tertiary star with respect to the inner WR+WR binary.

Parameter	Value
Inclination Angle, β_{tert}	$(124 \pm 10)^\circ$
Azimuthal Angle, α_{tert}	$(239 \pm 10)^\circ$
Opening Angle, $\theta_{\text{OA,tert}}$	$(90 \pm 10)^\circ$
Photodissociation Amplitude, A_{tert}	$1.75^{0.5}_{-1.0}$
Tertiary Star Radial Position, r_{tert}	$1700 \pm 200 \text{ au}$

TABLE 5.2: We use coordinates of another cone to model the photodissociation region of Apep due to the Northern companion. We show the parameters of the projected cone here, relative to the WR+WR binary orbital plane. For r_{tert} we assume the distance to Apep is $d = 2.4 \text{ kpc}$.

Like the generation of the colliding wind nebula, the photodissociation region predominantly relies on a few key parameters: the position of the tertiary star with respect to the inner binary and the cone opening angle of the photodissociation region. For the former, in the code we define the position of the third star in spherical coordinates with respect to the inner binary orbital plane. That is, we choose the angular location of the photodissociation region with a polar and azimuthal angle, β_{tert} and α_{tert} , as well as the radial distance of the third star, r_{tert} .

With these parameters, we de-weight the generated points whose angular coordinates are close enough to the centre of the cone projection axis. To calculate the angular distance, we use the formula from [Kells & Kern \(1940\)](#), modified to fit with the convention that the inclination $\theta = 0$ is at the north pole rather than $\theta = -\pi/2$:

$$\Theta = \arccos [\cos(\beta_{\text{tert}}) \cos(\beta_{\text{part}}) + \sin(\beta_{\text{tert}}) \sin(\beta_{\text{part}}) \cos(\alpha_{\text{tert}} - \alpha_{\text{part}})] \quad (5.3)$$

We then change the weighting of each point in the rendered image by a Gaussian according to their angular distance from the projected cone,

$$\delta w_{\text{tert}} = 1 - A_{\text{tert}} \exp \left(-\frac{2\Theta^2}{\theta_{\text{OA,tert}}^2} \right) \quad (5.4)$$

where A_{tert} is the amplitude of the photodissociation, Θ is the angular distance for each particle from the centre of the cone, and $\theta_{\text{OA,tert}}$ is the photodissociation region opening angle. This is then appended onto Equation 3.18 as another pre-processing step onto the final rendered plume. Rather than setting $\delta w_{\text{tert}} = 0$ for all particles with $\Theta < \theta_{\text{OA,tert}}$ we chose to model this effect with a Gaussian fall off; we would expect that all dust particles having a trajectory that impacts the tertiary O star should be dissociated, but as their impact parameter gets smaller (that is, as their trajectory deviates further from the tertiary star's position) we expect that proportionally fewer dust grains will be destroyed. As shown in Figure 5.4 (which includes the photodissociation effect with parameters as in Table 5.2), this reproduces the geometry around the tertiary star well.

Since we can include a simplified ‘bright spot’ on the rendered images to emulate the flux due to stars, we also included a third star in place of the Northern companion. If our



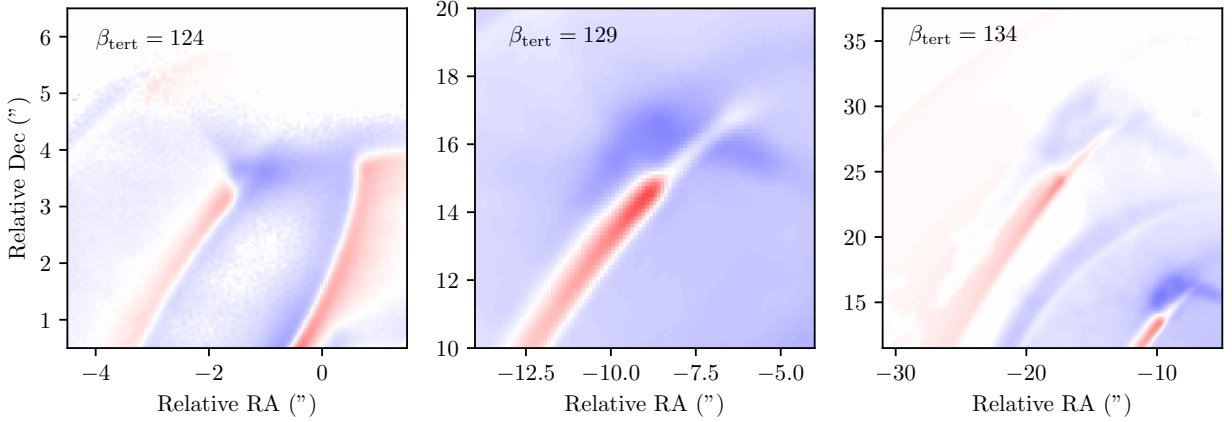


FIGURE 5.6: The JWST imagery provide evidence that the photodissociation cavity in Apep is imprinted at a different angle for each concentric dust shell. The left pane shows the 2024 VISIR image of the upper left region of the inner most shell subtracted off the model image with $\beta_{\text{tert}} = 124^\circ$ (with the same colourmapping as Figure 5.4). The middle image shows the same, but for the second concentric dust shell in the JWST image with a larger β_{tert} value. The rightmost pane shows the third concentric shell in the JWST image. The change in inclination angle of the cavity is evident by the vertical extent of the red (model) ridge versus the blue (data) ridge, which we needed to modify shell-by-shell in order to match their positions. We interpret the changing inclination angle of the cavity, β_{tert} , across each shell as being due to orbital motion of the Northern O companion responsible for the photodissociative dust destruction.

assumption that the Northern cavity is due to the tertiary star, the angular position of the modelled star should align exactly to that of the actual data. When modelling this third star at an absolute distance (that is, corrected for projection effects) of $r_{\text{tert}} = 1700 \pm 200$ au from the central WR+WR binary CoM, we find that its angular position matches that in the VISIR image exceptionally well. Put simply, we used the angular position of the cavity to constrain the angular position of the tertiary star from the central WR+WR binary, then used the $d = 2.4^{+0.2}_{-0.5}$ kpc distance to the system and the observed angular coordinate of the tertiary star to constrain its absolute distance from the central binary in spherical coordinates.

While too distant to contribute to the dust production in a colliding wind nebula, at $r_{\text{tert}} = 1700 \pm 200$ au the tertiary star is close enough to the WR+WR binary to have affected their stellar evolution and dynamics. If we naively assume that the tertiary star is in a circular orbit around the central WR+WR binary, we can quickly calculate the expected orbital period via Kepler's Third Law,

$$P_{\text{tert}} = 2\pi \sqrt{\frac{a_{\text{tert}}^3}{G(M_{\text{WN}} + M_{\text{WC}} + M_{\text{tert}})}} \quad (5.5)$$

If the star is in a circular orbit, then $a_{\text{tert}} = 1700$ au, and we can take for example the total stellar mass of all three stars as being $\sim 80M_\odot$, giving an orbital period of $P_{\text{tert}} \sim 8 \times 10^3$ yr. If this is the case, we would expect the tertiary star – and by extension its associated cavity in the dust plume – to move $\sim 32^\circ$ in its orbit around the common CoM over the 3 visible

dust shells and $3P_{\text{orb}} \simeq 700$ years of visible dust in the JWST image. We show in Figure 5.6 that there is some indication of this cavity moving across the concentric shells, although we see at most a 10° shift in the inclination across 700 years, a factor of a few too small for a circular orbit. This is marginal evidence that the tertiary star is in an elliptical orbit; we would expect that on average we view an elliptical orbiter when it is near apastron since this is where it spends the most time per orbit. Slower motion as a result of being near apastron would explain the lower-than-expected angular shift in the cavity over time than the simplest circular-orbit prediction.

If the tertiary star is in an elliptical orbit, it will have a perturbative dynamical influence on the inner WR+WR binary acting much faster than if it were on a circular orbit (Antognini & Thompson, 2016). One way of probing the perturbative timescale of three-body interactions is via the Kozai-Lidov timescale (Antognini, 2015, and Naoz, 2016 for a review),

$$P_{\text{KL}} \simeq \frac{8}{15\pi} \left(1 + \frac{M_{\text{WN}} + M_{\text{WC}}}{M_{\text{tert}}}\right) \frac{P_{\text{tert}}^2}{P_{\text{orb}}} (1 - e_{\text{tert}}^2)^{3/2} \quad (5.6)$$

which gives a timescale of eccentricity, inclination, and argument of periastron driving. If we assume that $M_{\text{WN}} + M_{\text{WC}} \sim M_{\text{tert}}$, $P_{\text{tert}} \sim 8 \times 10^3$ yr as before, and impose a modest tertiary orbit eccentricity of $e_{\text{tert}} = 0.1$, we arrive at a Kozai-Lidov timescale of $P_{\text{KL}} \sim 10^5$ yr. Since massive stars that eventually evolve into Wolf-Rayet stars have lifetimes of order a few millions of years, the Apep system has likely experienced several Kozai-Lidov timescales even if we underestimated its value by an order of magnitude. Hence, the Northern O star will have certainly influenced the dynamical history of the two WR stars in the central engine of Apep, and this may provide some clues as to the high eccentricity of the inner binary and their simultaneous Wolf-Rayet evolution.

This modelling of dust destruction from the tertiary star is successful in reproducing the observed geometry of the VISIR images in particular, but the MIRI image shows a problem in our interpretation. Comparing the photodissociation region of the innermost shell to the second shell in Figure 5.3 we see that some of the dust geometry not present in the first shell is in the middle of the cavity in the second. The left pane of Figure 5.5 illustrates what we would expect this ridge to look like, and the corresponding position in the JWST image shows that the ridge is significantly distorted, likely as a result of contact with the O star wind. One might expect that this tertiary stellar wind would shock the expanding dust plume into another cone that traces the photodissociation region, although this ridge present in the second shell provides (albeit weak) evidence against that idea.

Still, our tertiary cone modelling does not exactly produce the observed structure and one of the last remaining mysteries in the Apep plume geometry is the origin of the horizontal ridge outlining the cavity on its southern border; see the ridge structure just to the right of centre in each pane of Figure 5.6 for a zoomed view of this ridge in each shell. Our first interpretation of this ridge is that the O star may deflect some proportion of the dust onto this outer ridge, but modelling this has proven difficult. We considered and implemented several models of deflection in an attempt to explain this ridge, where the O star deflects dust particles

- into a ring along the entire cavity edge,



- onto the cavity edge on those angular coordinates co-located with the dust, or
- onto a central angular position along the cavity boundary with some azimuthal spread,

but all three models were unsuccessful in reproducing the geometry. The first two significantly over-predict ridges that are not seen in the images, and the third can produce a ridge in the correct location (by design) but at an angle which does not match the observed ridge. Given that this is a persistent feature across the shells, we do not think that this is an anomalous dust feature (created by e.g. a surface mass eruption). It will be interesting to see whether or not hydrodynamical modelling of Apep with our Table 5.1 parameters can produce this mysterious ridge.

In summary, by modifying our geometric model to include dust destruction along the volume of a projected cone, we have definitively associated the Northern companion along the line of sight to the Apep system with the inner WR+WR binary. At a present distance of $r_{\text{tert}} = 1700 \pm 200$ au this tertiary star does not directly contribute to dust production in colliding winds but could be an important piece in the puzzle of the WR+WR binary's stellar and dynamical evolution. Tertiary effects in WR CWBs have been observed before (notably in WR 147), although no evidence of photodissociation as a result of this has been shown in the literature. Any future hydrodynamical simulations of the Apep system must include this star, and this may constrain its influence on the produced dust from the inner WR stars.

6

Conclusions and Future Work

This thesis has shown our work developing from the ground up a new Wolf-Rayet colliding wind binary geometric model, and applying it to infer the parameters of two of the most unique CWBs in the Galaxy. We developed this model with computational speed and differentiability in mind, utilising the JAX framework to create a model ~ 100 times faster than previous implementations and enabling differentiable calculation with respect to every parameter.

Not only is our new model more efficient than previous works, but it also comes with many more physically motivated features than before. We have implemented the orbital and azimuthal modulation of dust production as in [Han et al. \(2022\)](#), and also included for the first time a phenomenological model for dust acceleration in the geometry from radiative pressure. Furthermore we have implemented a simple model that propagates any effect of wind anisotropy into the plume geometry.

Enabled by the speed of our new model, we created a graphical user interface for the geometric model that allows the user to change all model parameters at run time, comparing the output to an uploaded image. This has already significantly simplified the process of determining orbital/stellar parameters given an observed CWB, and we expect that this will be even more beneficial for future studies as new CWBs are observed.

We present the first infrared light curve modelling of the Wolf-Rayet colliding wind binaries, again owing its computational tractability to the accelerated codes. Constructing a well sampled light curve requires at minimum 100 model evaluations; this would be prohibitively slow for previous geometric models, but takes just seconds with our model. As an important test, we have verified the profile of our simulated WR 140 light curve against the decades-monitored photometric light curve. This significantly extends the reach of geometric models as previously fitted to image data, and in particular the light curve modelling allows us to probe into the dust production of CWB systems too distant for direct imagery. It furthermore serves as an essential consistency check, and source of additional parameter



constraint for those systems that are already imaged.

With our computational successes in creating a new geometric model, we set out to test it on the two candidate WR+WR colliding wind binaries: WR 48a and Apep. We present in this work the first geometric model of WR 48a using the archival Gemini-South data from [Marchenko & Moffat \(2007\)](#). We found that the observed colliding wind nebula is suitably reproduced with an almost edge-on orbit, accounting for orbital modulation in dust production near periastron and also with a gradual turn on and off in dust production. A relatively narrow cone open angle of $(37^{+5}_{-10})^\circ$ was needed to explain the observed plume; given this indicates a wind momentum imbalance between the two stars in WR 48a, we posit that the companion in this system is most likely an O star, although we cannot rule out a WR with an anomalously weak wind. This further positions the confirmed WC+WN system Apep as a unique laboratory to study the late-stage stellar evolution of massive stars.

In Chapter 5 we presented the first *James Webb Space Telescope* imagery of the Apep system as well new Very Large Telescope images spanning a duration of 8 years. With this new data, we were able to better constrain the orbital parameters of Apep and break previous parameter degeneracies. What we found is that the orbit of the WR+WR binary that makes the central engine of Apep is more eccentric than before and has a significantly longer orbital period of 234 ± 10 years. By modifying our model to include dust destruction effects along the volume of a cone projected out of the system, we were able to unambiguously associate the Northern O star in the Apep images to the WR+WR binary. We suggest that the orbit of this tertiary star is elliptical, and all of these findings have profound implications on the dynamical history and stellar evolution of the WR stars in Apep.

6.1 Future Work

In common with much of science, our research into the Wolf-Rayet colliding wind binaries has created more questions for every answer we find. For Apep specifically, we were unable to explain a persistent horizontal ridge on the edge of the photodissociation cavity with our geometric model. We suggest a detailed hydrodynamical treatment of this system in the future to investigate whether this ridge arises when fluid physics is considered. We are also interested in the stellar evolution history of the Apep system; this project set out with a stretch-goal of running stellar evolution codes, such as COMPAS ([Riley et al., 2022](#)), to see what initial conditions give rise to two WR stars at the same epoch in the same system. This remains an open question, and to our knowledge there have been no published attempts to investigate this.

During my work on this thesis, I submitted a proposal to observe the Apep system with VLT/VLTI – an optical interferometer that can resolve the positions of each WR star in the inner binary. This proposal was successful and is due to be observed in March 2025; we expect that we will be able to infer an astrometric orbit to the stars from these observations together with our team’s 2023 and 2024 epochs using the same instrument. If our geometric model estimate of 234 years for the orbital period is accurate, a 3 year phase coverage will not unambiguously constrain the binary orbit but may corroborate or conflict with the orbit found here via geometric modelling.

Although our new geometric model comes with more physically motivated features than

any previous iteration, more physics could be included still. We have mentioned in Section 5.1 that there may be some evidence for a varying plume geometry – whether open angle or expansion velocity – with true anomaly. This is supported by hydrodynamical studies that show that the conditions at the wind shock interface change with binary separation (Parkin & Pittard, 2008). On this note, there is motivation to include a ‘plume thickness’ parameter into the geometric model – our geometric model essentially assumes that dust is created in an infinitesimally thin ring near the shock interface, but hydrodynamical simulations suggest that dust production occurs more or less in an annulus (Pittard & Dawson, 2018). This could feasibly be modelled by imposing some scatter in the particle coordinates within each ring, and we are interested to see how this influences the observed plumes from our model.

Our model was created with the goal of performing the first statistical inference on the geometry of the CWBs, but regrettably time constraints meant that we were not able to use MCMC/HMC on our data. We share in Appendix A an overview of Hamiltonian Monte Carlo methods for statistical inference and our success in recovering the true parameters with HMC on simulated data. In doing so we have verified that the gradients of the log-likelihood with respect to each parameter are stable and HMC is a viable way forward for parameter inference of colliding wind nebulae. In that Appendix we also suggest modifications that would be beneficial to fitting our 4 epochs of VISIR data of Apep, and so the focus of future work will be on implementing these changes and subsequently performing such inference.

At the time of writing, several more CWBs have been observed with JWST-MIRI as part of the JWST GO 4093 program: WR 125, WR 137, WR 112, and notably WR 48a. These data are currently embargoed until roughly mid-2025, but geometric modelling of these systems will be possible with their public release. Modelling the JWST epoch of WR 48a, presumably with many more visible shells, will be essential in verifying our parameters and fit introduced in Chapter 4. Many of these systems, including Apep, may also be observed again in the coming years which will be another important verification of our models, and in particular the expansion properties of each nebula (see Appendix B). In parallel, continued photometric modelling of these systems in the mid-infrared will allow us to constrain these systems’ dust production properties through our light curve modelling. The light curve modelling is applicable not only to those systems imaged already, but also may be used for CWBs too far away to be directly imaged (for example in the SMC/LMC).

Finally, we advocate observations of Apep, and more broadly colliding wind binaries overall, with the Atacama Large Millimeter Array (ALMA; Brown et al., 2004). In Appendix B we describe how this observatory is capable of resolving the velocity profile of nebulous dust; we show predictions of what we may see in Apep with ALMA, and confirming this would be a vindication of our model parameters and provide a powerful probe of wind anisotropy in the nebula structure itself.



PRESIDENT MERKIN MUFFLEY

How is it possible for this thing to be triggered automatically and at the same time impossible to untrigger?

DR. STRANGELOVE

Mr. President, it is not only possible, it is essential. That is the whole idea of this machine, you know ... because of the automated and irrevocable decision-making process which rules out human meddling, the Doomsday machine is terrifying and simple to understand... and completely credible and convincing.

Dr. Strangelove or: How I Learned to Stop Worrying and Love the Bomb (1964)



Statistical Inference with the Geometric Model

In this Chapter we discuss our efforts to use our new geometric model together with modern statistical methods to perform the first numerical parameter inference of the Wolf-Rayet colliding wind nebulae. Previous analyses on the subject involved manually tuning model parameters to arrive at nebula geometry that visibly matches observed images¹, but this comes with ambiguous and large errorbars. In Chapter 3 we described our success in creating a fully differentiable geometric model, and so we naturally turn to gradient-based inference methods such as Hamiltonian Monte Carlo which scale efficiently to high dimensional problems such as ours.

A.1 Hamiltonian Monte Carlo

Parameter inference is the cornerstone on scientific analyses; we model some phenomenon and determine our model parameters that best reproduces a set of observations. Optimisation techniques, such as least-squares or gradient-descent, are able to efficiently arrive at best-fitting parameters but without any information on our uncertainty on those parameter estimates. To find both best-fitting parameters and their uncertainties, we can employ Bayesian inference methods such as Markov Chain Monte Carlo (Gelfand & Smith, 1990; Hogg et al., 2010). Bayesian methods seek to infer a probability distribution of *belief* over parameters to be inferred from data using Bayes' rule

$$p(\Theta, D) = p(\Theta) \frac{p(D|\Theta)}{p(D)} \quad (\text{A.1})$$

¹This is colloquially referred to as ‘chi by eye’, in reference to χ^2 minimisation performed purely by visual fit. This is usually a very good first pass at the problem, but the ‘fit’ parameters should be thought of with some degree of scepticism which is somewhat offset by large errorbars.

as a foundation. The objective of an MCMC sampler is to infer *integrals* of the posterior probability distribution, $p(\Theta, D)$, of our parameters Θ given our data D , such as moments (means, standard deviations), and to visualise these posteriors (e.g. with histograms or kernel density estimation). To do this, we need to supply our prior probability distribution of our parameters, $p(\Theta)$, and our probability of obtaining such data conditioned on our parameters (referred to as the likelihood), $p(D|\Theta)$, where the $p(D)$ term is treated as a normalisation constant.

The way that MCMC samplers work in practice is to initialise a population of ‘walkers’ which move around parameter space, sampling the likelihood at that location as they travel². Provided that we can assume that our data has Gaussian error, the likelihood is given as

$$\mathcal{L} \propto \exp(-\chi^2/2) \quad (\text{A.2})$$

where the exponential term is calculated with the χ^2 test statistic,

$$\chi^2 = \sum_i \left(\frac{D_i - M_i}{\sigma_i} \right)^2 \quad (\text{A.3})$$

which evaluates the ‘goodness of fit’ of our model evaluation, M_i using parameters Θ_i , against our data D_i with error σ_i . The goal of the walker is then to sample regions of high likelihood (and hence low χ^2), and this is commonly done with the Metropolis-Hastings algorithm (Metropolis et al., 1953; Hastings, 1970). In this algorithm, the next parameter position of each walker is decided by randomly choosing some location in a proposal distribution around the walker, where the walker then has a chance to randomly reject that movement if the likelihood at the new location is relatively lower than its current location. Because of this random and uninformed movement, walkers often require many steps during the ‘burn-in’ process of the MCMC run (where they travel from an initial position to the equilibrium posterior distribution). This issue is exacerbated when dealing with a higher dimensional problem ($N_{\text{dim}} \gtrsim 10$) where we would require prohibitively many samples for the walkers to converge to the ‘true’ posterior distribution.

More recently, gradient-based methods of moving walkers around the parameter space have been adopted in large part due to advances in computing. We consider the Hamiltonian Monte Carlo (HMC, first introduced in Duane et al., 1987) class of MCMC methods; with HMC we can think of a walker instead as a ball that bounces and rolls around the parameter space with some momentum, ρ . From Betancourt (2017), the Hamiltonian that describes the ball’s movement is

$$H(\rho, \Theta) \equiv -\log p(\rho, \Theta) = -\log(\rho|\Theta) - \log p(\Theta) \quad (\text{A.4})$$

$$= K(\rho, \Theta) + V(\Theta) \quad (\text{A.5})$$

We can think of the functions K and V as the kinetic and potential energy, respectively, relating to the motion of the ball. Using the gradient of our likelihood function, we can

²We have available an animation [online](#) that shows walkers travelling in parameter space, populating the associated posterior distribution for a simplified cosmological parameter study on simulated data. This animation was produced using the Python MCMC sampler `emcee` (Foreman-Mackey et al., 2013).

evolve the position of the ball with Hamilton's equations of motion

$$\frac{d\Theta}{dt} = \frac{\partial H}{\partial \rho} \quad (\text{A.6})$$

$$\frac{d\rho}{dt} = -\frac{\partial H}{\partial \Theta} \quad (\text{A.7})$$

that, numerically, is typically done with the Leapfrog symplectic (i.e. energy conserving) integrator. The conservation of energy ensures that the walker is able to efficiently explore the typical set of the distribution, which in high dimensions resembles a thin manifold arising from the balance of the volume element and the probability density.

Hamiltonian Monte Carlo methods typically outperform non-gradient-based methods in robustly sampling the target posterior distribution. Because the direction of walker movement is informed by the gradients of the likelihood, HMC methods converge to the equilibrium distribution in significantly (sometimes orders of magnitude) fewer steps and can do so no matter the dimensionality of the parameter space. Where HMC can fail, though, is for highly multimodal posteriors where the walker is not able to bridge the distance between likelihood maxima; in these cases, more general Bayesian methods such as Nested Sampling (Skilling, 2004) are needed.

With a gradient-friendly model developed, the consideration in using HMC then turns to the integration parameters for evolving the walkers' motion. The parameters that require user-tuning are the integration step-size and the number of steps to take, and the success of the HMC run is strongly dependent to the (often opaque) numerical choice of these parameters. Fortunately, Hoffman & Gelman (2014) introduce the 'No U-Turn Sampler' (NUTS) which automatically tunes these parameters to optimise sampling robustness and computational cost. The HMC-NUTS algorithm is implemented in the Python/JAX library NumPyro (Phan et al., 2019; Bingham et al., 2019; Neal, 2011; Hoffman & Gelman, 2014; Betancourt, 2017), which we have used for inference with our geometric model.

In fitting our models to the observed nebulae, we should only be concerned with those parameters that can be uniquely constrained by the geometry. This means that we do not fit for the distance to the system (which relies on information external to the plume geometry itself), or, in the case where only one dust shell is visible, the orbital period and nebula expansion speed. When multiple epochs of direct imaging are available, the angular expansion speed can be inferred, and when multiple shells are visible the orbital period can be inferred with the expansion speed.

A.2 Inference on Simulated Data

Before we can attempt to run Hamiltonian Monte Carlo for Apep's parameters with the actual data, we must first verify that we can recover the true parameters on simulated data. In doing so we may identify biases (if any) in the recovered parameters and potentially identify any multimodality in the posteriors that would hinder HMC on the real data.

We begin by rendering a single image of a nebula with parameters very similar to those in Tables 5.1 and 5.2, i.e. similar to our manual fit of Apep. The flux scale of the simulated image is in the range [0, 1], and we then inject Gaussian random noise (with $\mu = 0$, $\sigma = 0.05$)



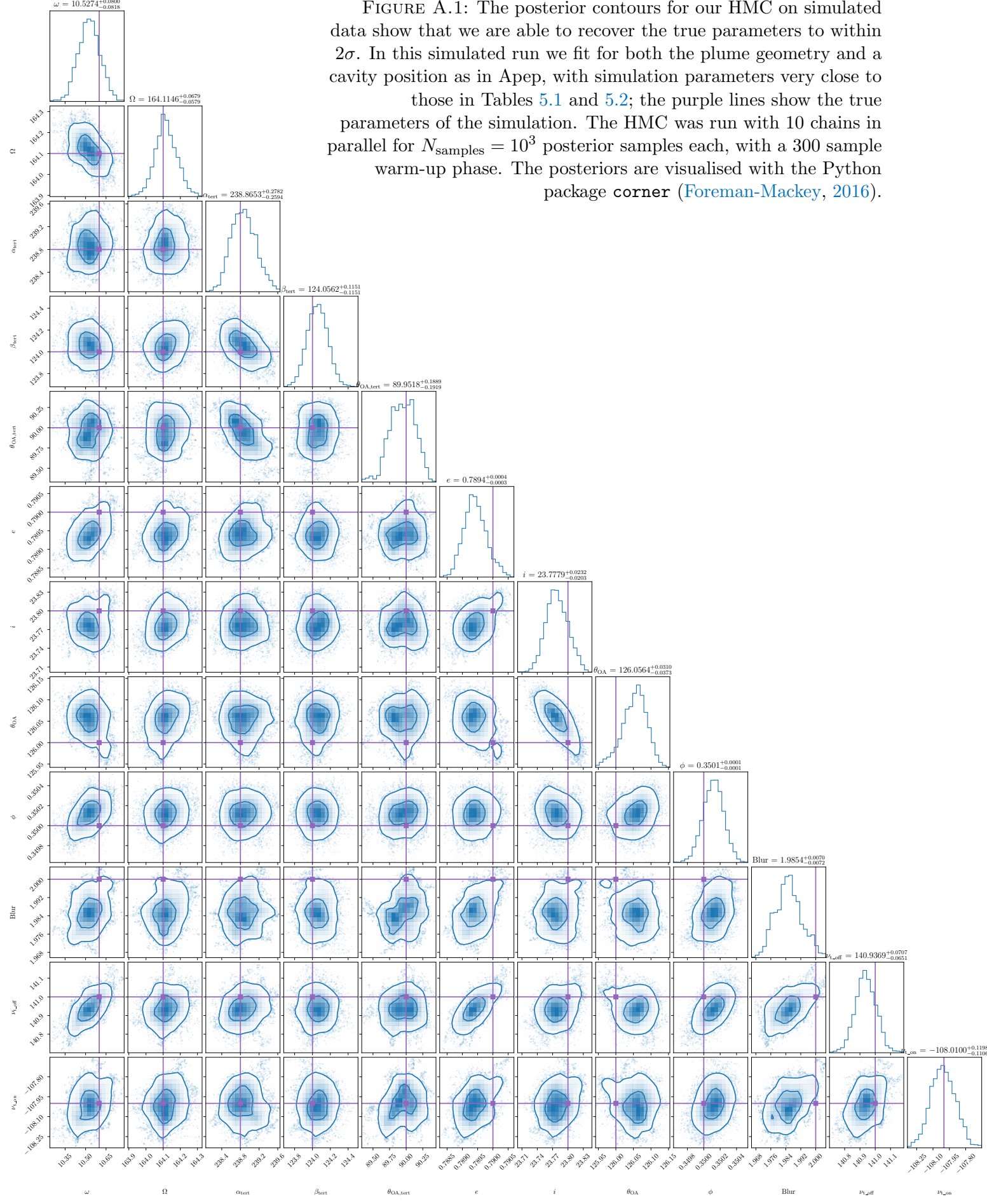


FIGURE A.1: The posterior contours for our HMC on simulated data show that we are able to recover the true parameters to within 2σ . In this simulated run we fit for both the plume geometry and a cavity position as in Apep, with simulation parameters very close to those in Tables 5.1 and 5.2; the purple lines show the true parameters of the simulation. The HMC was run with 10 chains in parallel for $N_{\text{samples}} = 10^3$ posterior samples each, with a 300 sample warm-up phase. The posteriors are visualised with the Python package `corner` (Foreman-Mackey, 2016).

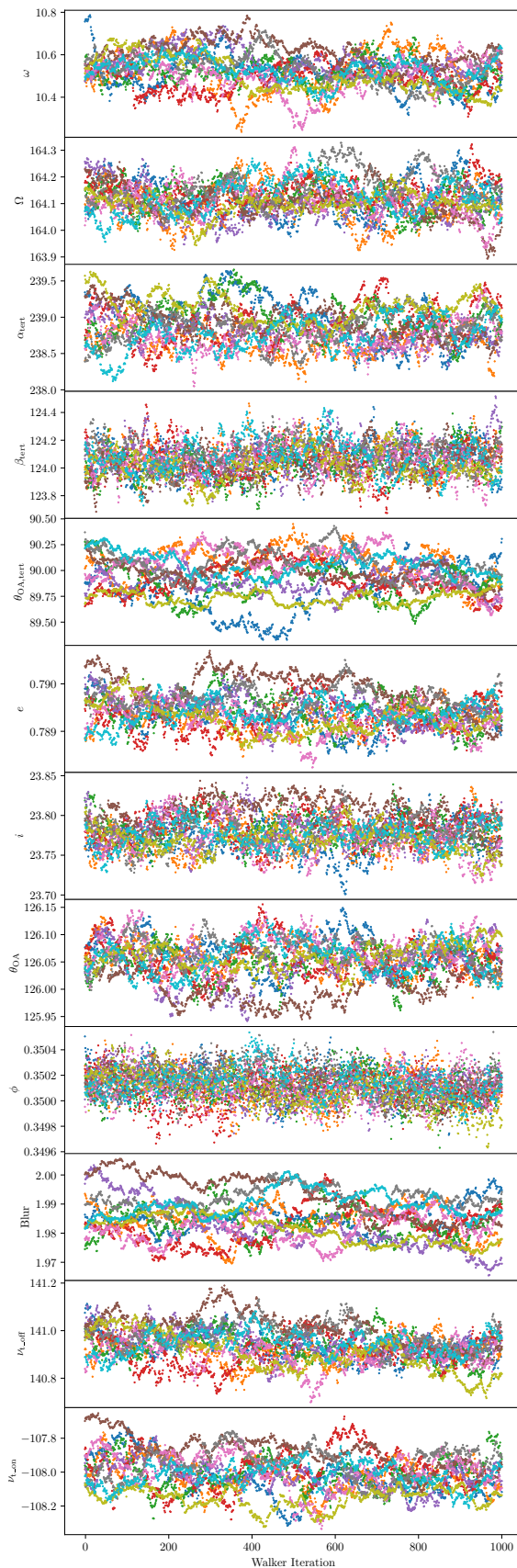


FIGURE A.2: The individual samples for the posterior contours in Figure A.1 show that each chain is burned in and has an autocorrelation time typically $\tau \ll N_{\text{samples}}$. Each marker colour corresponds to a different chain, and each chain had an independent warm-up phase initialised at the true parameters.



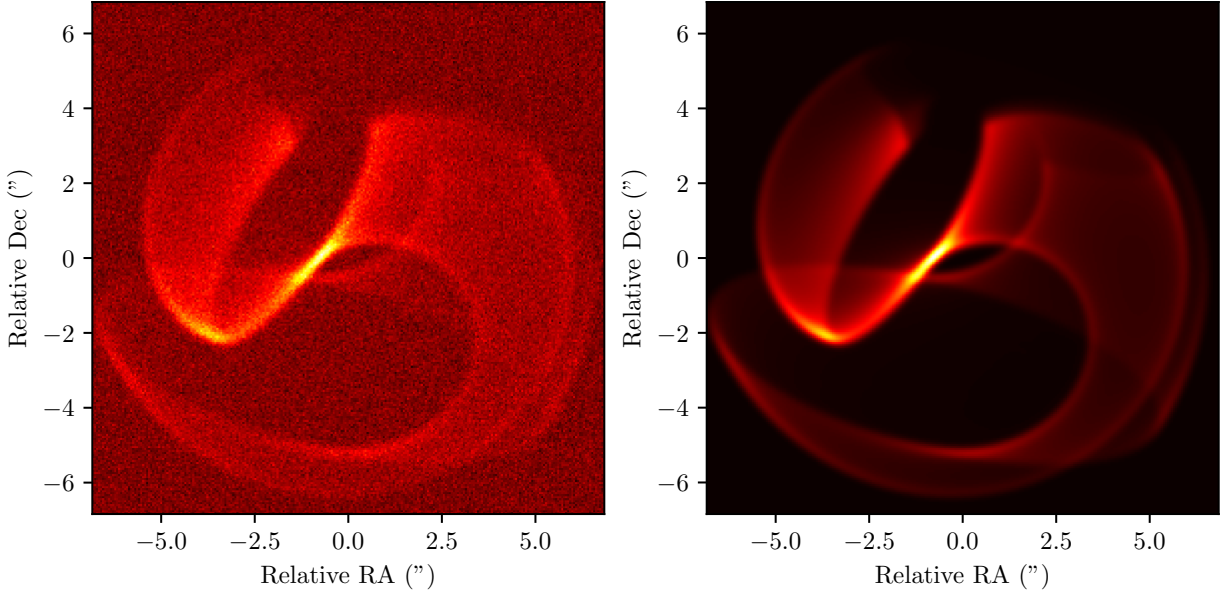


FIGURE A.3: We compare the simulated data with injected noise (left) to the model fit using the posterior means (right) from Figure A.1. The images are virtually indistinguishable by eye on account of the $\lesssim 2\sigma$ agreement in the fit parameters to their true values.

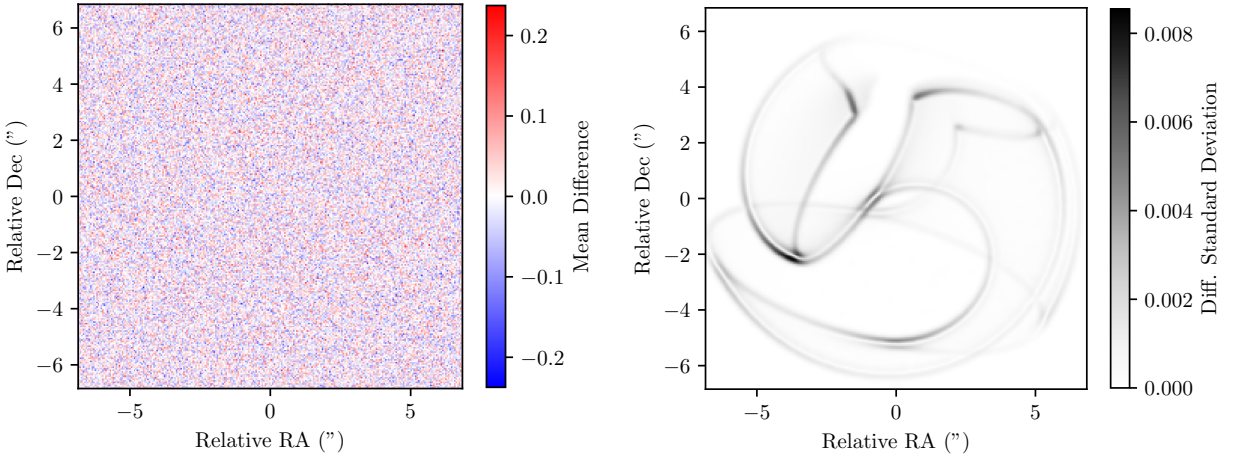


FIGURE A.4: We show here key per-pixel summary statistics of a subset of the posterior sample difference images, subtracting the model fit from the simulated image (right and left sides of Figure A.3 respectively). Each plot consists of a random sample of 500 of the total 10^4 samples. *Left:* The per-pixel mean across the posterior effectively reduces to random noise. *Right:* The per-pixel standard deviation (of the true image subtracted from the model image) across the posterior samples shows how the geometry is explored by the walkers across the HMC run; areas of higher variance represent pixels that have changed in flux across different posterior positions.

into the image to emulate the detector/photometric noise from a real telescope. The final simulated image is shown on the left side of Figure A.3.

Our fitting procedure begins with initialising a `NumPyro` model that randomly samples our parameters with uniform priors. Each sample of parameters is then used to generate a model image which is compared to the ‘true’ (noisy simulated) image with a χ^2 evaluation. Although the true image was injected with $\sigma_{\text{true}} = 0.05$, we set a flat $\sigma_{\text{model}} = 0.08$ across all of the pixels to encourage more parameter movement around the posterior modes. With this set up, `NumPyro`’s HMC-NUTS implementation then handles the parameter inference itself.

Without pre-existing knowledge of how HMC-NUTS behaves with our geometric model, we chose to run the algorithm with a warm-up phase of 300 iterations and a final sampling of 10^3 iterations. We ran this for 10 independent chains in parallel on the UQ School of Mathematics and Physics High-Performance Computing (HPC) cluster `Getafix`, initialising each chain at the true parameters. We show each parameter sampling of each chain in Figure A.2; each chain appears to have converged to the equilibrium distribution and has an autocorrelation time $\tau < N_{\text{samples}}$. The autocorrelation time is a measure of how many samples it takes a chain to ‘forget’ where it started, and so to be confident that we have robustly sampled the posteriors we should typically aim for $N_{\text{samples}} \sim 50\tau$ (Foreman-Mackey et al., 2013); this is not the case for some of the parameters we have fitted for (particularly evident for the Gaussian blur and $\theta_{\text{OA,tert}}$ in Figure A.2) although this is largely offset by sampling with multiple chains.

We show in Figure A.4 some per-pixel summary statistics of the model. In this figure we are comparing the pixel difference in the model and simulated image, $M_i - D_i$, over a subset of 5% of the total run samples across all chains. We see that the mean value of each pixel across the samples reduces to simply random noise, consistent with the injected noise on the simulated data. Plotting the standard deviation of the pixel values across the samples reveals that the ridge geometry is the key factor in the HMC fitting: we see a distinct border around each ridge showing how the walker trajectories impact the plume geometry.

With the sampling complete, we can easily see the posterior distributions and the parameter correlations in Figure A.1. Overall the posteriors are largely Gaussian and with surprisingly small spreads. We attribute the small errorbars here to two main factors. The first is that with a simulated image we are capable of reproducing the observed geometry *exactly* with our model. To minimise this effect we could try fitting to simulated data while fixing a subset of the parameters to deliberately, but not significantly, incorrect values to see how the walkers respond. The second factor could be due to a misspecification of the flux uncertainty (which feeds into the χ^2 value on each data-model comparison).

A.2.1 Towards Inference with Apep’s Four VLT Epochs

When handling data in the context of raw photon counts, the uncertainty is well described by Poisson statistics in the form of shot noise (Gehrels, 1986). In our case dealing with a transformed flux value, the uncertainty is not so fundamental. Our treatment of a constant flux uncertainty across all pixels no matter their value is oversimplified and we expect that the uncertainty should be proportional to the flux value itself. With this in mind we propose



a per-pixel uncertainty of

$$\sigma_{\text{pixel}} = \sqrt{aF_{\text{pixel}} + b^2} \quad (\text{A.8})$$

where F_{pixel} is the transformed flux of each pixel and a and b are free parameters that we can fit for during the HMC. For this we must impose log-uniform priors on a and b so that they prefer smaller values. Large values of these would mean that σ_{pixel} blows up and therefore the χ^2 would cease to be effective as a measure of the goodness of fit. Ideally these parameters should be tuned such that the reduced χ^2 ,

$$\chi^2_{\text{dof}} = \frac{\chi^2}{\text{degrees of freedom} - 1} \quad (\text{A.9})$$

equals 1, $\chi^2_{\text{dof}} = 1$, which indicates that the model represents the data well within the prescribed error. Initial tests show that this error prescription does not have much effect on the χ^2_{dof} of simulated data but is essential in tuning it towards 1 for the 4 VISIR epochs. For the VLT data we find that $a \sim 1$ and $10^{-4} \lesssim b \lesssim 10^{-2}$ gives the best results although this will need to be individually tuned for each image.

In the context of simulated data, we can be certain that the plume origin (that is, the centre point of the image) is consistent between the model and the true image since both were created in the same model pipeline. In the case of comparing our model to the real data, we cannot be so sure. With this in mind we also propose including two more parameters: a right ascension and declination offset, x and y respectively. Again, these parameters will need to be individually tuned for each VISIR image during the HMC run, and we expect their values to be close to 0 (having a modest uniform prior).

B

Velocity Maps with the Geometric Model

Since our geometric model creates an expanding point cloud of particles in 3D space (which we flatten to 2D to visualise in images), we are able to create tangential and radial velocity maps of these particles. In doing so, we can predict the expansion properties of each nebula (from the tangential velocity map) and the spectral properties of molecules within the nebula (from the radial velocity map which gives the doppler shift). The expansion properties of the nebula can be compared with multiple epochs of imaging, showing how the ridge geometry evolves in shape as it expands and by its proper motion in the plane of the sky (POS). We show in the bottom plot of Figure B.1 the integrated POS velocity of the Apep nebula using our geometric model and parameters in Tables 5.1 and 5.2.

Obtaining a line of sight velocity map of a colliding wind nebula will allow for an unambiguous calculation of its expansion speed. With multiple epochs of imaging and an idea of the expansion through the geometric model, this can then be used to infer the distance to CWBs. The Atacama Large Millimeter Array (ALMA; [Brown et al., 2004](#)) stands out as the foremost observatory to observe such a map. ALMA is capable of resolving the radial velocity distribution of spectral lines in each pixel of an image; this functionality was used to create a radial velocity map of the protoplanetary disc around AB Aurigae ([Speedie et al., 2024](#)). We show in the top plot of Figure B.1 our prediction for what a radial velocity map of Apep would look like, using our geometric model.



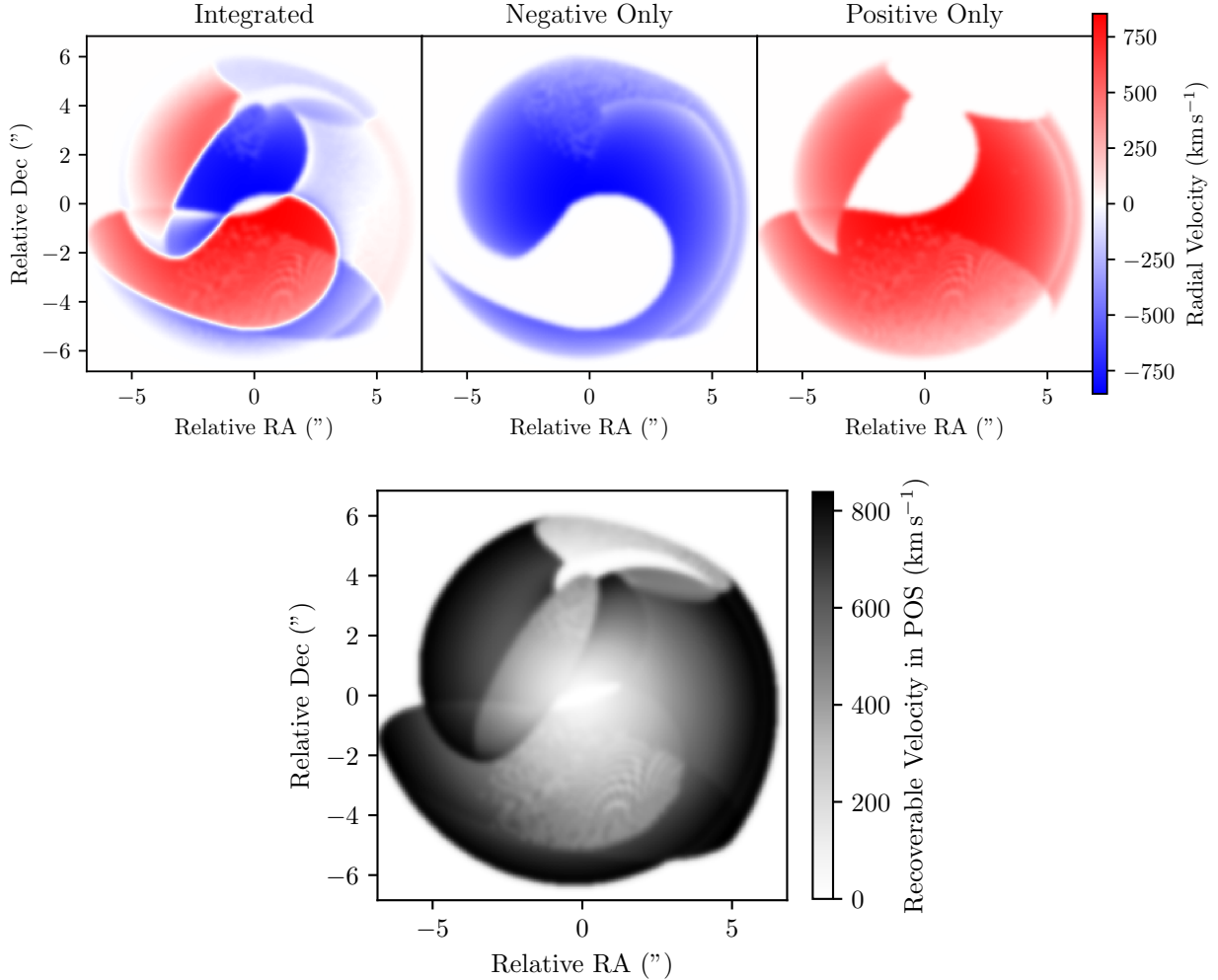


FIGURE B.1: The radial (top) and tangential (bottom) velocity maps of our modelled Apép nebula show what we might observe with ALMA imaging, and what drives the nebula expansion in our multi-epoch Apép imaging, respectively. These maps are created by integrating the particle velocities (radial or tangential) along the line of sight through the image pixels, assuming that the nebula is entirely optically thin. The radial velocity signal is largest towards the centre of the plume, while the tangential velocity signal is largest towards the far edges of the plume. Each image is convolved with a $\sigma = 1.5 \text{ px}$ Gaussian blur (Virtanen et al., 2020) to reduce the quantisation effect of us modelling the (actually smooth) nebula with discrete particles.

References

- Abbott D. C., Conti P. S., 1987, [ARA&A](#), **25**, 113
- Aguilera-Dena D. R., Langer N., Moriya T. J., Schootemeijer A., 2018, [ApJ](#), **858**, 115
- Allen D. A., Swings J. P., Harvey P. M., 1972, [A&A](#), **20**, 333
- Antognini J. M. O., 2015, [MNRAS](#), **452**, 3610
- Antognini J. M. O., Thompson T. A., 2016, [MNRAS](#), **456**, 4219
- Archimedes 2017, in Netz R., ed., , The Works of Archimedes: Translation and Commentary.
Cambridge University Press
- Ashall C., et al., 2019, [MNRAS](#), **487**, 5824
- Barlow M. J., Smith L. J., Willis A. J., 1981, [MNRAS](#), **196**, 101
- Baug T., de Grijs R., Dewangan L. K., Herczeg G. J., Ojha D. K., Wang K., Deng L., Bhatt B. C., 2019, [ApJ](#), **885**, 68
- Bavera S. S., et al., 2022, [A&A](#), **657**, L8
- Berger E., 2014, [ARA&A](#), **52**, 43
- Betancourt M., 2017, [arXiv e-prints](#), p. arXiv:1701.02434
- Bingham E., et al., 2019, [J. Mach. Learn. Res.](#), **20**, 28:1
- Bloot S., Callingham J. R., Marcote B., 2022, [MNRAS](#), **509**, 475
- Bonanos A. Z., et al., 2004, [ApJ](#), **611**, L33
- Bradbury J., et al., 2018, JAX: composable transformations of Python+NumPy programs,
<http://github.com/google/jax>
- Brown R. L., Wild W., Cunningham C., 2004, [Advances in Space Research](#), **34**, 555
- Callingham J. R., Tuthill P. G., Pope B. J. S., Williams P. M., Crowther P. A., Edwards M., Norris B., Kedziora-Chudczer L., 2019, [Nature Astronomy](#), **3**, 82
- Callingham J. R., Crowther P. A., Williams P. M., Tuthill P. G., Han Y., Pope B. J. S., Marcote B., 2020, [MNRAS](#), **495**, 3323



- Cameron A. J., Katz H., Witten C., Saxena A., Laporte N., Bunker A. J., 2024, *MNRAS*, **534**, 523
- Carroll B. W., Ostlie D. A., 2017, An Introduction to Modern Astrophysics, Second Edition. Cambridge University Press
- Castor J. I., Abbott D. C., Klein R. I., 1975, *ApJ*, **195**, 157
- Chené A.-N., St-Louis N., Moffat A. F. J., Gayley K. G., 2020, *ApJ*, **903**, 113
- Cherchneff I., Le Teuff Y. H., Williams P. M., Tielens A. G. G. M., 2000, *A&A*, **357**, 572
- Cherepashchuk A. M., 1976, Soviet Astronomy Letters, **2**, 138
- Chiappini C., Hirschi R., Meynet G., Ekström S., Maeder A., Matteucci F., 2006, *A&A*, **449**, L27
- Chira R. A., Kainulainen J., Ibáñez-Mejía J. C., Henning T., Mac Low M. M., 2018, *A&A*, **610**, A62
- Chrimes A. A., Stanway E. R., Eldridge J. J., 2020, *MNRAS*, **491**, 3479
- Cichowski S., Suad L. A., Pineault S., Noriega-Crespo A., Arnal E. M., Flagey N., 2015, *MNRAS*, **450**, 3458
- Conti P. S., 1975, Memoires of the Societe Royale des Sciences de Liege, **9**, 193
- Crowther P. A., 2007, *ARA&A*, **45**, 177
- Crowther P. A., Smith L. J., 1997, *A&A*, **320**, 500
- Dale J. E., Ngoumou J., Ercolano B., Bonnell I. A., 2013, *MNRAS*, **436**, 3430
- Danks A. C., Dennefeld M., Wamsteker W., Shaver P. A., 1983, *A&A*, **118**, 301
- De Becker M., Raucq F., 2013, *A&A*, **558**, A28
- De Buizer J., Fisher R., 2005, in Käufl H. U., Siebenmorgen R., Moorwood A., eds, High Resolution Infrared Spectroscopy in Astronomy. pp 84–87 ([arXiv:astro-ph/0402572](https://arxiv.org/abs/astro-ph/0402572)), doi:10.1007/10995082_12
- De Marco O., Izzard R. G., 2017, *PASA*, **34**, e001
- de Koter A., Heap S. R., Hubeny I., 1997, *ApJ*, **477**, 792
- de Wit W. J., Testi L., Palla F., Zinnecker H., 2005, *A&A*, **437**, 247
- Dean C., Fernández R., 2024, *Phys. Rev. D*, **109**, 083010
- Deshmukh K., et al., 2024, Investigating 39 Galactic Wolf-Rayet stars with VLTI/GRAVITY: Uncovering A Long Period Binary Desert ([arXiv:2409.15212](https://arxiv.org/abs/2409.15212)), <https://arxiv.org/abs/2409.15212>

- Detmers R. G., Langer N., Podsiadlowski P., Izzard R. G., 2008, [A&A](#), **484**, 831
- Dougherty S. M., Beasley A. J., Claussen M. J., Zauderer B. A., Bolingbroke N. J., 2005, [ApJ](#), **623**, 447
- Dsilva K., Shenar T., Sana H., Marchant P., 2020, [A&A](#), **641**, A26
- Dsilva K., Shenar T., Sana H., Marchant P., 2022, [A&A](#), **664**, A93
- Dsilva K., Shenar T., Sana H., Marchant P., 2023, [A&A](#), **674**, A88
- Duane S., Kennedy A. D., Pendleton B. J., Roweth D., 1987, [Physics Letters B](#), **195**, 216
- Eatson J. W., Pittard J. M., Van Loo S., 2022a, [MNRAS](#), **516**, 6132
- Eatson J. W., Pittard J. M., Van Loo S., 2022b, [MNRAS](#), **517**, 4705
- Eichler D., Usov V., 1993, [ApJ](#), **402**, 271
- Eldridge J. J., Langer N., Tout C. A., 2011, [MNRAS](#), **414**, 3501
- Eldridge J. J., Fraser M., Smartt S. J., Maund J. R., Crockett R. M., 2013, [MNRAS](#), **436**, 774
- Endo I., Lau R. M., Sakon I., Onaka T., Williams P. M., Shenavrin V. I., 2022, [ApJ](#), **930**, 116
- Filippenko A. V., 1997, [ARA&A](#), **35**, 309
- Foellmi C., Moffat A. F. J., Guerrero M. A., 2003, [MNRAS](#), **338**, 1025
- Foreman-Mackey D., 2016, [The Journal of Open Source Software](#), **1**, 24
- Foreman-Mackey D., Hogg D. W., Lang D., Goodman J., 2013, [PASP](#), **125**, 306
- Galama T. J., et al., 1998, [Nature](#), **395**, 670
- Gamow G., 1943, [ApJ](#), **98**, 500
- Gayley K. G., 2009, [ApJ](#), **703**, 89
- Gehrels N., 1986, [ApJ](#), **303**, 336
- Gehrzi R. D., Hackwell J. A., 1974, [ApJ](#), **194**, 619
- Gelfand A. E., Smith A. F., 1990, [Journal of the American Statistical Association](#), **85**, 398
- Gorny S. K., Stasińska G., 1995, [A&A](#), **303**, 893
- Gosset E., Nazé Y., 2016, [A&A](#), **590**, A113
- Gräfener G., Hamann W. R., 2008, [A&A](#), **482**, 945



- Gräfener G., Vink J. S., de Koter A., Langer N., 2011, *A&A*, **535**, A56
- Groh J. H., Meynet G., Georgy C., Ekström S., 2013, *A&A*, **558**, A131
- Hacar A., Clark S. E., Heitsch F., Kainulainen J., Panopoulou G. V., Seifried D., Smith R., 2023, in Inutsuka S., Aikawa Y., Muto T., Tomida K., Tamura M., eds, Astronomical Society of the Pacific Conference Series Vol. 534, Protostars and Planets VII. p. 153 ([arXiv:2203.09562](https://arxiv.org/abs/2203.09562)), doi:10.48550/arXiv.2203.09562
- Hamann W. R., Gräfener G., Liermann A., 2006, *A&A*, **457**, 1015
- Han Y., et al., 2020, *MNRAS*, **498**, 5604
- Han Y., Tuthill P. G., Lau R. M., Soulain A., 2022, *Nature*, **610**, 269
- Harries T. J., Babler B. L., Fox G. K., 2000, *A&A*, **361**, 273
- Harries T. J., Monnier J. D., Symington N. H., Kurosawa R., 2004, *MNRAS*, **350**, 565
- Harris C. R., et al., 2020, *Nature*, **585**, 357
- Hastings W. K., 1970, *Biometrika*, **57**, 97
- Hastings B., Langer N., Puls J., 2023, *A&A*, **672**, A60
- Hattori S., Garcia L., Murray C., Dong J., Dholakia S., Degen D., Foreman-Mackey D., 2024, exoplanet-dev/jaxplanet: Astronomical time series analysis with JAX, doi:10.5281/zenodo.10736936, <https://doi.org/10.5281/zenodo.10736936>
- Hendrix T., Keppens R., van Marle A. J., Camps P., Baes M., Meliani Z., 2016, *MNRAS*, **460**, 3975
- Hoffman M. D., Gelman A., 2014, *Journal of Machine Learning Research*, **15**, 1593
- Hogg D. W., Bovy J., Lang D., 2010, *arXiv e-prints*, p. arXiv:1008.4686
- Hoyle F., 1953, *ApJ*, **118**, 513
- Hunter J. D., 2007, *Computing in Science & Engineering*, **9**, 90
- Hurtado V. U., Lloyd-Ronning N. M., Miller J. M., 2024, *ApJ*, **967**, L4
- Josiek J., Ekström S., Sander A. A. C., 2024, *arXiv e-prints*, p. arXiv:2404.14488
- Karamehmetoglu E., et al., 2023, *A&A*, **678**, A87
- Kells L. M., Kern W. F., 1940, *Plane and Spherical Trigonometry*, 2nd ed. edn. McGraw Hill Book Company, New York
- Kilpatrick C. D., et al., 2021, *MNRAS*, **504**, 2073
- Kroupa P., 2001, *MNRAS*, **322**, 231

- Lagage P. O., et al., 2004, *The Messenger*, **117**, 12
- Lamberts A., Dubus G., Lesur G., Fromang S., 2012, *A&A*, **546**, A60
- Lau R. M., Hankins M. J., Schödel R., Sanchez-Bermudez J., Moffat A. F. J., Ressler M. E., 2017, *ApJ*, **835**, L31
- Lau R. M., Eldridge J. J., Hankins M. J., Lamberts A., Sakon I., Williams P. M., 2020a, *ApJ*, **898**, 74
- Lau R. M., et al., 2020b, *ApJ*, **900**, 190
- Lau R. M., et al., 2021, *ApJ*, **909**, 113
- Lau R. M., et al., 2022, *Nature Astronomy*, **6**, 1308
- Lau R. M., et al., 2023, *ApJ*, **951**, 89
- Lau R. M., et al., 2024, *ApJ*, **963**, 127
- Lefevre L., et al., 2005, *MNRAS*, **360**, 141
- Mackey J., Jones T. A. K., Brose R., Grassitelli L., Reville B., Mathew A., 2023, *MNRAS*, **526**, 3099
- Maeder A., 1983, *A&A*, **120**, 113
- Maeder A., Georgy C., Meynet G., Ekström S., 2012, *A&A*, **539**, A110
- Marchenko S. V., Moffat A. F. J., 2007, in St. -Louis N., Moffat A. F. J., eds, Astronomical Society of the Pacific Conference Series Vol. 367, Massive Stars in Interactive Binaries. p. 213 ([arXiv:astro-ph/0610531](https://arxiv.org/abs/astro-ph/0610531)), doi:10.48550/arXiv.astro-ph/0610531
- Marchenko S. V., Moffat A. F. J., Vacca W. D., Côté S., Doyon R., 2002, *ApJ*, **565**, L59
- Marchenko S. V., Moffat A. F. J., Crowther P. A., 2010, *ApJ*, **724**, L90
- Marcote B., Callingham J. R., De Becker M., Edwards P. G., Han Y., Schulz R., Stevens J., Tuthill P. G., 2021, *MNRAS*, **501**, 2478
- Markley F. L., 1995, *Celestial Mechanics and Dynamical Astronomy*, **63**, 101
- McClelland L. A. S., Eldridge J. J., 2016, *MNRAS*, **459**, 1505
- Metropolis N., Rosenbluth A. W., Rosenbluth M. N., Teller A. H., Teller E., 1953, *J. Chem. Phys.*, **21**, 1087
- Meynet G., Georgy C., Hirschi R., Maeder A., Massey P., Przybilla N., Nieva M. F., 2011, *Bulletin de la Societe Royale des Sciences de Liege*, **80**, 266
- Michaux Y. J. L., Moffat A. F. J., Chené A.-N., St-Louis N., 2014, *MNRAS*, **440**, 2



- Miller G. E., Scalo J. M., 1979, [ApJS](#), **41**, 513
- Moens N., Poniatowski L. G., Hennicker L., Sundqvist J. O., El Mellah I., Kee N. D., 2022, [A&A](#), **665**, A42
- Monnier J. D., Tuthill P. G., Danchi W. C., 1999, [ApJ](#), **525**, L97
- Monnier J. D., Tuthill P. G., Danchi W. C., 2002, [ApJ](#), **567**, L137
- Monnier J. D., et al., 2011, [ApJ](#), **742**, L1
- Motte F., Bontemps S., Louvet F., 2018, [ARA&A](#), **56**, 41
- Murray C. D., Dermott S. F., 1999, Solar System Dynamics. Cambridge University Press, [doi:10.1017/CBO9781139174817](#)
- Murray N., Ménard B., Thompson T. A., 2011, [ApJ](#), **735**, 66
- Naoz S., 2016, [ARA&A](#), **54**, 441
- Neal R., 2011, in , Handbook of Markov Chain Monte Carlo. Chapman & Hall/CRC, pp 113–162, [doi:10.1201/b10905](#)
- Nishimaki Y., Yamamuro T., Motohara K., Miyata T., Tanaka M., 2008, [PASJ](#), **60**, 191
- Offner S. S. R., Moe M., Kratter K. M., Sadavoy S. I., Jensen E. L. N., Tobin J. J., 2023, in Inutsuka S., Aikawa Y., Muto T., Tomida K., Tamura M., eds, Astronomical Society of the Pacific Conference Series Vol. 534, Protostars and Planets VII. p. 275 ([arXiv:2203.10066](#)), [doi:10.48550/arXiv.2203.10066](#)
- Olivier G. M., et al., 2022, arXiv e-prints, p. arXiv:2212.02514
- Paczyński B., 1967, [Acta Astron.](#), **17**, 355
- Parkin E. R., Pittard J. M., 2008, [MNRAS](#), **388**, 1047
- Peatt M. J., Richardson N. D., Williams P. M., Karnath N., Shenavrin V. I., Lau R. M., Moffat A. F. J., Weigelt G., 2023, [ApJ](#), **956**, 109
- Pellegrino C., et al., 2022, [ApJ](#), **938**, 73
- Phan D., Pradhan N., Jankowiak M., 2019, arXiv preprint arXiv:1912.11554
- Pinte C., Ménard F., Duchêne G., Bastien P., 2006, [A&A](#), **459**, 797
- Pittard J. M., 2010, [MNRAS](#), **403**, 1633
- Pittard J. M., Dawson B., 2018, [MNRAS](#), **477**, 5640
- Pittard J. M., Dougherty S. M., 2006, [MNRAS](#), **372**, 801
- Pledger J. L., Sharp A. J., Sansom A. E., 2021, [MNRAS](#), **503**, 2168

- Prilutskii O. F., Usov V. V., 1976, Soviet Ast., **20**, 2
- Rauw G., Nazé Y., 2016, *Advances in Space Research*, **58**, 761
- Rauw G., et al., 2005, *A&A*, **432**, 985
- Richardson N. D., et al., 2016, *MNRAS*, **461**, 4115
- Richardson N. D., et al., 2024, *arXiv e-prints*, p. arXiv:2405.10454
- Riley J., et al., 2022, *ApJS*, **258**, 34
- Rodríguez L. F., Arthur J., Montes G., Carrasco-González C., Toalá J. A., 2020, *ApJ*, **900**, L3
- Salpeter E. E., 1952, *ApJ*, **115**, 326
- Sana H., 2017, in Eldridge J. J., Bray J. C., McClelland L. A. S., Xiao L., eds, Vol. 329, The Lives and Death-Throes of Massive Stars. pp 110–117 ([arXiv:1703.01608](https://arxiv.org/abs/1703.01608)), doi:10.1017/S1743921317003209
- Sana H., Evans C. J., 2011, in Neiner C., Wade G., Meynet G., Peters G., eds, Vol. 272, Active OB Stars: Structure, Evolution, Mass Loss, and Critical Limits. pp 474–485 ([arXiv:1009.4197](https://arxiv.org/abs/1009.4197)), doi:10.1017/S1743921311011124
- Sander A. A. C., Vink J. S., 2020, *MNRAS*, **499**, 873
- Schönberner D., Balick B., Jacob R., 2018, *A&A*, **609**, A126
- Schootemeijer A., Shenar T., Langer N., Grin N., Sana H., Schürmann G. G. C., Wang C., Xu X. T., 2024, *arXiv e-prints*, p. arXiv:2406.01420
- Seaquist E. R., 1976, *ApJ*, **203**, L35
- Shara M. M., Howell S. B., Furlan E., Gnilka C. L., Moffat A. F. J., Scott N. J., Zurek D., 2022, *MNRAS*, **509**, 2897
- Shenar T., 2024, *arXiv e-prints*, p. arXiv:2410.04436
- Shenar T., Hamann W. R., Todt H., 2014, *A&A*, **562**, A118
- Shenar T., et al., 2017, *A&A*, **598**, A85
- Shenar T., Gilkis A., Vink J. S., Sana H., Sander A. A. C., 2020, *A&A*, **634**, A79
- Siebert M. R., et al., 2024, *arXiv e-prints*, p. arXiv:2406.05076
- Skilling J., 2004, in Fischer R., Preuss R., Toussaint U. V., eds, American Institute of Physics Conference Series Vol. 735, Bayesian Inference and Maximum Entropy Methods in Science and Engineering: 24th International Workshop on Bayesian Inference and Maximum Entropy Methods in Science and Engineering. AIP, pp 395–405, doi:10.1063/1.1835238



- Smartt S. J., 2009, *ARA&A*, **47**, 63
- Smith N., Conti P. S., 2008, *ApJ*, **679**, 1467
- Soulain A., et al., 2018, *A&A*, **618**, A108
- Soulain A., Lamberts A., Millour F., Tuthill P., Lau R. M., 2023, *MNRAS*, **518**, 3211
- Speedie J., et al., 2024, *Nature*, **633**, 58
- Stevens I. R., Blondin J. M., Pollock A. M. T., 1992, *ApJ*, **386**, 265
- Tan J. C., Beltrán M. T., Caselli P., Fontani F., Fuente A., Krumholz M. R., McKee C. F., Stolte A., 2014, in Beuther H., Klessen R. S., Dullemond C. P., Henning T., eds, Protostars and Planets VI. pp 149–172 ([arXiv:1402.0919](https://arxiv.org/abs/1402.0919)), doi:10.2458/azu-uapress-9780816531240-ch007
- Tolstoy E., Hill V., Tosi M., 2009, *ARA&A*, **47**, 371
- Tuthill P. G., Monnier J. D., Danchi W. C., 1999, *Nature*, **398**, 487
- Tuthill P. G., Monnier J. D., Danchi W. C., Wishnow E. H., Haniff C. A., 2000, *PASP*, **112**, 555
- Tuthill P., Monnier J., Tanner A., Figer D., Ghez A., Danchi W., 2006, *Science*, **313**, 935
- Tuthill P. G., Monnier J. D., Lawrence N., Danchi W. C., Owocki S. P., Gayley K. G., 2008, *ApJ*, **675**, 698
- Ud-Doula A., Owocki S. P., Townsend R. H. D., 2009, *MNRAS*, **392**, 1022
- Usov V. V., 1991, *MNRAS*, **252**, 49
- van Dalen J. N. D., et al., 2024, arXiv e-prints, p. arXiv:2409.19056
- van Marle A. J., Langer N., Yoon S. C., García-Segura G., 2008, *A&A*, **478**, 769
- van der Hucht K. A., 2001, *New A Rev.*, **45**, 135
- van der Hucht K. A., et al., 1996, *A&A*, **315**, L193
- Vink J. S., Harries T. J., 2017, *A&A*, **603**, A120
- Vink J. S., de Koter A., 2005, *A&A*, **442**, 587
- Vink J. S., Gräfener G., Harries T. J., 2011, *A&A*, **536**, L10
- Virtanen P., et al., 2020, *Nature Methods*, **17**, 261
- Vrancken M., De Greve J. P., Yungelson L., Tutukov A., 1991, *A&A*, **249**, 411

- Walder R., Folini D., Motamen S. M., 1999, in van der Hucht K. A., Koenigsberger G., Eenens P. R. J., eds, IAU Symposium Vol. 193, Wolf-Rayet Phenomena in Massive Stars and Starburst Galaxies. p. 298
- Wallace D. J., Moffat A. F. J., Shara M. M., 2002, in Moffat A. F. J., St-Louis N., eds, Astronomical Society of the Pacific Conference Series Vol. 260, Interacting Winds from Massive Stars. p. 407
- Williams P. M., 2019, [MNRAS](#), **488**, 1282
- Williams P. M., Beattie D. H., Lee T. J., Stewart J. M., Antonopoulou E., 1978, [MNRAS](#), **185**, 467
- Williams P. M., van der Hucht K. A., The P. S., 1987, [QJRAS](#), **28**, 248
- Williams P. M., van der Hucht K. A., Pollock A. M. T., Florkowski D. R., van der Woerd H., Wamsteker W. M., 1990, [MNRAS](#), **243**, 662
- Williams P. M., et al., 2009, [MNRAS](#), **395**, 1749
- Williams P. M., van der Hucht K. A., van Wyk F., Marang F., Whitelock P. A., Bouchet P., Setia Gunawan D. Y. A., 2012, [MNRAS](#), **420**, 2526
- Williams P. M., et al., 2021, [MNRAS](#), **503**, 643
- Willis A. J., 1982, [MNRAS](#), **198**, 897
- Wolf C. J. E., Rayet G., 1867, Academie des Sciences Paris Comptes Rendus, **65**, 292
- Woosley S. E., 1993, [ApJ](#), **405**, 273
- Woosley S. E., Bloom J. S., 2006, [ARA&A](#), **44**, 507
- Woosley S. E., Heger A., 2006, [ApJ](#), **637**, 914
- Woosley S. E., Heger A., Weaver T. A., 2002, [Reviews of Modern Physics](#), **74**, 1015
- Wright W. H., 1918, in Publications of the American Astronomical Society. p. 104
- Zavala S., Toalá J. A., Santamaría E., Ramos-Larios G., Sabin L., Quino-Mendoza J. A., Rubio G., Guerrero M. A., 2022, [MNRAS](#), **513**, 3317
- Zhekov S. A., 2021, [MNRAS](#), **500**, 4837
- Zhekov S. A., Park S., 2010a, [ApJ](#), **709**, L119
- Zhekov S. A., Park S., 2010b, [ApJ](#), **721**, 518
- Zhekov S. A., Tomov T., Gawronski M. P., Georgiev L. N., Borissova J., Kurtev R., Gagné M., Hajduk M., 2014, [MNRAS](#), **445**, 1663
- Zhekov S. A., Gagné M., Skinner S. L., 2022, [MNRAS](#), **510**, 1278

List of External Links

Histogram comparison https://github.com/ryanwhite1/ryanwhite1.github.io/blob/50b1641077793aeeddc225498e7c073b20468d2d/permanent_storage/apep_photos/thesis_specific/Hist_Co mparison_Gif.gif	33
GUI demonstration https://github.com/ryanwhite1/ryanwhite1.github.io/blob/50b1641077793aeeddc225498e7c073b20468d2d/permanent_storage/apep_photos/thesis_specific/GUI_gif. gif	34
WR 48a evolution over orbital period https://github.com/ryanwhite1/ryanwhite1.github.io/blob/831298ae03b8dd1f2d546040878edf54ee563a84/permanent_storage/apep_photos/thesis_specific/WR48a_e volution.gif	40
Apep VISIR epochs https://github.com/ryanwhite1/ryanwhite1.github.io/blob/50b1641077793aeeddc225498e7c073b20468d2d/permanent_storage/apep_photos/Apep_VISIR_gif.gif	46
Apep evolution over orbital period https://github.com/ryanwhite1/ryanwhite1.github.io/blob/5d6c4c84b9a65402912bed784c18a0c8b09488b6/permanent_storage/apep_photos/Apep_evolution.gif	49
MCMC walkers animation https://github.com/ryanwhite1/ryanwhite1.github.io/blob/50b1641077793aeeddc225498e7c073b20468d2d/permanent_storage/apep_photos/thesis_specific/MCMC_ walkers.gif	62

